Modeling and Analysis of Human Airway Dynamics Utilizing Data Obtained from a Cine MRI

by

Wesley A. Zloza

A Report Submitted to the Faculty of the

Milwaukee School of Engineering

in Partial Fulfillment of the

Requirements for the Degree of

Master of Science in Engineering

Milwaukee, WI

May 2017

ABSTRACT

The objective of this project was to determine the validity of using MRI (magnetic resonance imaging) data to identify abnormalities in human airways and to analyze the internal flow behavior, which is conducted by means of fluid flow analysis. CT (computed tomography) scans have long been used to develop three-dimensional (3D) models of internal anatomy because of their fine resolution and contrast between tissue densities. The negative aspect of these scans is that they expose patients to medical risks because of the radiation that is emitted when capturing the images. Because of these risks, MRIs are considered to be a safer imaging option; however, their image quality isn't as fine. The original goals of this project were to employ static (standard) and dynamic (cine) MRI images from pediatric patients to develop accurate models of their airways, and to use the models to perform computational fluid dynamics (CFD) simulations. CFD simulations results would then to be used to identify areas of large pressure differentials and air recirculation, which could indicate areas of concern. These results would then aid medical personnel in determining which medical procedures could be performed to minimize irregular or problematic air flow. Because of time constraints and challenges associated with the MRI images, the project goals were refined. Standard and cine MRI data from a single patient, and CT data from an additional patient, were employed in an attempt to establish a technique for developing accurate 3D fluid domain models from MRI data. This report explains the work performed during the two-phase project. The first phase of the project focused on the generation of 3D models from cine MRI data, and the second phase focused on use of the models in CFD simulation. To generate models from standard MRI data in their original DICOM format, a complicated series of data manipulation techniques was necessary. Using 3D Slicer, along with thresholding and image segmentation, a 3D mesh model was extracted and created. The mesh model was refined and converted to a STL format with a number of tools, including Blender, Meshmixer, and Remake. Fusion 360 was employed to convert this model into a solid model needed for simulation. The solid model was imported into ANSYS Fluent, where the mesh was optimized for simulation, and laminar and turbulent flow simulations were successfully conducted. An attempt was made to employ cine MRI data to analyze the changing geometry of the airway. Difficulties were encountered in working with the cine MRI data, because they had to be analyzed manually. A recommendation for future research is the development of a software program that can automate the analysis of cine MRI data. CFD simulations of the MRI data revealed recirculation within the airway, but no other areas of concern were discerned. The project was successful in verifying that 3D models suitable for simulation can be extracted from MRI data.

TABLE OF CONTENTS

LIST OF FIGURES

LIST OF TABLES

NOMENCLATURE

SYMBOLS

A – area

f – respiration rate

kg – kilogram

m – meter

$\dot{m}$ – mass flow rate

N – Newton

P – Pressure

Pa – Pascal

s – second

u – velocity in the x-direction

v – velocity in the y-direction; velocity

V – volume

$\dot{V}$ – volumetric flow rate

w – velocity in the z-direction

x – horizontal direction

y – vertical direction

z – dimensional direction normal to an xy-plane

μ – dynamic viscosity

ρ – density

τ – shear stress

ABBREVIATIONS

CAD – Computer Aided Design

CAE – Computer Aided Engineering

CFD – Computational Fluid Dynamics

DICOM – Digital Image and Communication in Medicine

ECG – Electrocardiography

FEA – Finite Element Analysis

FOV – Field of View

IRB – Institutional Review Board

MPR – Multiplanar Reconstruction

MRI – Magnetic Resonance Imaging

MSE – Master of Science in Engineering

MSOE – Milwaukee School of Engineering

NREM – Non-Rapid Eye Movement

NURB – Non-Uniform Rational Basis Spline

REM – Rapid Eye Movement

REU – Research Experience for Undergraduates

ROI – Region of Interest

RPC – Rapid Prototyping Center

STL – Stereolithography File Format

1. INTRODUCTION

A person's health is greatly affected by their ability to breath. For many people, this ability is impaired because of improper airflow within the nasal cavity, oral cavity, or the trachea. Blockages within these passages are primarily observed during a physical examination or a sleep study. In a physical examination, doctors discover blockages within the airways by observing the tissue within the oral cavity. Abnormalities in the oral cavity are a quick indication of where a blockage is occurring and immediately provide a path of action. If no blockages are observed, however, a sleep study is then utilized to observe the effect of the limited airflow.[1] One's inability to breath during sleeping is detrimental to their health. The lack of oxygen during a sleep cycle can reduce one's ability to stay in a non-rapid eye movement (NREM) sleep as well as the ability to reach a state of rapid eye movement (REM) sleep. The REM cycle is the period in one's sleep that provides the most amount of rest and is associated with a high amount of brain activity [1, 2]. Irregular sleep behavior (or sleep deprivation) greatly affects the body's neuron activity, which in turn negatively affects a person's mood, physical strength, focus, and memory [3, 4].

Invasive measures such as a video probe can be used to observe blockages that exist within the airways, but they provide little insight on the fluid flow properties. Any flow properties observed using a probe are inaccurate due to the change in the airway geometry and because of the introduction of another obstruction. Surgery within the

[1] Obstructions can exist deep within the airways and thus are not observable via a physical examination. These obstructions can occur for several reasons, two of which include physical abnormalities and fatty tissue placing restrictions on the air passages.

airways can improve the state of airflow, but the level of improvement is simply an estimate drawn from these medical examinations. The objective of this project was to evaluate a cine MRI's (magnetic resonance imaging) ability to determine the level of obstruction within the airways, as well as the MRI's effectiveness in treatment planning. Specifically, analysis of MRIs was to be performed using simulation results obtained within computational fluid dynamics (CFD) software. Initially, a model of a patient's airway would be generated using the MRI data obtained before and after surgery. The two models would then provide insight into resistance within the airways, as well the level of improvement generated through surgery. Because of time constraints, only pre-surgery data of a patient was provided. Because of this, CFD analysis of the airway was not compared to sleep studies. The final results of this project can serve as a reference for medical professionals to explore alternative, non-invasive methods of airway analysis.

2. PROJECT DESCRIPTION

The objective of this project was to evaluate an MRI's ability to determine the level of obstruction in human airways and its effect on air flow. Initially, this evaluation was to be made by comparing fluid flow simulations within CFD software to sleep studies performed on patients before and after surgery. A minimum of three airways were to be analyzed throughout the scope of the project. Additional airways were to be added, depending on the success of the CFD analysis. Because of time constraints, CFD analysis was only performed for a single patient prior to receiving surgery. As a result, no comparisons could be made to the patient's sleep study. The model of the airway was derived from the DICOM images that were provided by project advisors Dr. Ravi Elluru, M.D., Ph.D. and Dr. Maninder Kalra, M.D., Ph.D., both from Dayton Children's Hospital in Dayton, Ohio. A segmentation software program known as 3D Slicer was used to trace the fluid domain of the airways. The selected regions within each slice allowed for the development of the three-dimensional (3D) models. The geometry isolated within this program included mesh geometries that required manipulation prior to analysis.

The project consisted of two phases that corresponded to the Fall and Winter quarters offered at the Milwaukee School of Engineering (MSOE). The first phase of the project was performed in GE-797 during the 2016 Fall quarter, whereas the second phase was performed in GE-798 in the 2016-2017 Winter quarter. The first phase of the project focused on the preliminary tasks associated with the simulation and analysis. These tasks included the following:

- Developing the best method for isolating the airway geometry and creating the preliminary mesh models of the patient's airway.

- Refining models for simulation. This included the removal of unwanted mesh characteristics that could hinder simulation time.
- Determining a protocol that can be used to convert mesh geometry to traditional solid models used in CAD programs.
- Performing an initial set of simulations and identifying areas of improvement. From this, preliminary conclusions were drawn about the data provided on how improvements could be made for the second phase of the project.

The second phase of the project served as both an extension and a refinement period for all the work performed during the previous quarter. In this phase, time was invested in analyzing the cine MRI data that were provided and refining the boundary conditions used for simulation. Some of the tasks performed included the following:

- Determining the proper boundary conditions. An inlet mass flow rate was calculated based on published values for a patient's respiratory volume and rate.
- Defining a method of analyzing the cine MRI images. An image editing program was used to observe the changing cross-section of the patient's trachea.
- Performing CFD simulations on the airway model obtained from newly provided MRI data. These data allowed for the generation of an airway model that could not be created in the previous quarter.

Sections 3 and 4 of this document detail the research that was performed throughout the duration of this project. Section 3 highlights some of the literature that was found to be applicable to the work that was proposed, whereas Section 4 details the background information that was deemed necessary to the reader. Section 5 documents the analysis that was performed with the medical images that were provided. This section

of the report is split into two sub-sections that correlate to the two phases of the project. The work performed within these two quarters is concluded in Section 6.

3. REVIEW OF LITERATURE

A review of literature finds that previous studies have been performed in relation to airway dynamics. A study performed by H. Radhakrishnan and S. Kassinos reveals that the airflow within the trachea and upper bronchi is turbulent, thus removing the need for laminar analysis [5]. Despite this fact, it is common to see both laminar and turbulent models used in airway simulations and a comparison being made between the two results. Furthermore, the models analyzed in these simulations often assume a static structure, where in reality, the human airway is dynamic, with contracting and expanding walls. The nature in which this dynamic behavior occurs is out of the scope of this project; however, it has been discussed that it may be possible to observe the deflection (and therefore, stress) of internal tissue because of the variation of pressure with the airways.

Although static structures were used during the scope of this project, it was beneficial to review works pertaining to the movement of system walls. Tanaka *et al*. [6] studied the contracting and expanding of a small airway. In this study, the actual physical model did not change (thus, it was still a static structure). However, sinusoidal equations were used to control the mass flow rates associated with these contractions. The movement of the 3D model itself would have proven troublesome in terms of computational time. The final results of this study indicated that the dispersion of fluid particles increased because of the simulated effects on mass flow rate.

Work performed by Saksono *et al.* [7] and Lin *et al.* [8] stressed the influence of nasal cavity geometry on simulation results within the nasopharynx and oropharynx. Similar conclusions were drawn from the work performed within this project. Specifically, the angle at which air entered the larynx influenced the recirculation.

Efforts have been made to develop image technology that can capture the dynamic motion of organs and internal fluid. Doctors Moghari and Powell from Boston's Children Hospital have developed an imaging technique which they refer to as "3-D-cine" [9]. Currently, this technology has been limited to cardiac analysis and the tracking of blood flow. Internal anatomy is captured as a "3-D block", as opposed to two-dimensional (2D) image slices. In this technique, the patient is not required to hold their breath during the imaging process. The disadvantage of this technology is that it requires the use of a dye that enhances the color of blood within the equipment. The dependence of blood makes application of this technology to airway geometry questionable.

In addition to the findings described above, time was dedicated to reviewing work previously performed by researchers at MSOE. In 2013, CFD analysis was performed on a pediatric trachea in conjunction with the institution's Research Experience for Undergraduates program (REU). The study was performed by David Rutkowksi under the supervision of Dr. Subha Kumpaty [10]. The objective of this study was to compare the fluid flow properties of a normal airway compared to the flow properties affected by tracheomalacia, a condition which causes the collapse of the pediatric trachea [10]. Out of all of the information provided within the report, special attention was given to the data acquisition, data processing, and CFD simulation sections. Unlike the study proposed in this document, the work performed by Rutkowski utilized data obtained by computed tomography (CT) scanning. A CT scan entails a different process than a cine MRI that also allows for better extraction of airway geometry. The disadvantage with CT equipment is that it exposes individuals to a large amount of radiation, which can be

harmful to their health. Nonetheless, the data obtained from both sets of equipment are provided within the Digital Imaging and Communications in Medicine (DICOM) format.

Although the native data were provided in the DICOM format, it was revealed that the image slices of the airways were also provided and used for analysis. The images were then imported into a program called Materialise Mimics, which allows for the extraction of a 3D model of a patient's anatomy [11]. Refinement of this model was performed in a program called Magics and then converted in a program called 3-matic. [2] All of these programs were part of the Materialise Mimics® Innovation Suite, which specializes in computer-aided design on anatomy [12]. This is significant, as it provided insight into image processing that was used for this project. In addition, it was learned that an open source program known as 3D Slicer was a viable option for developing three-dimensional (3D) models. However, the review of programs detailed in Rutkowski's report suggested that the programs provided by Materilise would be a better option.

The boundary conditions used in Rutkowski's research were based on airway models performed by Luo, Hinton, Liew, and Tan [13]. These boundary conditions were based on a relatively high respiration rate and assumed a constant inlet velocity and zero-gauge pressure at the outlets. A no-slip condition was specified at the walls of the airways. A summary of model parameters is detailed in Table 1. It is assumed that these parameters remained constant for both inhalation and exhalation simulations.

[2] The program Magics no longer appears to be offered by Materialise.

Table 1: Summary of Model Parameters used by Luo, Hinton, Liew, and Tan [13].

Parameter Name	Value
Operating Pressure (P_a)	101 kPa
Density (ρ)	1.19 kg/m^3
Viscosity (μ)	$1.82 \cdot 10^{-5}$ kg/m·s
Inspiratory rate (f)	45 breathes/min
Inlet Velocity (v_i)	2.03 m/s
Reynolds Number (Re)	3012

Luo *et al.* [13] further confirm that the flow within the upper airways and trachea is primarily turbulent and is transitional for light breathing. However, because of the deceleration of air particles and relaminarisation (i.e., the transition from turbulent to laminar flow), the particle motion within the large trachea-bronchial airways is still unclear. This stresses the need for a refined airway model and a better understanding of the flow dynamics. Regardless of this information, the study performed by Luo *et al.* [13] utilized both laminar and turbulent flow models and compared their differences. This appears to be a common trend in airway analysis.

The remaining information available in Rutkowski's report does not provide any more insight into the simulations that are part of the scope of this project. The work completed by Rutkowski in the MSOE REU program served as a foundation for all the simulations in this project.

4. BACKGROUND

Given that this project is medical in nature, background research had to be performed to become familiar with some of the technology, sciences, and terminology that would be used. Specifically, research about the human airways, its effect on sleep, and MRIs as a means of analysis, had to be performed. An introduction to fluid mechanics and CFD has also been provided as background for the sciences involved during this study.

4.1 THE HUMAN AIRWAY

The human airway represents a significant portion of the respiratory system by serving as the pipelines in transferring oxygen-rich air into the lungs and expelling waste gases [14]. These pipelines are composed of the nasal cavities, mouth, larynx, trachea, and bronchi. With the exception of the mouth and nasal cavities, the airways are lined with small hairs known as cilia. It was to be determined at a later time (i.e, during simulation) how these hairs would be incorporated in the flow models or if their effect on airflow is negligible. The shape of these airways is important to the fluid flow that is experienced as well as to the health of individuals. Abnormalities or obstructions of air can significantly impair the amount of oxygen received by the lungs as well as cause discomfort. Furthermore, one's ability to breathe can greatly affect their ability to enjoy restful sleep. Sleep deprivation greatly affects the body's neuron activity, which in turn negatively affects a person's mood, physical strength, focus, and memory [3, 4].

For this project, the focus was on the study of air flow within trachea and bronchi. The geometry of these passages is illustrated in Figure 1, where a schematic of the human respiratory system is shown. As one will notice, the combination of these geometries

forms a y-shape whose inlets and outlets were expanded where needed for analysis. The boundary conditions (see Sections 4.1.2 and 4.3.2) used during simulation had to incorporate the breathing conditions for an individual at rest as well as when in a sleeping or relaxed state. The results from these two states were then to be used to make correlations between the fluid flow and sleep studies, but this step did not take place.

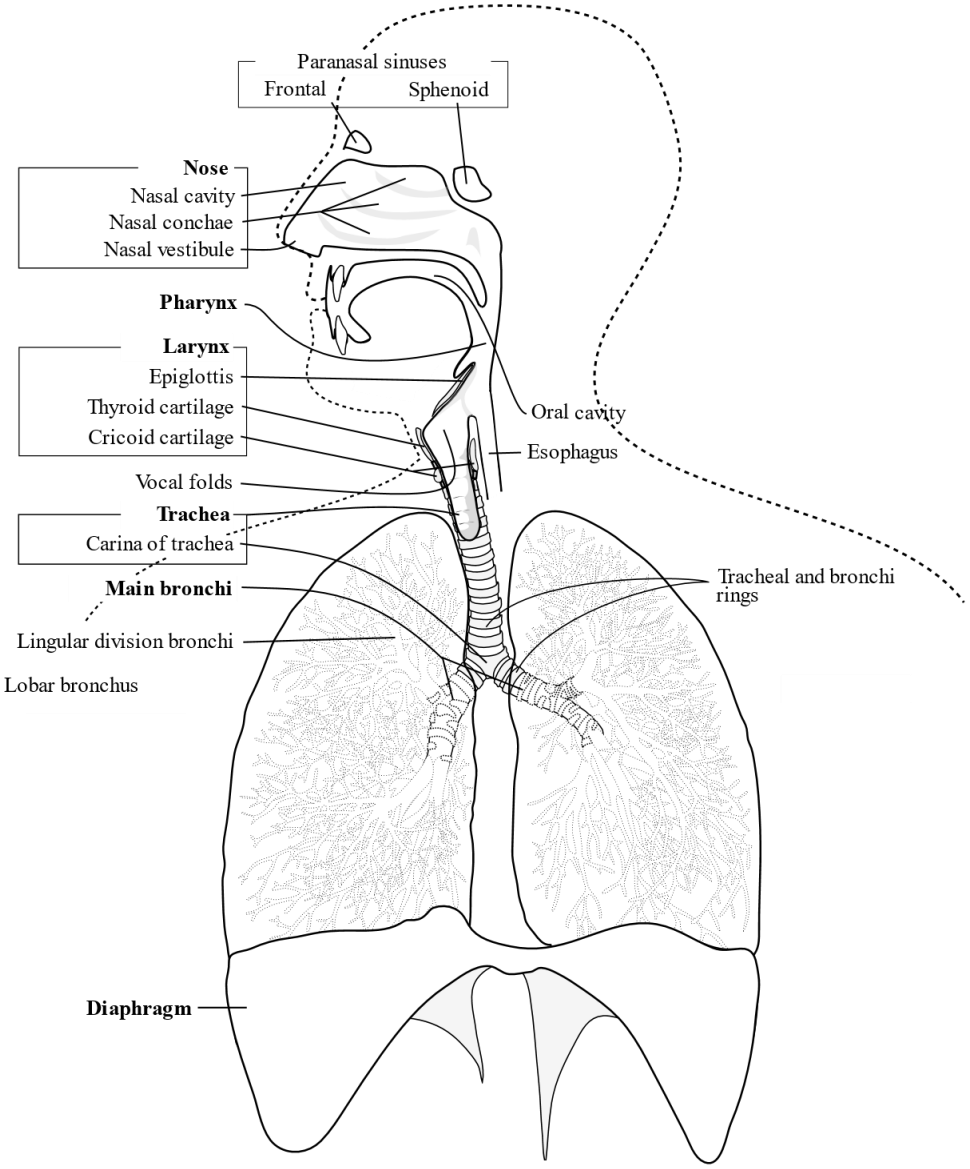

Figure 1: Schematic of Human Respiratory System [15].

4.1.1 Nasal and Oral Cavities

The nasal and oral cavities contain a more complex shape than the lower airway (i.e., the trachea and bronchi). The abruptly changing geometry of the upper airway requires that medical images taken in this region have a high resolution with a fine slice thickness (see Section 4.2.2). Although not a primary concern, three-dimensional (3D) models of the nasal and oral cavities are desirable if they can be obtained. Anatomical schematics were utilized to aid in the development of these models. Figure 2 through Figure 5 are a series of illustrations that were used for reference during the second phase of the project. These illustrations were obtained from a Gray's Anatomy text that highlighted the various anatomical components within an individual [16]. Figure 2 shows the location of the nasal cavity in relation to other cavities/regions within the head. The highlighted regions in this figure are general outlines. The internal geometry of the nasal cavity is better detailed in Figure 3. In this figure, one can see the various folds (or concha) that exist within the cavity, and also that it is divided into two by the nasal septum. This bifurcation rejoins at the nasopharynx, which eventually transitions into the patient's trachea. Thus, a total representation of the airway would result in an inhalation model that contained two inlets at the patient's nostrils and the two outlets at his or her bronchi.

Figure 4 details the location of the sinuses in correlation to the nasal cavity. In this figure, one can see that sinuses surround the nasal cavity, with smaller anatomical features existing within. The complex shape of the nasal cavity, along with the interacting tissue and bone, raises concerns on the ability of MRIs to capture the fluid domain.

Figure 5 shows how the geometry of the skull corresponds to the geometry of the nasal cavity. Coronal slices of a patient's head would provide better segregation of this region.

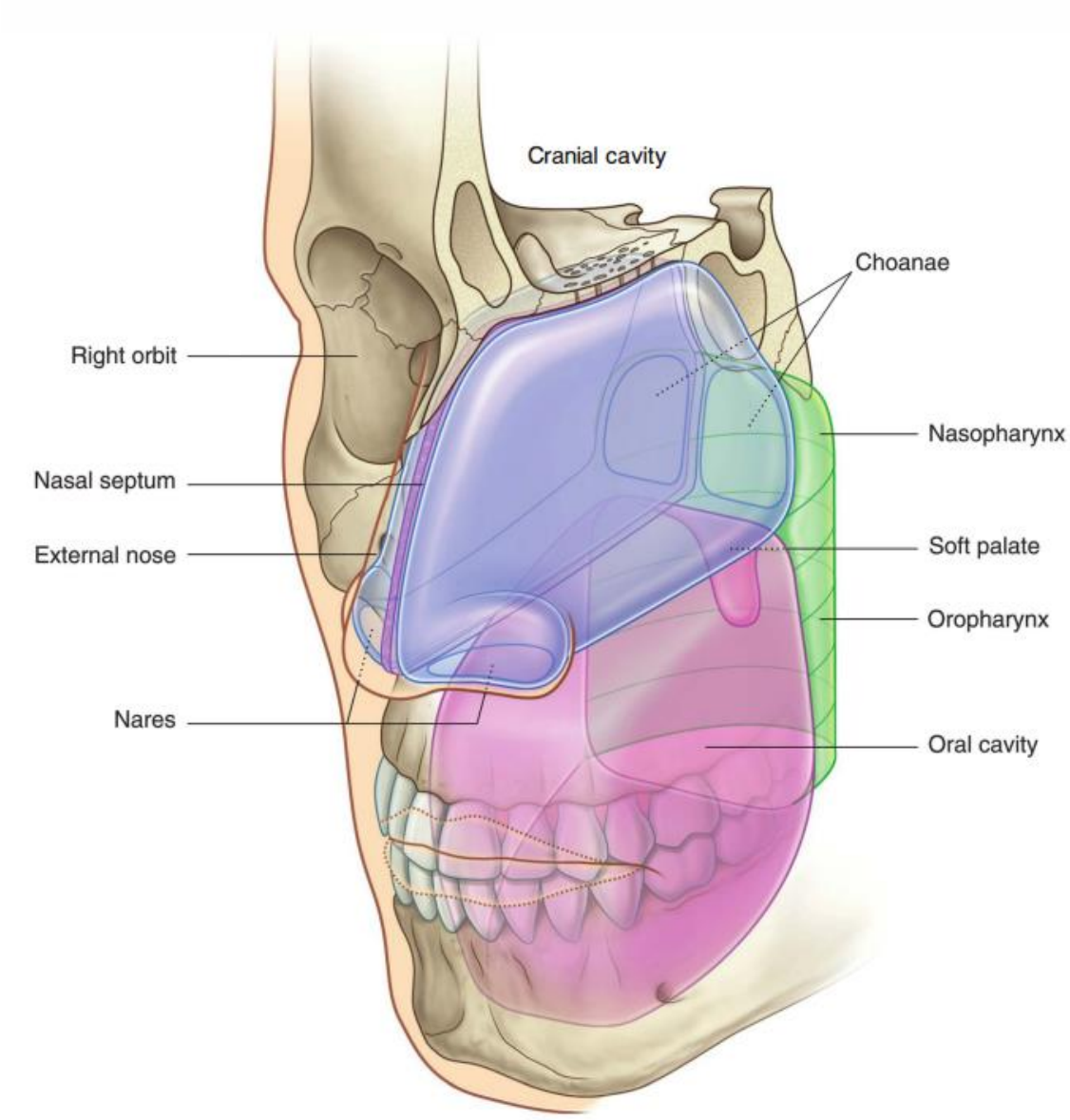

Figure 2: Nasal Cavity Relationship to Other Airway Cavities [16].

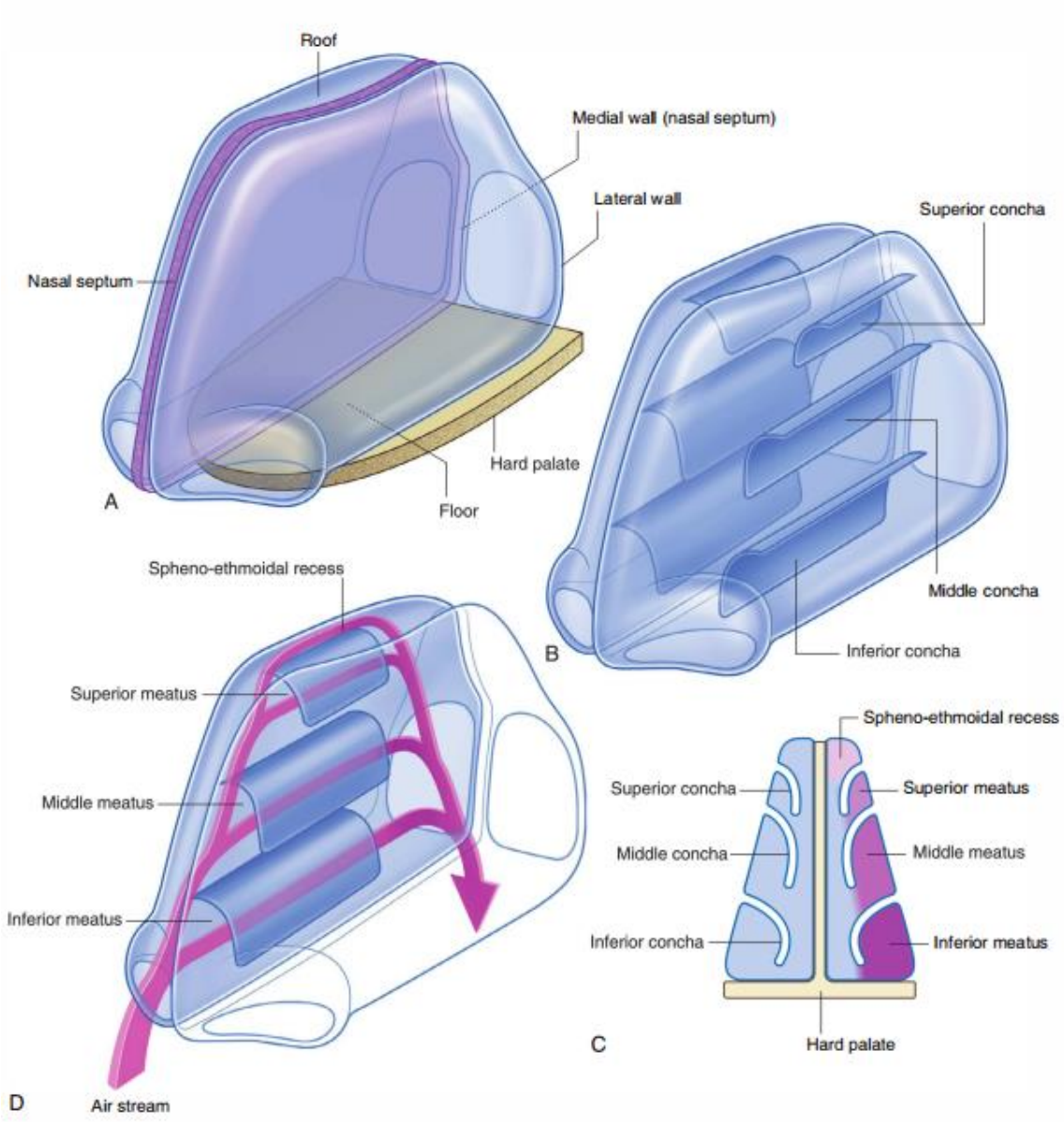

Figure 3: Illustrations of the Nasal Cavity [16]. (A) Overall Domain of Geometry. (B) Isometric View Detailing Internal Folds. (C) Coronal Cross-section. (D) Illustration of Internal Air Stream.

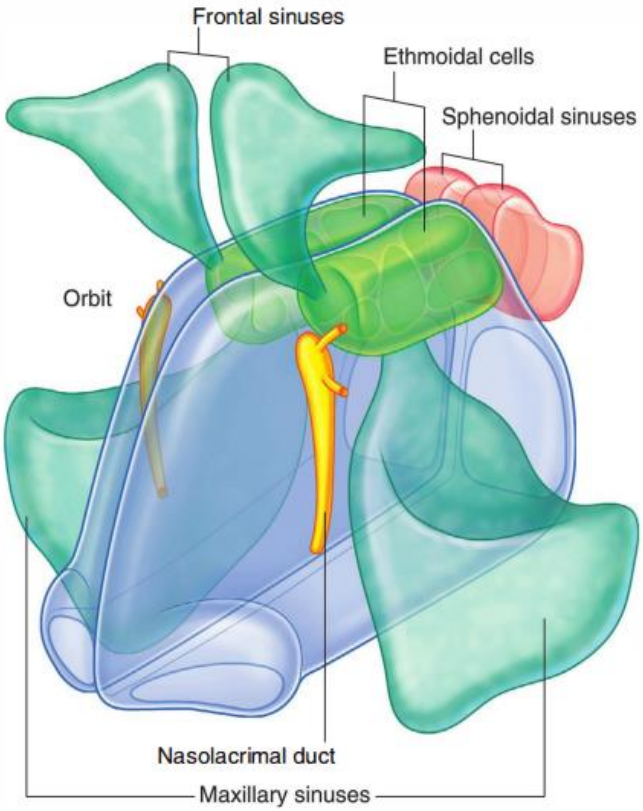

Figure 4: Location of Sinuses in Correlation to the Nasal Cavity [16].

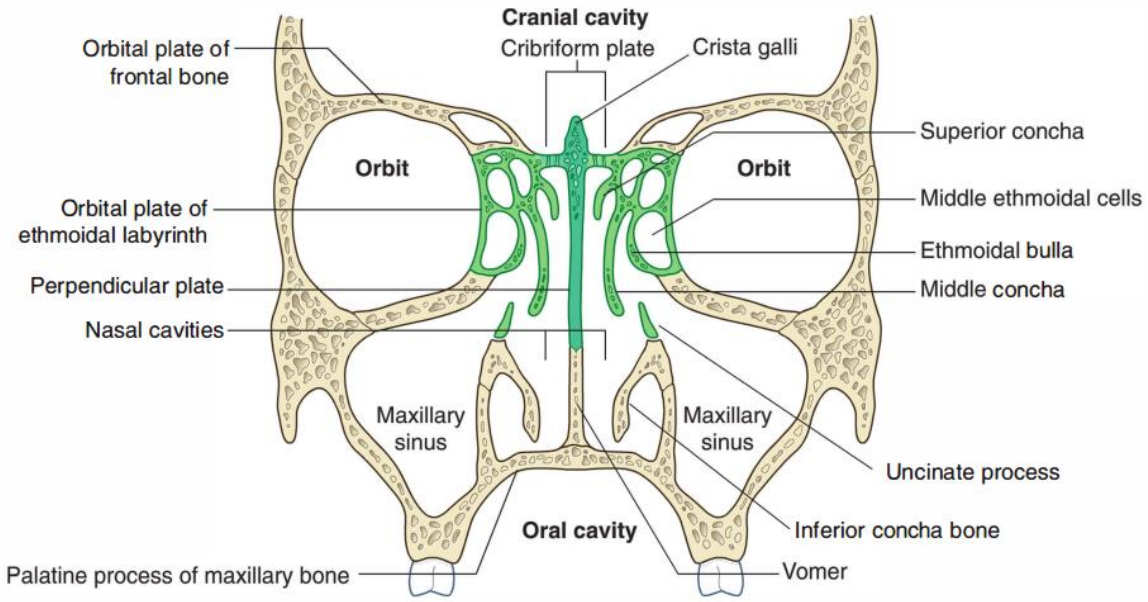

Figure 5: Coronal Cross-section of the Skull [16].

4.1.2 RESPIRATION

Human respiration occurs in sinusoidal pattern and has characteristics that are dictated by the amount and rate of air inhaled/exhaled. The vertical location of the sinusoid is dependent on the average amount of air within an individual's lungs. Figure 6 demonstrates the relationships between various lung volumes and capacities. As one will see, average respiration occurs in a small range and is surrounded by inspiratory and expiratory reserves. These reserves represent the maximum amount of air that one can voluntarily inhale or exhale beyond their typical respiration volume (tidal volume). For this project, only normal respiration functions were a concern for CFD simulations. Specifically, the average volumetric flow rate is desired from a patient's respiration pattern.

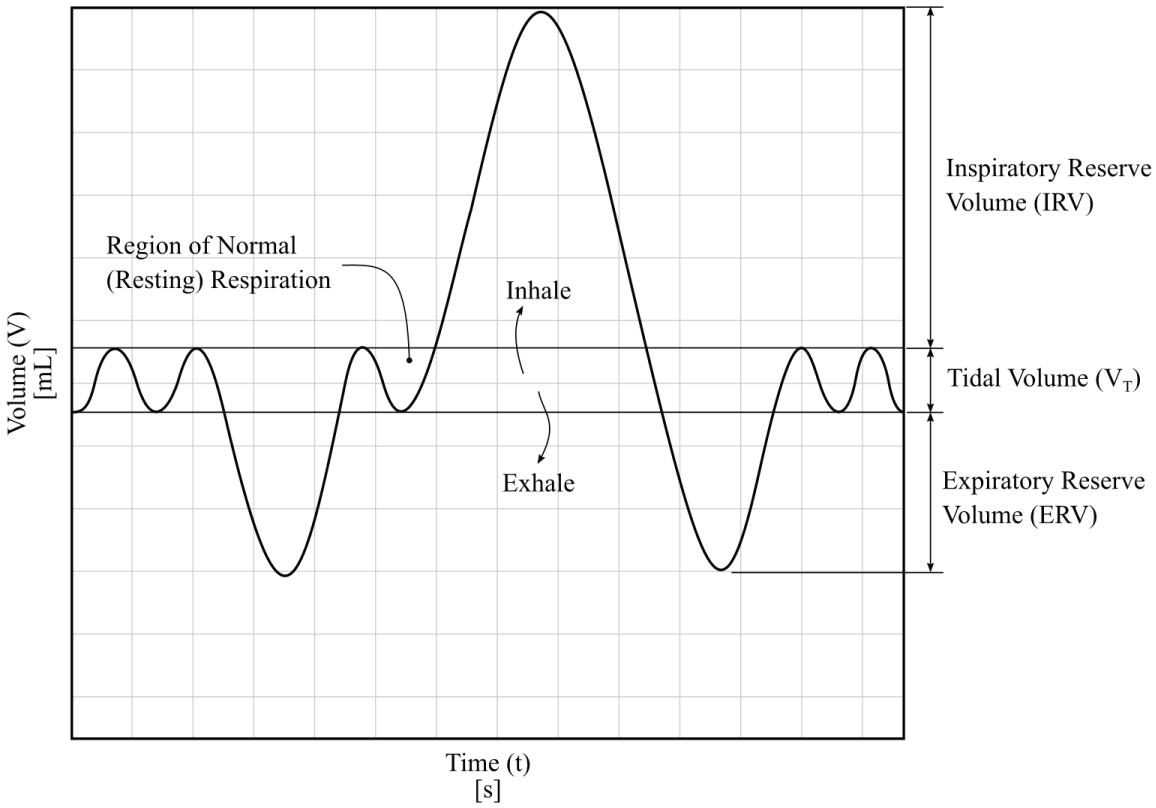

Figure 6: Lung Volumes and Capacities.

The volumetric flow rate of air entering (or exiting) the airway is calculated from an individual's tidal volume and respiration rate. Tidal volume is the amount of air one moves into or out of their lungs during a single respiration cycle, whereas respiration rate is the amount of breaths an individual makes within a minute [17]. The equation used to calculate the volumetric flow rate is

$$\dot{V} = V_T \cdot f, \tag{1}$$

where $\dot{V}$ is the volumetric flow rate in mL/s, V_T is the tidal volume in mL, and f is the respiratory rate in breaths/s. For an adult, the average tidal volume is 500 mL and the average resting respiration rate is 14 breathes/min [18, 19, 20]. This results in a general volumetric flow rate of approximately 116.7 mL/s for a resting adult.[3] This value is likely to differ slightly for an individual who is asleep. Thus, a sleeping volumetric flow rate would have to be determined (be it from documented or experimental data) before a comparison can be made between CFD simulations and sleep studies. Table 2 highlights common respiratory rates for both pediatric and adult patients. These ranges, along with a known tidal volume for a patient, can be used to develop simulation results that are unique to the patient being treated. Section 4.3.2 explains the derivation of boundary conditions that were used for simulation.

[3] A unit conversion is required for the respiration rate to achieve units of breaths/s.

Table 2: Common Respiratory Rates [18, 21].

Age Group	Respiration Rate (f) [breath/min]
Newborn (<1 months)	30-60
Infant (1-12 months)	30-60
Toddler (1-2 years)	24-40
Preschooler (3-5 years)	22-34
School Age (6-12 years)	18-30
Adolescent (13-17 years)	12-16
Adult (18+ years)	12-16

4.2 MEDICAL IMAGING

4.2.1 MEDICAL DIRECTIONS AND ORIENTATIONS FOR 3D SPACE

The three-dimensional (3D) space in which the human body is defined to exist is labeled using nomenclature different from engineering, manufacturing, or 3D modeling. The six spatial directions -- top, bottom, front, back, left, and right -- are referred to using the adjectives superior, inferior, posterior (or dorsal), anterior (or ventral), right, and left, respectively. These directions are illustrated in Figure 7, where they have been labeled using the first letter of each word. The orthogonal planes that exist in this 3D space are also given specific names. The axial plane refers to the normal cross-section that cuts the

body from the superior or inferior directions. This plane is analogous to an XY plane in the Cartesian coordinate system. The coronal plane refers to the cross-section that intersects the human body normal to the anterior and posterior directions. This plane is analogous to the YZ plane. Finally, the sagittal plane is the plane normal to the right and left directions and is equivalent to the XZ plane.

The location of origin within this system is defined by the user and is dependent on the operation at hand. For an MRI, the origin is defined before the study using an operation known as the 3-plane localizer (or "3-PLANE LOC").[4] The images taken during this localization are low in resolution and have a large field of view (FOV), and were used to plan the location of scans within the study.

[4] It is uncertain if a single point is defined as the origin/point of reference during the localizer operation. All that could be confirmed is that this step is very much required because it is used to plan the location of each image taken during the MRI study. It is the professional opinion of the author that the MRI equipment has a global origin in which operates and that localization is part of planning the 3D acquisition.

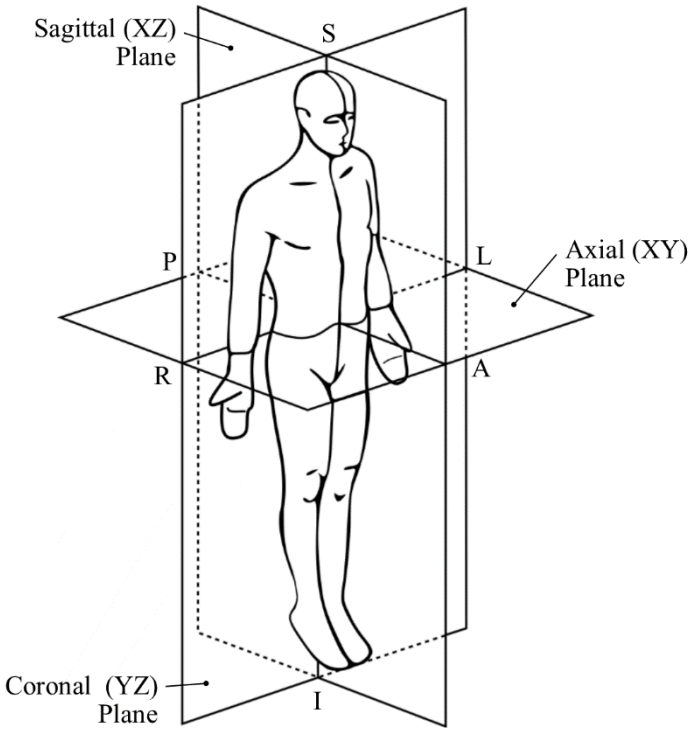

Figure 7: Medical Planes and Anatomical Orientations.

4.2.2 Image Quality and Acquisition

The quality of the 3D models that were created during this project were dependent on the slice thickness and pixel size of the 2D CT/MRI images provided. Every CT and MRI image is constructed of a square matrix whose size can range anywhere from 320 x 320 to 1024 x 1024 elements [22]. The matrix size and the field of view (FOV) of the image(s) are then used to determine the pixel size. This relationship is shown in Equation (2) [22],

$$p = \frac{FOV}{n}, \tag{2}$$

where p is the pixel size in mm, FOV is the field of view of the image in mm, and n is dimensionless and represents the size of the square matrix. A small pixel size is favorable, as it results in a high-resolution image. Special considerations are required

with MRIs, however, due to noise that is introduced at higher resolutions. One must observe the signal-to-noise ratio (SNR) while capturing the images. Increasing the resolution of a scan above an acceptable range can produce grains in images because of low SNR, whereas the reverse will result in blurry images because of high SNR [23]. The SNR is proportional to the volume of the voxel, the three-dimensional (3D) element that is created from the pixel size and slice thickness used [22]. Figure 8 illustrates the relationship that exists between the matrix size, FOV, pixel size, and the created voxel(s). The voxel volume can be calculated using Equation (3) for a square pixel [22]:

$$V_{vox} = p^2 \cdot t, \tag{3}$$

where V_{vox} is the voxel volume in mm^2, p is the pixel size in mm, and t is the slice thickness in mm. The slice thickness used in a CT/MRI study is dependent on the area of interest and is typically determined by the best opinion of the operator/radiologist. Considerations include acquisition time, image quality, and the health of the patient. A small slice thickness is desirable for the generation of the three-dimensional (3D) models, because it allows for the capture of fine details; however, the procedure should not be abused when using CT because of the radiation exposure given to the patient (see Section 4.2.3.1).

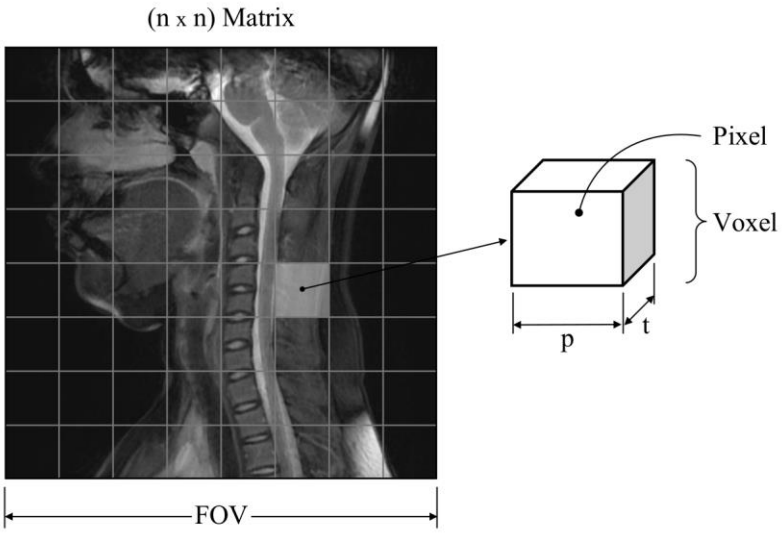

Figure 8: Correlation Between Matrix Size, FOV, Pixel Size, and Voxel Volume.

4.2.3 CT VERSUS MRI

4.2.3.1 COMPUTED TOMOGRAPHY (CT)

CT scans capture the internal anatomy of an individual with the use of high energy X-rays. The cross-sectional images obtained using CT are achieved by the rotation of an X-ray tube around a patient [22]. The grayscale brightness seen in a CT scan is proportional to the degree of X-ray attenuation by a tissue, which then can be correlated to physically density [24]. CTs operate on what is known as the Hounsfield scale. The Hounsfield scale is a method of correlating the radiodensity of a material to that of distilled water and air [22, 25]. The Hounsfield unit of a material can be calculated using Equation (4), where υ is the linear attenuation coefficient of the material and υ_{water} and υ_{air} are the linear attenuation coefficient of water and air with values of 0 HU and -1000 HU, respectively [25]. Thus,

$$HU = 1000 \cdot \frac{\upsilon - \upsilon_{water}}{\upsilon_{water} - \upsilon_{air}}. \quad (4)$$

Figure 9 is an illustration of the Hounsfield scale [26]. The minimum Hounsfield unit (or CT number) is -1000 HU for air and is displayed black. Bone and other dense materials are displayed white and are on the opposite end of the scale. The traditional Hounsfield scale operates on a range going from -1000 HU to 1000 HU; however, advances in medical equipment have increased the top range to approximately 3000 HU [27]. The human eye is unable to accurately distinguish between the 4000 shades of gray; thus, a windowing technique is sometimes used to reduce the spectrum close to the 256 shades of gray that can be displayed on a digital display [26]. CT is typically more common because of its availability and high resolution; however, it should not be abused. Although CT scans amount to approximately 6% of X-ray examinations, they contribute to more than 43% of the radiation dose resulting from those procedures [28].

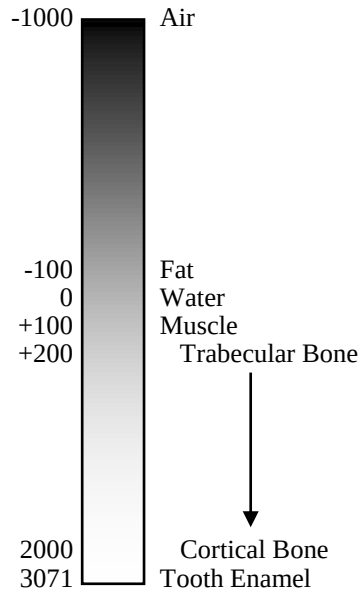

Figure 9: Hounsfield Scale [26].

4.2.3.2 MAGNETIC RESONANCE IMAGING (MRI)

MRIs function by exciting the protons (hydrogen ions) in tissue using magnets and interpreting the frequencies generated from their oscillation. Unlike CT scans, the

color scale seen in an MRI does not directly correlate to the physical density of the tissue. In fact, the shades of gray associated with tissue are dependent on the protocol, whereas the number of shades is determined from the FOV that is analyzed [24]. The MRI gray-scale is scaled relative to the voxel, with the largest signal strength (i.e., the brightest). This allows for inconsistencies between studies because the signal strength is dependent both on the tissue types and the applied magnetic field [24]. MRIs have the benefit of not using ionizing radiation, but suffer from lower quality and longer acquisition times when compared to CT. For this reason, the two methods are used interchangeably, with CT generally being more common [22].

4.2.4 CINE MRI

The term *cine* is an adjective used to describe the use of cinematography (i.e., the creation of a video). Cine MRIs allow medical professionals to observe firsthand the internal workings of a patient's body without the need for an incision. A patient is equipped with an ECG device that allows for the MRI equipment to take images at certain points within the patient's heartbeat [29]. These various segments are then stitched together to develop a video showing the movement of tissue and cardiac functions, such as blood flow. Cine MRIs also provide the ability to observe the flow of cerebrospinal fluid within the brain [30].

4.2.5 LIMITATIONS

Advances in medical imaging are occurring at a rapid pace, especially in fields that focus on the brain and the cardiovascular system. Functional MRIs (fMRIs) and 4D MRIs rely on the ability to track the movement of blood flow using blood-oxygen-level dependent (BOLD) contrast [31]. This contrast allows for doctors to observe the flow of

blood within the heart, as well as neural activity in real time. Unfortunately, air flow within the respiratory system cannot be observed, because it appears as empty space (black). Instead, the movement of air has to be simulated. This involves a detailed understanding of the boundary conditions in place and requires much more computational power. Furthermore, simulations have the disadvantage of not being real time, as the solution methods require a number of iterations (see Section 4.4). A number of assumptions can be introduced to reduce the computation time and the complexity of the simulation, but inversely, the assumptions reduce the accuracy.

Limitations also exist in the ability to capture the dynamic geometry of internal anatomy. Currently, there is no feasible way to capture the three-dimensional (3D) changing geometry. This process would require a tremendous amount of time, because it would entail taking multiple axial slices at various points in a patient's heartbeat. The number of images in a traditional CT/MRI would increase by a multiple equal to the number of frames desired in the cinematic. For example, a 60-image MRI would increase to 7,200 images for a 120-frame cinematic. For this reason, this project focused on analyzing the changing geometry in a single cross section, with assumptions made about its shape.

4.3 Fluid Dynamics

4.3.1 Fluid Behavior

A fluid is defined as a substance that deforms continuously under the action of any shear stress. That is, when a fluid is brought into contact with a moving surface, the fluid should move or deform no matter the magnitude of the force applied. There are two types of fluids that exist: Newtonian and non-Newtonian. In a Newtonian fluid, the

viscosity of the fluid remains the same as the shear rate applied to the fluid that is changed. This means that the viscosity is independent of the shear stress being applied. This makes the viscosity a property of that fluid. The opposite is true for non-Newtonian fluids. The viscosity of a non-Newtonian fluid is dependent on the rate of shear stress being applied, resulting in one of two characteristics: a shear-thinning or a shear-thickening fluid. In a shear-thinning fluid, the amount of resistive drag is decreased as the rate of shear stress is increased (i.e., a decrease in viscosity). A shear-thickening fluid follows the opposite trend in that the viscosity will increase as shear rate increases [32]. This relationship is summarized [32] by Equation (5):

$$\tau = \mu \cdot \frac{\partial u}{\partial y}, \tag{5}$$

where τ is the shear stress in units of N/m^2, μ is the dynamic viscosity of the fluid in units of $N \cdot s/m^2$, and $\partial u/\partial y$ is the rate at which the shear is being applied in units of s^{-1}. The symbol ∂u denotes the change in horizontal velocity in m/s, whereas ∂y is an indication that the change is with respect to vertical position in meters. Given that fluids exist in three dimensions, the shear stress applied on a fluid can be calculated per the direction of force. This would require the proper change of velocity and direction within the partial derivative.

Fluid flow can also be categorized as being compressible or incompressible depending on the variation of density (ρ) within a system. An incompressible fluid is defined as fluid whose density remains constant with respect to both time and space. This is represented mathematically [32] by Equation (6):

$$Incompressible: \frac{d\rho}{dt} = 0;\ \nabla\rho = \ 0. \tag{6}$$

In this equation, ρ is the fluid density in kg/m^3 and the variable t indicates time in seconds. A compressible fluid is a substance whose density is dependent on the system in which it exists. The value of the fluid density can change both in respect to time and space [32], as shown by Equation (7):

$$Compressible: \frac{d\rho}{dt} \neq 0;\ \nabla\rho \neq\ 0. \tag{7}$$

Liquids are usually classified as incompressible substances because their change of density is virtually unaffected by changes in pressure. Gases, on the other hand, are classified as highly compressible due to the free movement and spacing of their internal molecules. To reduce computational complexity, it often becomes beneficial to model gases as incompressible. This can be done if density changes are less than 5 percent throughout a system, and it is traditionally the case when flow velocity is less than 30% the speed of sound (approximately under 100 m/s) [32].

4.3.2 Boundary Conditions

The velocity of a fluid in contact with a surface or wall is equal to zero because of the no-slip condition caused by fluid viscosity [32]. This condition results in a transition of velocities from the wall to the remaining internal flow of the fluid, generating what is known as a velocity profile. The transition from viscous flow to the inviscid internal flow is known as a boundary layer [33]. A boundary layer can be separated into various sublayers whose number is dependent on whether laminar or turbulent flow exists. Figure 10 illustrates the development of both laminar and turbulent boundary layers over a flat plate.

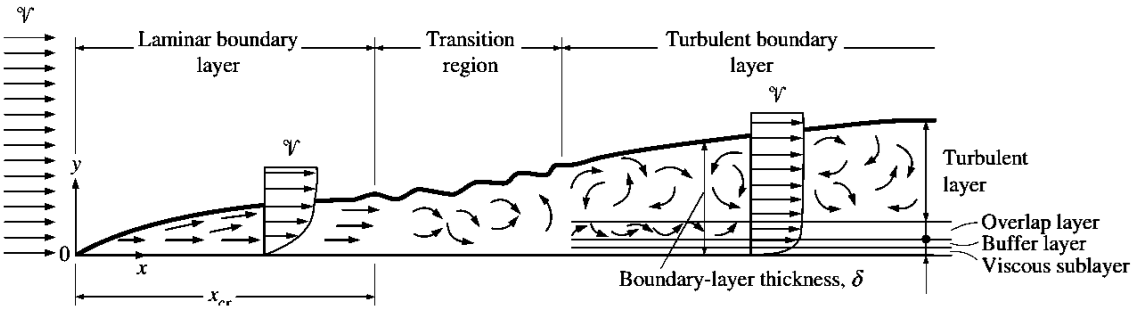

Figure 10: Boundary Layer Development over a Flat Plate [32].

The importance of boundary layers is that they require special attention when analyzing flow characteristics. In CFD analysis, finer meshes are typically required near walls to capture fluid behavior. This technique is known as the two-layer zonal model approach and was implemented in the CFD analysis in this project [33]. Special equations are also used near walls and are dependent on the solution model that is used.

In addition to these conditions, it is imperative that the proper boundary conditions for velocity and pressure be defined within a model. Versteeg and Malalasekera point out that the most common cause of rapid divergence of CFD simulations is the inappropriate selection of boundary conditions [34]. The number of boundary conditions that are known is dependent on the problem being solved; however, it is best to know conditions at the inlet, outlet, and walls. Figure 11 illustrates the combination of boundary conditions that are required for "simple flow".[5]

[5] The term *simple flow* can be used to express a large number of systems. *Complex flows* would require the introduction of moving components and other unique system characteristics.

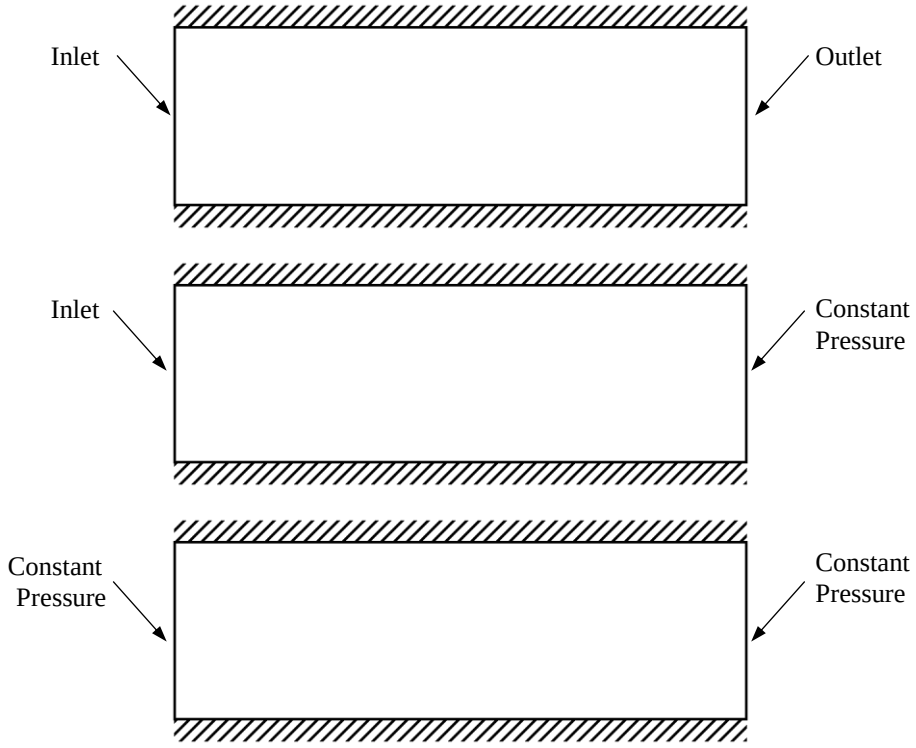

Figure 11: Boundary Condition Configurations for Simple Flow [34].

In addition to the configuration in Figure 11, the following list summarizes the allowed combination of boundary conditions [34]:

- walls and inlet and at least one outlet
- walls and inlet and at least one constant pressure boundary
- walls and constant pressure boundaries

The *Introduction to Computational Fluid Dynamics* by Versteeg and Malalasekera [34] notes that special care is required when working with systems that have more than one outlet. This happens to be the case when modeling the human trachea whose bronchi split between the right and left lung. Exit pressures govern the flow split between multiple outlets, meaning it is better to specify these values rather than to use a zero-pressure gradient condition.

During the first phase of the project, the boundary conditions in Table 1 were utilized for CFD simulations. The fluid properties and inlet velocity used within this table, however, do not necessarily apply to everyone. For the second phase of the project, more time was dedicated for developing boundary conditions that would be unique to the patient being analyzed. The fluid properties required for simulation are the density and viscosity of air. These values are dependent on the operating temperature and pressure acting on the fluid. The density of air was calculated using the ideal gas law [35],

$$\rho = \frac{P}{R \cdot T}, \tag{8}$$

where ρ is the fluid density in kg/m^3, P is the ambient pressure in Pa, R is the specific gas constant for air with a value of 287 J/(kg·K), and T is the operating temperature in K. Atmospheric pressure of 101.325 kPa and an average body temperature of 36.85°C were used for calculation [18]. This resulted in approximate air density of 1.139 kg/m^3.

The corresponding viscosity of the air was then calculated utilizing the power law [35], which states

$$\mu = \mu_0 \cdot \left(\frac{T}{T_0}\right)^{0.7}, \tag{9}$$

where μ_0 is the absolute viscosity of air with a value of $1.71 \cdot 10^{-5}$ kg/(m·s), T is the operating temperature in K, and T_0 is the absolute temperature with a value of 273 K. Using Equation (9), the viscosity of air for average body temperature was calculated to be approximately $1.869 \cdot 10^{-5}$ kg/(m·s). It should be noted that the power law used here is a simpler alternative to the Sutherland law that can also be used to correlate viscosity and temperature [32, 35].

The mass flow rate or air within the airway was then calculated utilizing the average volumetric flow rate from Section 4.1.2, and the air density calculated above using Equation (8). The relationship between these values is shown by Equation (10),

$$\dot{m} = \dot{V} \cdot \rho_{air}, \tag{10}$$

where $\dot{m}$ represents the mass flow rate of the fluid in units of kg/s, $\dot{V}$ is the volumetric flow rate in mL/s, and ρ_{air} is the density of air in kg/m^3. Not shown in Equation (10) is a conversion of 10^6 mL/m^3 that is required to cancel out the volume terms. Upon calculation, the mass flow rate for a resting adult was approximated to be $1.329 \cdot 10^{-4}$ kg/s. Table 3 is a summary of the model parameters that were developed for the second phase of the project. The values shown in this table were used to replace the values shown in Table 1. The primary reason for this is that Table 3 utilizes a mass flow rate boundary condition as opposed to a velocity. Mass flow rate can be applied to any airway model of a patient with similar physical criteria (i.e., similar tidal/respiration volume, respiration rate), regardless of the inlet cross-sectional area.

Table 3: Simulation Parameters for a Resting Adult.

Parameter Name	Value
Operating Pressure (P)	101.325 kPa
Ambient Temperature (T_{amb})	36.85°C
Density (ρ)	1.139 kg/m^3
Viscosity (μ)	$1.869 \cdot 10^{-5}$ kg/m·s
Inspiratory Rate (f)	14 breaths/min
Mass Flow Rate ($\dot{m}$)	$1.329 \cdot 10^{-4}$ kg/s

4.4 COMPUTATIONAL FLUID DYNAMICS (CFD)

Computational fluid dynamics functions by discretizing the governing equations of fluid flow, which is similar to how mechanics of materials are discretized in finite element analysis (FEA). Discretization of fluid models allows for the governing partial differential equations to be represented as linked algebraic expressions. The governing equations are known as the Navier-Stokes equations and are made up of continuity and momentum expressions for a fluid in all spatial dimensions. Equation (11) illustrates the continuity equation and Equation (12) through Equation (14) represent the momentum equations for the x, y, and z direction, respectively. These equations are written for compressible, Newtonian, viscous flow [36, 37]:

$$\frac{\partial \rho}{\partial t} + \frac{\partial(\rho u)}{\partial x} + \frac{\partial(\rho v)}{\partial y} + \frac{\partial(\rho w)}{\partial z} = 0, \tag{11}$$

$$\frac{\partial(\rho u)}{\partial t} + u\frac{\partial(\rho u)}{\partial x} + v\frac{\partial(\rho u)}{\partial y} + w\frac{\partial(\rho u)}{\partial z} = \frac{\partial P}{\partial x} + \mu\left(\frac{\partial^2 u}{\partial x^2} + \frac{\delta^2 u}{\delta y^2} + \frac{\delta^2 u}{\delta z^2}\right) + \rho f_x, \tag{12}$$

$$\frac{\partial(\rho v)}{\partial t} + u\frac{\partial(\rho v)}{\partial x} + v\frac{\partial(\rho v)}{\partial y} + w\frac{\partial(\rho v)}{\partial z} = \frac{\partial P}{\partial y} + \mu\left(\frac{\partial^2 v}{\partial x^2} + \frac{\delta^2 v}{\delta y^2} + \frac{\delta^2 v}{\delta z^2}\right) + \rho f_y, \tag{13}$$

$$\frac{\partial(\rho w)}{\partial t} + u\frac{\partial(\rho w)}{\partial x} + v\frac{\partial(\rho w)}{\partial y} + w\frac{\partial(\rho w)}{\partial z} = \frac{\partial P}{\partial z} + \mu\left(\frac{\partial^2 w}{\partial x^2} + \frac{\delta^2 w}{\delta y^2} + \frac{\delta^2 w}{\delta z^2}\right) + \rho f_z. \tag{14}$$

The variables u, v, and w indicate the velocity components in m/s for the x, y, and z directions, respectively. The variable P represents pressure in units of N/m^2 (or Pa) and the variable f is a source term that is used when applicable. If the density of the fluid is assumed to be constant (i.e., incompressible fluid flow), it can be removed from the partial derivatives within the momentum equations and removed completely from the continuity equation. Further simplification can be made if the source term f is also neglected. These simplifications [36] are shown in Equation (15) through Equation (18):

$$\frac{\partial u}{\partial x} + \frac{\partial v}{\partial y} + \frac{\partial w}{\partial z} = 0, \tag{15}$$

$$\rho\left(\frac{\partial u}{\partial t} + u\frac{\partial u}{\partial x} + v\frac{\partial u}{\partial y} + w\frac{\partial u}{\partial z}\right) = \frac{\partial P}{\partial x} + \mu\left(\frac{\partial^2 u}{\partial x^2} + \frac{\delta^2 u}{\delta y^2} + \frac{\delta^2 u}{\delta z^2}\right), \tag{16}$$

$$\rho\left(\frac{\partial v}{\partial t} + u\frac{\partial v}{\partial x} + v\frac{\partial v}{\partial y} + w\frac{\partial v}{\partial z}\right) = \frac{\partial P}{\partial y} + \mu\left(\frac{\partial^2 v}{\partial x^2} + \frac{\delta^2 v}{\delta y^2} + \frac{\delta^2 v}{\delta z^2}\right), \tag{17}$$

$$\rho\left(\frac{\partial w}{\partial t} + u\frac{\partial w}{\partial x} + v\frac{\partial w}{\partial y} + w\frac{\partial w}{\partial z}\right) = \frac{\partial P}{\partial z} + \mu\left(\frac{\partial^2 w}{\partial x^2} + \frac{\delta^2 w}{\delta y^2} + \frac{\delta^2 w}{\delta z^2}\right). \tag{18}$$

The discretization of the computational domain requires the use of a staggered grid between the values of pressure and velocity. The staggered grid is required to overcome some of the shortcomings associated with the central difference scheme of the discretized Navier-Stokes equations [38]. The primary cause of this shortcoming is that the central difference scheme is incapable of detecting flow direction and is unstable for illogical velocity and pressure distributions [39]. Figure 12 details the staggered grid that is utilized in a two-dimensional (2D) flow field. The solid circles represent values of pressure, P, the hollow circles represent horizontal velocity values, u, and the crosses represent vertical velocities, v. A two-dimensional (2D) grid is shown here for the sake of simplicity and will be used for the remaining theory. This grid and equations are expanded for three-dimensional (3D) problems by the introduction of the velocities normal to the xy-plane (i.e., velocities in the z-direction).

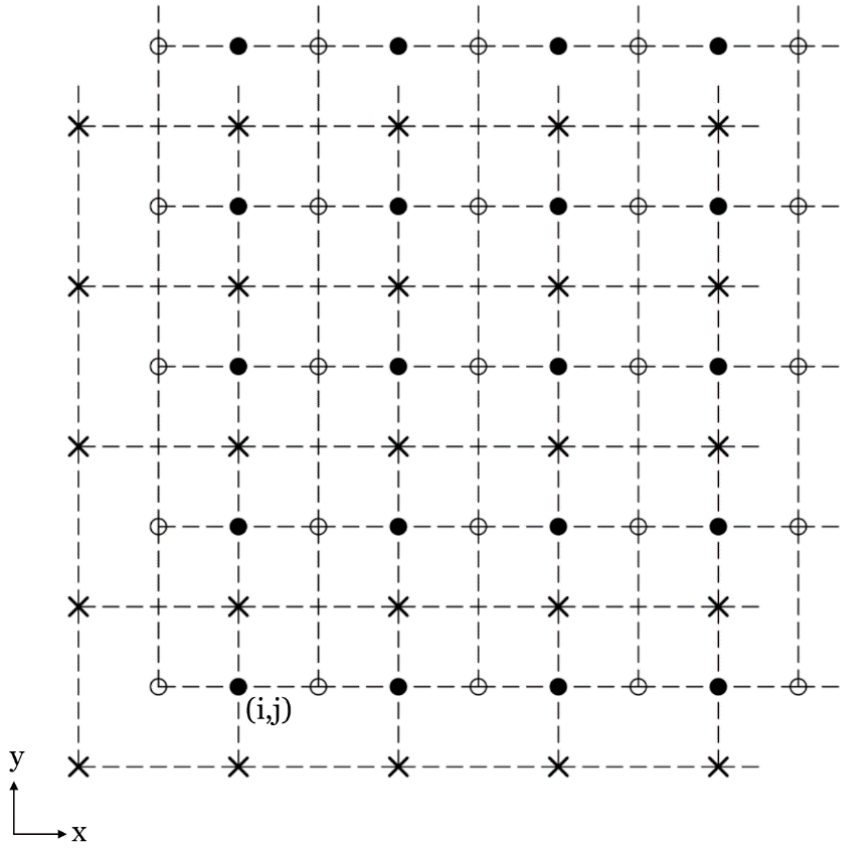

Figure 12: Staggered Computational Grid.

Once the grid system has been defined, the Navier-Stokes equations can be discretized about the pressure nodes within the grid. Equation (19) details the central difference continuity equation about a pressure point (i,j) [38]. The subscript i and j, respectively, indicate the horizontal and vertical location within the grid. As one can see, each variable is a half-step away from another and a full half-step away from itself. The central difference scheme used in the continuity equation utilizes velocities a half-step away in all four directions. Thus,

$$\frac{u_{(i+1/2,j)}-u_{(i-1/2,j)}}{\Delta x}+\frac{v_{(i,j+1/2)}-v_{(i,j-1/2)}}{\Delta y}=0. \tag{19}$$

The momentum equations are derived in a similar way. Each partial derivative within the momentum equations are determined using a central difference Taylor series expansion. Equation (20) and Equation (21) are the discretized momentum equation in the x and y direction, respectively [38]. The x-momentum equation is derived about a horizontal velocity point located at (i+1/2,j), whereas the y-momentum equation is derived about a vertical velocity point located at (i,j+1/2). Again, these grid locations are with respect to a pressure point (i,j). Thus,

$$\rho\left(\frac{u^{n+1}_{i+1/2,j}+u^{n}_{i+1/2,j}}{\Delta t}-\frac{(u^2)^n{}_{i+3/2,j}-(u^2)^n{}_{i-1/2,j}}{2\Delta x}+\frac{(u\bar{v})^n{}_{i+1/2,j+1}-(u\bar{v})^n{}_{i+1/2,j-1}}{2\Delta y}\right)= -\frac{P^n_{i+1,j}-P^n_{i,j}}{\Delta x}+\mu\left(\frac{u^n_{i+3/2,j}-2u^n_{i+1/2,j}-u^n_{i-1/2,j}}{(\Delta x)^2}+\frac{u^n_{i+1/2,j+1}-2u^n_{i+1/2,j}-u^n_{i+1/2,j-1}}{(\Delta y)^2}\right), \tag{20}$$

$$\rho\left(\frac{v^{n+1}_{i,j+1/2}+v^{n}_{i,j+1/2}}{\Delta t}-\frac{(v\bar{u})^n{}_{i+1,j+1/2}-(v\bar{u})^n{}_{i-1,j+1/2}}{2\Delta x}+\frac{(v^2)^n{}_{i,j+3/2}-(v^2)^n{}_{i,j-1/2}}{2\Delta y}\right)= -\frac{P^n_{i,j+1}-P^n_{i,j}}{\Delta y}+\mu\left(\frac{v^n_{i+1,j+1/2}-2v^n_{i,j+1/2}-v^n_{i-1,j+1/2}}{(\Delta x)^2}+\frac{v^n_{i,j+3/2}-2v^n_{i,j+1/2}-v^n_{i,j-1/2}}{(\Delta y)^2}\right). \tag{21}$$

The subscripts within the momentum equations indicate the nodal locations in space, whereas the non-numeric superscripts are an indication of a point in time. Specifically, the superscript n+1 indicates a value in the next point in time (i.e., the next time step) and n indicates the current point in time (or current values). The bar notation represents average values of velocities that have to be calculated because of the lack of a value at the specified grid point. This is shown in Figure 13 and Figure 14, where the computational domain of each discretized momentum equation is illustrated.

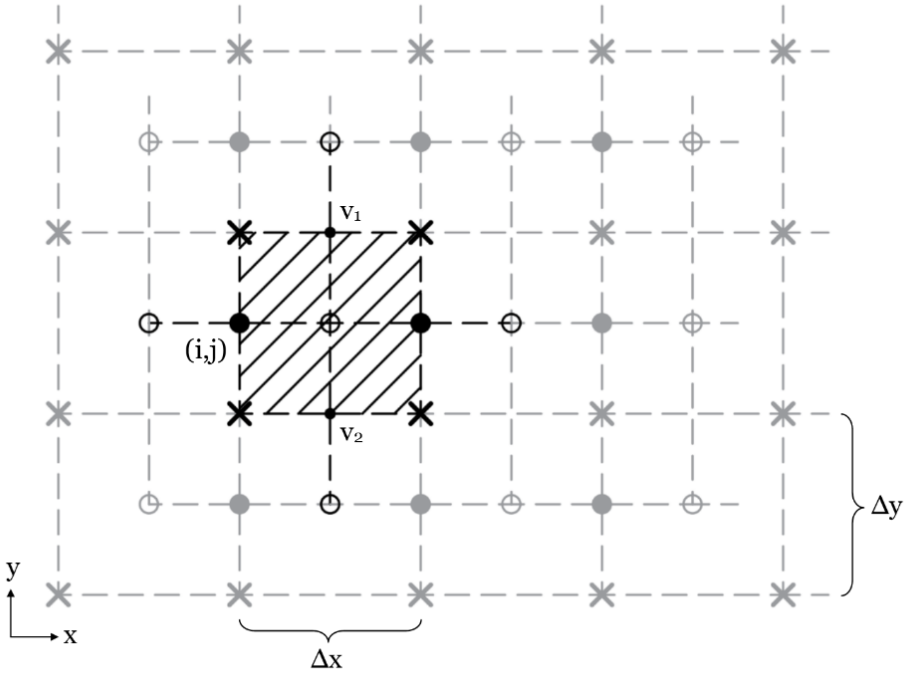

Figure 13: Computational Domain of the x-Momentum Equation.

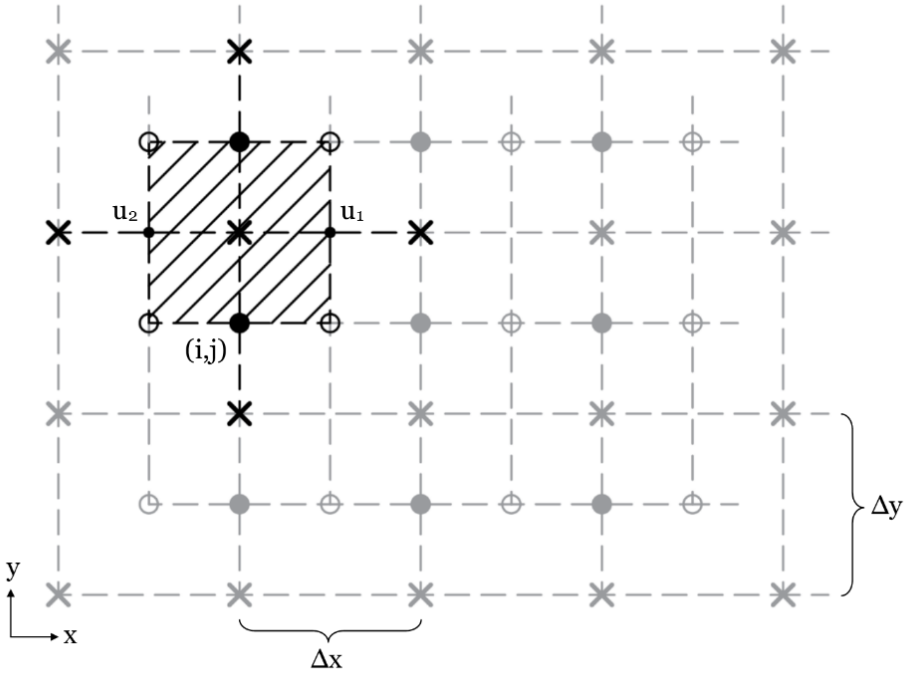

Figure 14: Computational Domain of the y-Momentum Equation.

In each figure, the unutilized grid locations have been reduced in opacity. The average velocities within these figures have been represented as small solid dots and should not be confused with values of pressure. The equations associated with the average velocities [38] are show in Equation (22) through Equation (25):

$$u_1 = \bar{u}^n_{i+1/2,j+1/2} = \frac{u^n_{i+1/2,j}+u^n_{i+1/2,j+1}}{2}, \tag{22}$$

$$u_2 = \bar{u}^n_{i-1/2,j+1/2} = \frac{u^n_{i-1/2,j}+u^n_{i-1/2,j+1}}{2}, \tag{23}$$

$$v_1 = \bar{v}_{i+1/2,j+1/2} = \frac{v^n_{i,j+1/2}+v^n_{i+1,j+1/2}}{2}, \tag{24}$$

$$v_2 = \bar{v}_{i+1/2,j-1/2} = \frac{v^n_{i,j-1/2}+v^n_{i+1,j-1/2}}{2}. \tag{25}$$

As one can see, the varying subscripts require an attention to detail and deep understanding of the staggered grid. This is apparent with the averages shown above, whose grid locations are not the same as their orthogonal counterpart. For example, the average vertical velocities shown by Equation (24) and Equation (25) use different grid points than those of the corresponding horizontal velocities in the x-momentum equation. This is illustrated in greater detail in Equations (26) and (27) [38] where each product of u and $\bar{v}$ has been expanded:

$$(u\bar{v})^n{}_{i+1/2,j+1} = u^n_{i+1/2,j+1} \cdot \bar{v}^n_{i+1/2,j+1/2}, \tag{26}$$

$$(u\bar{v})^n{}_{i+1/2,j-1} = u^n_{i+1/2,j-1} \cdot \bar{v}^n_{i+1/2,j-1/2}. \tag{27}$$

These expansions have been shown to eliminate (or reduce) any confusion that might arise when working with the discretized momentum equations and the staggered grid. The discretized momentum equations can be re-arranged to solve for the horizontal and

vertical velocities in the next time step for every point within the computational domain. This yields [38] Equation (28) and Equation (29):

$$u_{i+1/2,j}^{n+1} = u_{i+1/2,j}^{n} + \frac{A \cdot \Delta t}{\rho} - \frac{\Delta t}{\rho \cdot \Delta x}\left(P_{i+1,j} - P_{i,j}\right), \tag{28}$$

$$v_{i,j+1/2}^{n+1} = v_{i,j+1/2}^{n} + \frac{B \cdot \Delta t}{\rho} - \frac{\Delta t}{\rho \cdot \Delta y}\left(P_{i,j+1} - P_{i,j}\right). \tag{29}$$

The variables A and B represent components of the momentum equations [38], whose values are shown in Equation (30) and Equation (31):

$$A = -\rho\left(\frac{\left(u^2\right)^n{}_{i+3/2,j} - \left(u^2\right)^n{}_{i-1/2,j}}{2\Delta x} + \frac{(u\bar{v})^n{}_{i+1/2,j+1} - (u\bar{v})^n{}_{i+1/2,j-1}}{2\Delta y}\right) + \mu\left(\frac{u_{i+3/2,j}^n - 2u_{i+1/2,j}^n - u_{i-1/2,j}^n}{(\Delta x)^2} + \frac{u_{i+1/2,j+1}^n - 2u_{i+1/2,j}^n - u_{i+1/2,j-1}^n}{(\Delta y)^2}\right), \tag{30}$$

$$B = -\rho\left(\frac{(v\bar{u})^n{}_{i+1,j+1/2} - (v\bar{u})^n{}_{i-1,j+1/2}}{2\Delta x} + \frac{\left(v^2\right)^n{}_{i,j+3/2} - \left(v^2\right)^n{}_{i,j-1/2}}{2\Delta y}\right) + \mu\left(\frac{v_{i+1,j+1/2}^n - 2v_{i,j+1/2}^n - v_{i-1,j+1/2}^n}{(\Delta x)^2} + \frac{v_{i,j+3/2}^n - 2v_{i,j+1/2}^n - v_{i,j-1/2}^n}{(\Delta y)^2}\right). \tag{31}$$

Equation (28) through Equation (31) formulate the basis for the pressure corrective method. Although it will be explained in detail within the following section, the pressure correction method allows a user to yield the steady-state pressure and velocity values, given that the boundary conditions of a system are known.

4.4.1 The Pressure Correction Method

The pressure correction method is an iterative approach used to develop steady-state physical properties [38]. The initial conditions of the system are chosen arbitrarily and the discretized continuity and momentum equations are iterated with changes made to the pressure distribution. The system is said to reach steady-state once the pressure gradient allows for the continuity and momentum equations to be satisfied. Although the

initial conditions are chosen arbitrarily,[6] the boundary conditions must be maintained for the system to converge as well as to generate valid results. It is for this reason that the boundary conditions remain constant through all of the iterations.

At the start of an iterative process, the estimated pressure values are denoted as P*. These estimated values are used to solve for the horizontal velocity, u, and the vertical velocity, v, from the discretized momentum equations – Equation (28) and Equation (29). Because these values are calculated using an estimated pressure gradient, their variables are also denoted by a star. Anderson observes that since they were obtained from estimated values of P*, the values of u* and v* when substituted into the continuity equation will not necessarily satisfy that equation [39]. This results in the use of a pressure correction term. A pressure correction P' is added to the estimated pressure values P* to generate a new pressure gradient that will bring the velocity field into more agreement with the continuity equation. This yields [38] the following relationship:

$$P = P^* + P'. \tag{32}$$

The corrected pressure gradient P is then defined as the new estimated pressure gradient for the next iteration. Correction equations are also used for the velocity terms [38] and are represented as Equation (33) and Equation (34) in this text. These values are also used as the estimated values for the next iteration. It should be noted that a correction equation is not shown for velocities in the z-direction and must be added when modeling a three-dimensional fluid flow system. Thus,

$$u = u^* + u', \tag{33}$$

$$v = v^* + v'. \tag{34}$$

[6] For convenience, all of the initial conditions of a system are typically set equal to zero.

This process is repeated until a velocity or pressure field is found that satisfies the continuity equation. It is important to note that the pressure correction method is not a time-accurate method [39]. That is, the flow field at each iteration is not an accurate representation of the actual flow transients and should only be used to obtain the flow field at steady-state. If the velocity terms are written to be in respect to their correction terms (i.e., with the prime notation), it then becomes possible to generate a discretized pressure correction formula that encompasses the velocity correction [38, 39]. Equation (35) shows the final form of pressure correction formula:

$$P'_{i,j} = \frac{1}{a}(bP'_{i+1,j} + bP'_{i-1,j} + cP'_{i,j+1} + cP'_{1+j+1} + d). \tag{35}$$

The variables a, b, c, and d are defined as follows [39]:

$$a = 2\left(\frac{\Delta t}{(\Delta x)^2} + \frac{\Delta t}{(\Delta y)^2}\right), \tag{36}$$

$$b = -\frac{\Delta t}{(\Delta x)^2}, \tag{37}$$

$$c = -\frac{\Delta t}{(\Delta y)^2}, \tag{38}$$

$$d = \frac{\rho}{\Delta x}\left(u_{i+1/2,j} - u_{1-1/2,j}\right) + \frac{\rho}{\Delta y}\left(v_{i,j+1/2} - v_{i,j-1/2}\right). \tag{39}$$

4.4.2 The SIMPLE Algorithm

The SIMPLE algorithm is the term used to summarize the steps that are employed in the pressure correction method. The acronym SIMPLE stands for “semi-implicit method for pressure-linked equations” and is a widely accepted and used technique for incompressible, viscous, CFD applications [38]. In fact, the SIMPLE algorithm is one of the solution techniques made available within ANSYS Fluent software. The following list is a summary of the SIMPLE algorithm [38]:

1. Define the initial conditions of the system arbitrarily for unknown boundary conditions. Because these values of pressure and velocity are rough estimates, they are denoted by a star. For example, $(P^*)^n$, $(u^*)^n$, and $(v^*)^n$.
2. Using Equation (28) and Equation (29), solve for the velocities inside the flow field at the next time step. These points are the internal points within the staggered grid and do not include the boundary nodes. Again, because these new velocities are calculated using estimated values, they are denoted as the following: $(u^*)^{n+1}$ and $(v^*)^{n+1}$.
3. Substitute the newly calculated values of $(u^*)^{n+1}$ and $(v^*)^{n+1}$ into the pressure correction formula, Equation (35), to solve for the correction pressure terms P' for all interior points of the grid. It should be noted that for the first iteration, there are no values for P' defined. These values can be defined equal to zero for the first iteration.
4. The correction term can then be added to the guess pressure values to generate the new "guessed values" for the next iteration. This is illustrated by Equation (40). As one will notice, the pressure correction, P', is notated with a n+1 as opposed to an n. This has been done because this value is calculated using velocities from the next time step. Relaxation can be introduced to increase that rate in which a solution is found.[7] Thus,

$$(P^*)^{n+1} = (P^*)^n + (P')^{n+1}. \quad (40)$$

[7] The correction for the velocities is encompassed within the pressure correction equation and SIMPLE algorithm. This means that Equation (33) and Equation (34) are no longer valid and thus can be ignored.

5. Repeat Steps 1 through 4 until the system has converged. When convergence is achieved, a velocity distribution has been calculated that satisfies the continuity equation. Typically, the value of d – Equation (39) – is an indication of convergence. A system can be said to have converged when the difference between two consecutive velocity profiles is that of a provided tolerance (typically, 10^{-6}).

5. Model Generation, Refinement, and Simulation

5.1 Fall Quarter (2016)

5.1.1 Patient A – Data Set #1

The first set of MRI data from Dr. Elluru and Dr. Kalra was received on July 1st, 2016. The data were physically delivered to Dr. Kumpaty in the form of a compact-disc (CD). The CD contained both the MRI images for what has been labeled as "Patient A" as well the Centricity DICOM Viewer developed by GE Healthcare. Upon exploring the file directory within the disc, it appeared that the MRI images were not in a standard DICOM (or .dcm) format. However, none of the programs used for this project had any difficulty working with file directory stored on the disc. Nonetheless, the files were converted to DICOM format by exporting the images using a program called RadiAnt [40].[8] These files were then stored in a project directory backed up by Microsoft OneDrive. This allowed for redundancy in case the disc was to be damaged as well as for convenience.

Table 4 lists the series information that was provided within the first data set. Six series of MRI images were provided within the disc, all of which, except for Series 3, contained cinematics of the patient's airway as he/she breathed. The description from each series indicates that two series were taken in the patient's sagittal plane and three were taken in the axial plane. The words "FAT SAT" within the descriptions indicate the MRIs were taken using a fat saturation. Fat saturation is a technique used to selectively

[8] RadiAnt is a DICOM viewer that has an unlimited (or rather long) evaluation period. The program came highly recommended from the online community. The program would cost approximately $90 USD for commercial use.

saturate fat protons prior to acquiring data. This allows for fat molecules to produce negligible signal and can be used as a form of fat suppression within the images [41]. The last portion within the descriptions inform the viewer that the images were taken using a 12 mm plane thickness. This information can be ignored as the location between each frame remains constant.

Table 4: Summary of MRI Data Provided in the First Data Set.

Series	Description	Frames
3	MR: 3 PLANE LOC	21
7	MR: SAG 2D FIESTA FAT SAT ASSET 12mm	117
8	MR: SAG 2D FIESTA FAT SAT ASSET 12mm	128
9	MR: AX 2D FIESTA FAT SAT ASSET 12mm	6
10	MR: AX 2D FIESTA FAT SAT ASSET 12mm	128
11	MR: AX 2D FIESTA FAT SAT ASSET 12mm	128

Only four of the six series that were provided could be used in analysis. Series 3 – known as a 3-plane localization – is a set of images used in calibration (see Section 4.2.1), and is not intended to be used in medical applications beyond image acquisition. These images are generally lower resolution and have a larger FOV. Series 9 also cannot be used because it contains a small number of frames, which would make any analysis negligible. Thus, the only images that could be used in confidence were within Series 7, 8, 10, and 11.

The programs that were the primary focus during this project include, but are not limited to, Materialise Mimics, 3D Slicer (or Slicer), and Invesalius. For evaluation purposes, all three of these programs were used in analyzing the images from Patient A.

The first program to be tested was Materialize Mimics. Mimics is a propriety software that requires a commercial license. Fortunately, an evaluation license for mid-July to mid-August was obtained upon contacting a sale representative from the company. During that period, time was invested in becoming familiar with the program's interface as well as the tools used in generating models. Although there was some uncertainty prior to working with the software, it became instantly clear that the cinematics provided in Series 7, 8, 10, and 11 could not be used within this program. In fact, only the images from the 3-plane localization would properly import.

A limited amount of work could be performed using this series because of the poor quality and varying slice distance within the data set. These variations are highlighted in

Table 5, where the number of slices (i.e., images) and corresponding thickness are summarized for each orientation. In fact, because the series is composed of scans taken in different planes, it appears that the volume rendered by Mimics is dependent on which orientation it decides to choose at random. For example, the file directory containing the MRI images could be loaded into Mimics the same way multiple times; however, each time could result in a different orientation being presented upon selecting Series 3. This was particularly odd behavior that could not be explained until working within 3D Slicer and Invesalius.

3D Slicer was used once the evaluation period for Mimics had expired. Unlike Mimics, Slicer is an open source program available free for download with an unlimited user license. The learning curve associated with this program is steeper than Mimics, but the two share many similarities in terms of user interface and functionality. As one would

expect, Slicer was first developed in academia as part of a Master's thesis project involving several universities [42, 43, 44]. Since its incarnation, it has grown to a very large collaborative project involving individuals across the engineering and biomedical fields. The program is unique in that it is modular in design, allowing for any custom features (or modules) to be installed directly within the base program.

Table 5: Summary of Images within Series 3 for Patient A.

Orientation	Number of Slices	Slice Thickness [mm]
Axial	1	n/a
Coronal	12	9.65*
Sagittal	9	10

*This number represents an average slice thickness; slice thickness varied between 9.6 mm and 9.7 mm in the coronal view.

After some time was spent using Slicer, a final program evaluation was performed using Invesalius. Invesalius is another popular open source application that is used for creating three-dimensional (3D) models from medical images. The program was first developed in 2001 by Brazil as a means of bringing better imaging technology to the country [45]. Of the three programs that were used, this was the simplest to work with. Unlike Mimics and Slicer, Invesalius is clearly broken down into a linear work flow:

1. Load data.
2. Select regions of interest.
3. Configure the 3D surface.
4. Export data.

Although a user must follow these steps in order, he/she is free to move back any number of steps to make necessary changes. This workflow, along with the simple user interface, provides for the fastest generation of a three-dimensional (3D) model. The major limitation of this application is that it does not provide any advanced tools for image segmentation or for post-processing.

Of the three programs evaluated, it was determined that 3D Slicer would be the appropriate primary program in trying to develop three-dimensional (3D) models of the pediatric airway. Although Materialise Mimics is the most versatile and feature-packed of the three applications, it was decided it would not be the main program for working with the MRI images. A price quote of $2,350.00 was received for a six-month academic license of the software. This was a non-viable option, given that no budget was allocated to the project and that Mimics was not an absolute necessity. Dr. Kumpaty, a project advisor, was able to approve access to a Mimics license available through the Rapid Prototyping Center (RPC) at MSOE, but the restricted access to the RPC's facility further reduced the appeal of the program. Overall, the cost of the program and its restricted availability made it an undesirable choice. Slicer was chosen over Invesalius because it was believed to be a more capable program.

It appears that the current programs developed to analyze medical images (other than viewers) have not been designed to work with cinematics or DICOM images taken in a single plane. Instead, these programs are best in manipulating images that have been gathered using a constant slice thickness at different points in space. This uniformity is what allows for the sagittal and coronal views to be generated from the axial slices, as well as the generation of three-dimensional (3D) models. This is key as it indicated that

working with the cine MRIs was more difficult than originally thought to be during the project proposal.

Nonetheless, it was deemed that effort should still be placed in working with the first data set (i.e., Patient A), because the generation of 3D models was proposed. This meant working with the images gathered from the localization process (see Series 3 in Table 4). As mentioned earlier, difficulties arose when working with these images within Mimics. At the time of use, it appeared that Mimics had the tendency to randomly choose the orientation to work with. This behavior couldn't be explained until working with 3D Slicer. Figure 15 is a screenshot of the DICOM browser within 3D Slicer. The DICOM browser provides a hierarchal representation of the data for a patient. As one can see, the browser is broken into three sections. The top section lists the patients that have been loaded within the program. What has been assigned as Patient A for this project can be seen in the browser with the patient name "o". The middle section details all the studies that have been performed for the corresponding patient. A study refers to all the series of images taken during one sitting (thus, one would have multiple studies if images were on different days). Finally, the bottom section of the browser details all the series of images provided within the study. In this case, one can see all the series that have been previously detailed in Table 4.

The area of focus within the DICOM browser has been highlighted using dashed lines. This portion of the browser is shown to the user when he/she examines a series of data. Because of the previous issues with working with the localized data series, Series 3 was examined prior to being loaded into 3D Slicer. As one can see, the examination resulted in a series of notes. The first note refers to the data series as a whole and contains

a warning that the images are not equally spaced. This fact became clear prior to importing the MRI images and has been pointed out in Table 5. What is important is that examination then automatically separated the images based on their orientation. This can be seen with the three subsequent lines. These individual orientations can then be loaded upon selecting their corresponding checkbox and selecting load on the bottom left.

The images in the coronal and sagittal orientations could be used. Both orientations contained multiple images, whereas the axial orientation only contained one. Figure 16 and Figure 17 are screenshots of the coronal and sagittal data when imported into 3D Slicer, respectively. Each figure is divided into four quadrants, which represent different orientations. These quadrants have also been color categorized using a slim banner located on the top of each view. Red is reserved for the axial orientation, yellow is reserved for the sagittal, and green is reserved for the coronal. The top-right quadrant represents the three-dimensional (3D) view and is categorized using a blue banner.[9]

[9] Colors are reserved for specific orientations but a user is free to change the orientation as he or she pleases. Furthermore, the layout of the windows/views can be changed depending on what orientation or location a user may want to focus on.

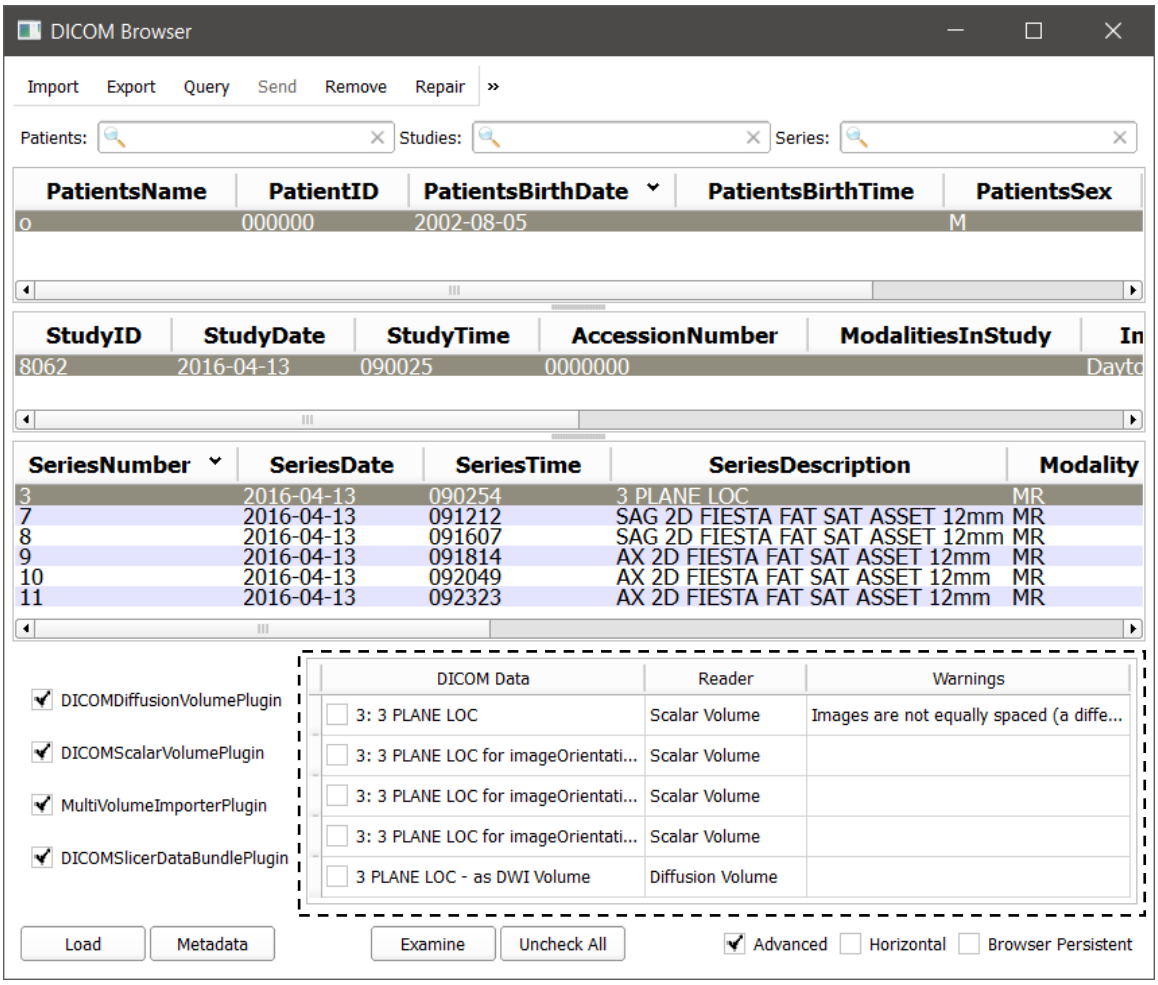

Figure 15: DICOM Browser within 3D Slicer with Series 3 Selected.

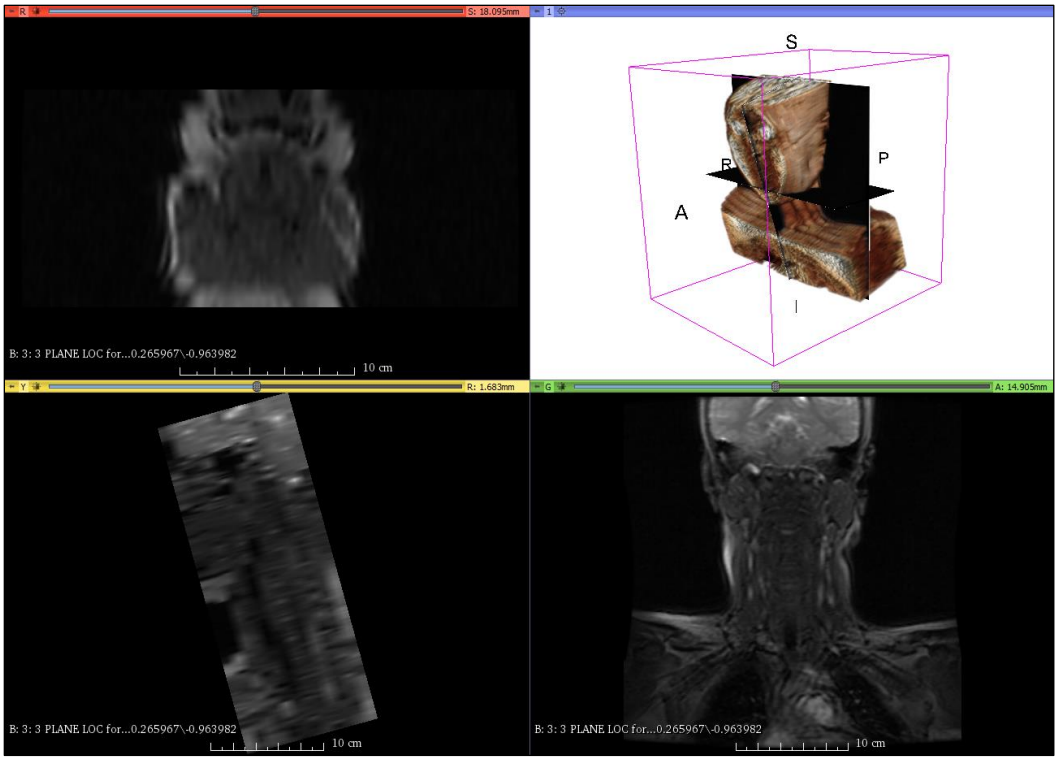

Figure 16: Coronal Orientation from Patient A, Series 3.

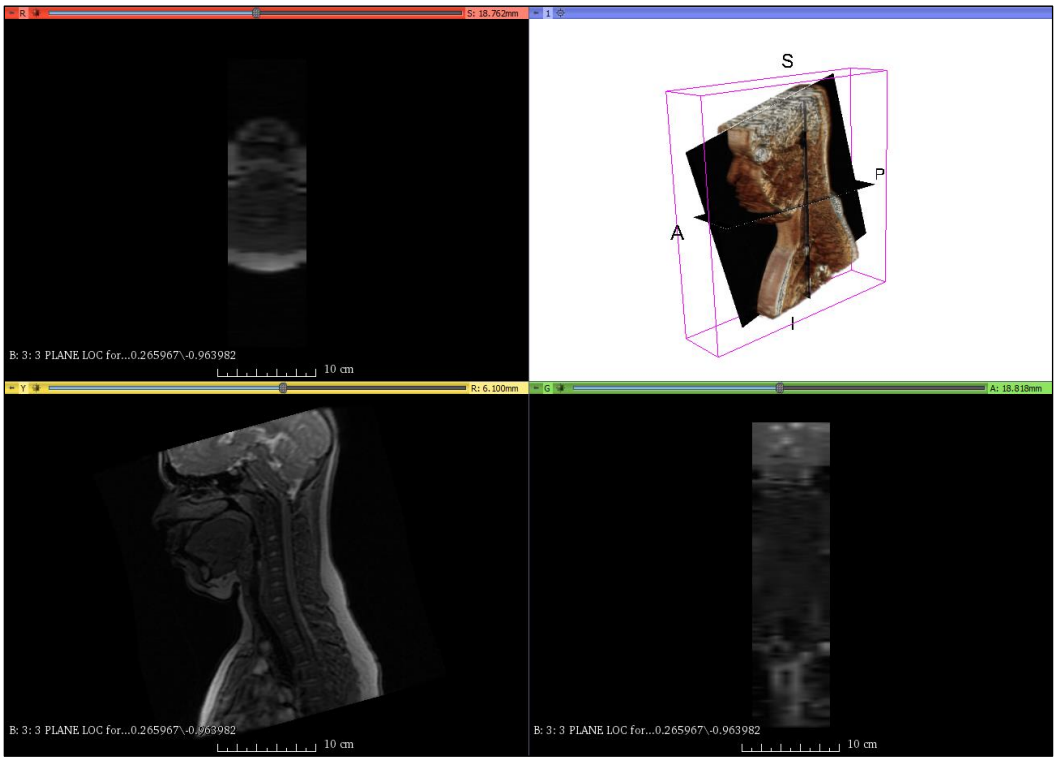

Figure 17: Sagittal Orientation from Patient A, Series 3.

A volume render is included in both Figure 16 and Figure 17 to illustrate the three-dimensional (3D) data that could be extracted from the MRI images. The tissue highlighted in the renderings is a preset for MRI images. It is important to note that the volume render feature is a quick way to visualize the internal anatomy of the scan but does not allow a user to develop surface models within that module. The reason for this is because the volume rendering module is a particle-rendering engine and does not directly correlate to solids and surfaces. 3D models must be generated using the editor module, which is analogous to creating masks in both Mimics and Invesalius.

In an attempt to save time, it was first believed that it would not be necessary to isolate the tissue of the airways. Because the airways encompass empty space, it was believed that all the tissue within the images could be selected and that an inverse of the generated model would result in the fluid domain. Figure 18 illustrates the first attempt at extracting the airway model for Patient A. The generated surface model is a silhouette of the patient with cavities existing internally. As one can see, the model was developed using a surface mesh, which had to be exported into the stereolithography (STL) file format. The inverse of the model was created by taking the difference between it and a larger 3D element (in this case, a cube). This process was performed within Blender, an open source 3D creation suite. Blender had to be used because it was better suited with working with 3D meshes. Computer-aided-design (CAD) programs such as SolidWorks and Autodesk Inventor work poorly with these file types.

Figure 18: Surface Mesh Generated from the Coronal View of Series 3 for Patient A.

Figure 19 shows the airway that was extracted from the silhouette of Patient A. The largest issue with this model is that it is discontinuous. This model could not be used in CFD simulation without additional manipulation. Paths would have to be extruded to achieve a continuous fluid domain and this would require a number of assumptions about the airway geometry, defeating the purpose of the study. The discontinuity and sharp features within this model are due to the slice thickness and resolution of the images used. The slice thickness of Series 3 is approximately ten times larger than what is typical in MRI 3D acquisition (10 mm versus 1 mm). Thus, one is not capable of capturing the smooth and complex shape of the airway. The poor resolution of the images also inhibits the ability of creating a finite boundary between the human tissue and empty space.

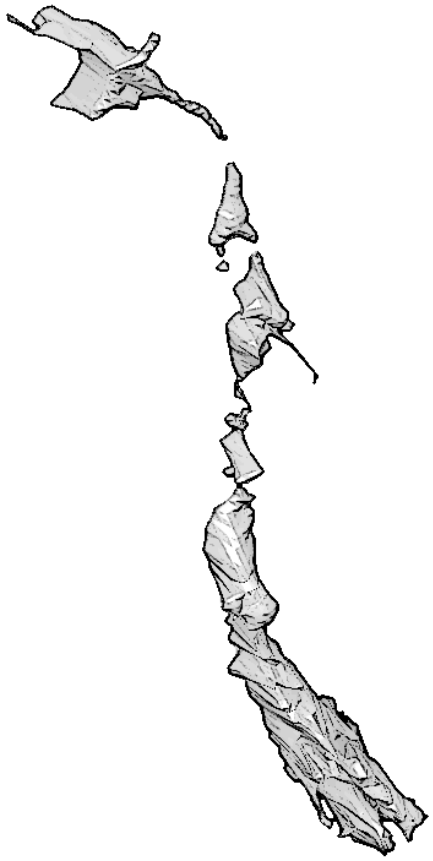

Figure 19: Extracted Airway from Surface Mesh of Patient A.

The subtraction method for generating an airway model also proved to be as equally time consuming as producing a tissue mask. Although another model was not generated using this technique, a portion of the steps involved were performed to gather insight into the MRI images.[10] The first step in generating a tissue mask involves a thresholding technique in which the tissue density is selected based on the color intensity. This is the simplest method of image segmentation and it is also one of the fastest [46]. Table 6 shows the preliminary threshold region for the airway tissue. This region was

[10] The low resolution and large slice thickness of the images would result in another poor-quality airway; thus, another model was not deemed necessary.

determined by the author's best judgement and is highlighted in Figure 20 by the dark regions. It is important to note that this image has been altered for publishing purposes. The MRI image would typically have a black background with the internal tissue being various shades of white. Furthermore, the opacity of the image has been reduced to better highlight the tissue that has been selected. Unlike CT images, the brightness of a tissue is not proportional to physical density but rather to proton richness and the characteristics of the applied magnetic field [24]. Thus, the color of tissue is dependent on the MRI protocol used. The properties of MRI images are explained in detail within Section 4.2.2. These facts contribute to the difficulty in developing a universal process for working with MRIs to extract airway geometry.

Additional MRI images were requested from Dr. Elluru and Dr. Kalra on September 18, 2016. While the first data were sufficient in providing cinematics, the images could not be used in the generation of a 3D model. The next set of data to be sent over was requested to be a 3D acquisition with a fine slice thickness and resolution. As advised by Dr. Elluru on October 18, 2016, it was decided that the project would focus on the two types of data. Specifically, methods would have to be developed to analyze the air flow using the two-dimensional (2D) cinematics (i.e., cine MRIs), as well as a universal protocol for generating three-dimensional (3D) airway models using traditional MRI techniques.

Table 6: Preliminary Threshold Region for Airway Tissue.

Lower Limit	Upper Limit
37.50	51.50

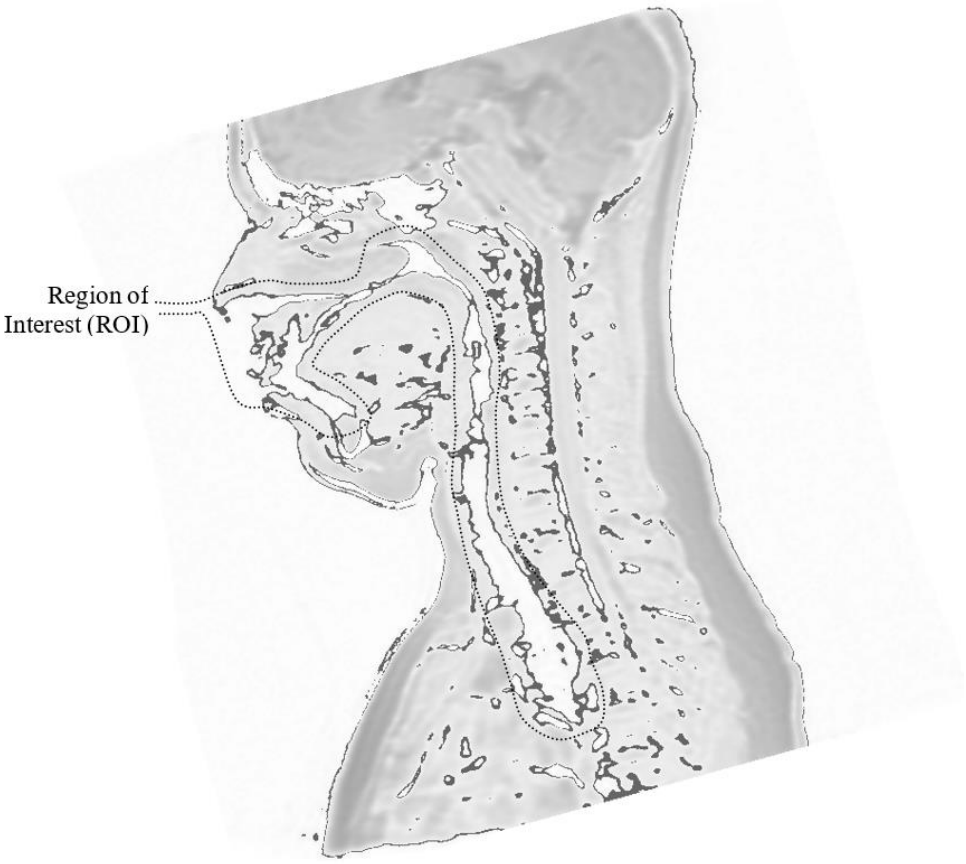

Figure 20: Tissue Highlighted in Patient A for a Threshold of 37.50 –51.50.

5.1.2 Patient B – Sample CT Data

A sample set of data was used while waiting for additional MRI images from Dr. Elluru and Dr. Kalra. It was believed that a preliminary CFD model could be created using sample data and that actual data could later be linked within ANSYS Fluent, the CFD program for this project. The time invested with sample data would also provide insight into preparing models for simulation. The best set of sample data that could be obtained was a CT scan of a patient's chest. The CT images were made available through a library provided within 3D Slicer and have been labeled as Patient B. MRI images would have been preferable; however, none were available for the chest or head. Figure 21 is a volume render of the respiratory tissue within Patient B.

Figure 21: Volume Render of Patient B Configured for Respiratory Tissue.

The respiratory tissue of Patient B was isolated using a preset within 3D Slicer. The benefit of CT scans over MRI is that they operate on the Hounsfield scale, which can be correlated to tissue density (see Section 4.2.3). The preset threshold region was then used to develop a mask for the respiratory tissue. The initial mask provided an outline of the airway and included small artifacts that had to be removed manually using traditional editing tools (e.g., erasing, drawing). Once the artifacts were removed, the airway boundary was filled to generate the fluid domain. Figure 22 illustrates the final tissue mask that was developed for the region of interest (ROI). The green regions within this figure represent captured volumes from the mask; the resulting surface model can be seen in the top-right quadrant, along with the tissue projections on each plane.

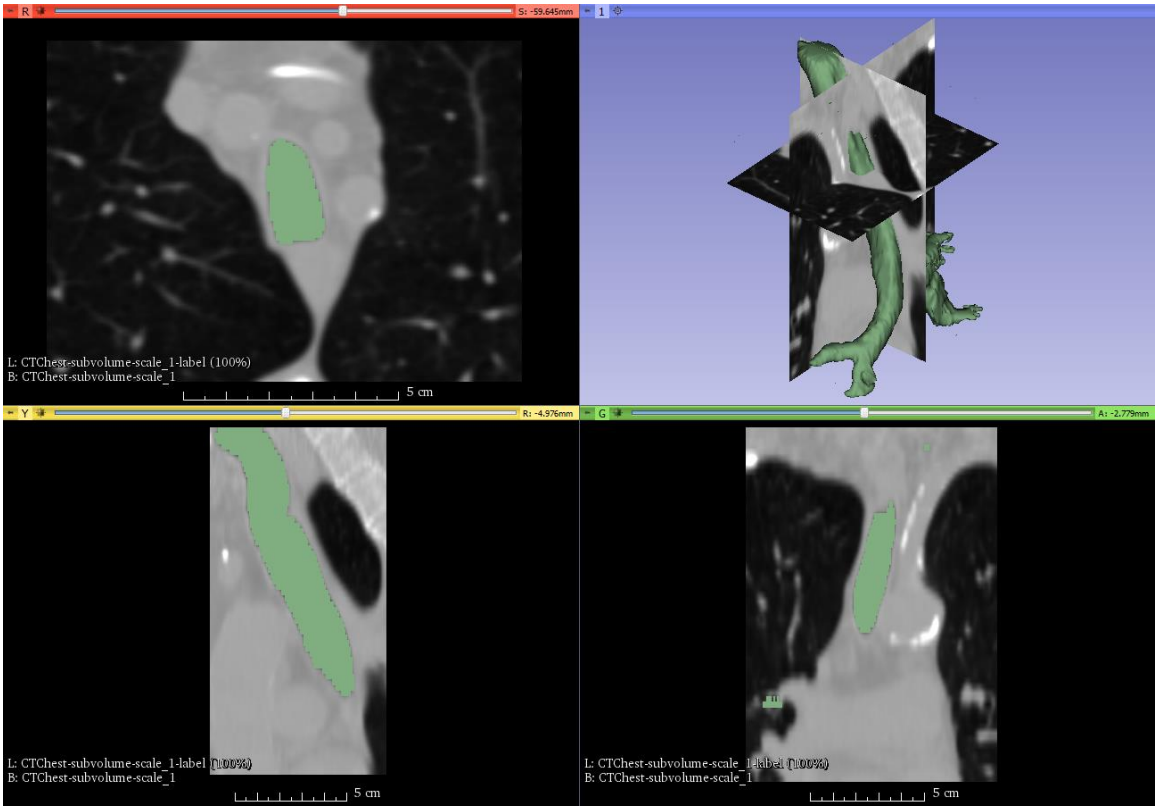

Figure 22: Applied Tissue Mask and Corresponding Surface Model for Patient B.

The surface model of the airway was then exported to an STL file to be cleaned and optimized. Figure 23 illustrates the mesh that was exported from 3D Slicer. The model contains many particles that were missed during the tissue mask process, as well some unwanted features. Model refinement can be performed within 3D Slicer; however, it was believed that a dedicated meshing program would be better suited. A period of a week had to be invested in becoming familiar with mesh models, because they function much differently than traditional models created using CAD. During this period, several programs were investigated for use. It appears that one of the best programs is Geomagic Design X by 3D Systems (the company that pioneered the STL file format and 3D printing technology) [47, 48]. This program is designed to reverse engineer mesh models and to convert them into traditional, feature-based CAD models [48]. Because of a few

constraints, budget being the largest, it was decided not to pursue this program as an option.

Instead, a combination of free and open source programs was used for mesh refinement. These programs included Meshmixer, Remake, Fusion 360, and Blender. Meshmixer is a free program available through Autodesk that allows a user to make edits to triangular meshes [49]. This program was used to smooth the model, create flat inlet and outlets via cuts, and to remove unwanted particles. These changes are shown in Figure 24. It should be noted that the models shown in Figure 23 and Figure 24 are composed of triangular meshes that are designed to capture the shape of the object. These triangular surfaces vary in shape and include very sharp corners that are undesirable in computer-aided engineering (CAE) programs, such as ANSYS. CAE programs rely on solid CAD models to generate meshes independently. Solid models are controlled by parametric equations, allowing for smooth features that are not rasterized. Thus, further changes had to be made to the refined model to prepare it for simulation. It was discovered that if the triangular-based STL was converted to a quadrilateral mesh, it could then be imported into Fusion 360 to be made into an equation-controlled model [50].

There was some difficulty in moving from a triangular to quadrilateral mesh. Two programs, Autodesk Remake and Blender, were used during this stage of the model refinement. Autodesk Remake is another program that has been developed to work with mesh objects and to convert them into “high-definition models” [51]. This program was recommended by the Autodesk community because STL models can be directly exported into a quadrilateral mesh that is optimized for their suite set via the OBJ file format

(another 3D file type). The issue with this program is that there isn't any control over the new mesh, other than selecting low, medium, and high quality. Furthermore, a user cannot specify the desired mesh density nor can he or she make any manual alterations once the model has been converted. The proprietary nature of the program could also lead to user issues, which further suggested the need to use an open source product, such as Blender.[11]

Blender has been found to be a difficult but incredible tool for working with mesh models. Some time was required to become familiar with it, because its user interface differs significantly from traditional modeling programs. All of the features available with Meshmixer are available within Blender, but both programs were still used interchangeably. It was found that some actions could be performed easier and faster within Meshmixer. A feature in Blender that is not available in Meshmixer is the "Tris to Quad" command. This function does as it describes, in that it converts a triangular model into a quadrilateral model by deleting common edges of triangles. The result of this function was not perfect, due to the complex shape of the airway. A remesh modifier had to be added to increase uniformity of the mesh grid. A balancing act had to be made during this process. A fine mesh grid would ensure that the shape of the airway is maintained but would also contribute to difficulties in converting it into a traditional solid model. Thus, a medium mesh density was chosen. This allowed for the airway geometry to be maintained without adverse effects in computation time.

---

[11] There is some confusion regarding the licensing options available for Autodesk Remake. A user is directed to downloading a trail version of the program; however, the licensing chart details a free and professional version. Nonetheless, it was deemed that Blender was a more capable program.

The next step in the conversion process involved converting the quadrilateral mesh into a spline surface model. Spline models contain equation-based curves that can be modified using traditional CAD packages. For this project, a t-spline model was created using Fusion 360.[12] Fusion 360 is parametric modeling program that is like Autodesk Inventor; however, it is free to students, individuals, and institutions that make less than $100,000 USD in revenue per year [52]. Even though steps were taken to refine the model in Blender and Meshmixer, the finally OBJ file type conversion had to be made in Autodesk Remake. Models imported directly from Blender would not convert into a t-spline model and would present several errors or issues that had to be resolved priorly. Remake appears to be specifically designed to create quadrilateral OBJ meshes that work with Fusion 360. Figure 25 illustrates the t-spline model that was interpolated from the quadrilateral mesh. As one can see, the t-spline model was composed of a uniform grid that could capture the airway geometry using significantly fewer vertices than the mesh models. The final solid (or "water-tight") model of the airway was generated upon exiting the t-spline editor in Fusion 360. This model is shown in Figure 26. The solid airway was composed of complex, stitched surfaces that were governed by splines.

[12] t-splines are a surface modeling technique unique to Autodesk products. These splines are similar to non-uniform rational basis splines (NURBS) that are common in many other programs [56, 57].

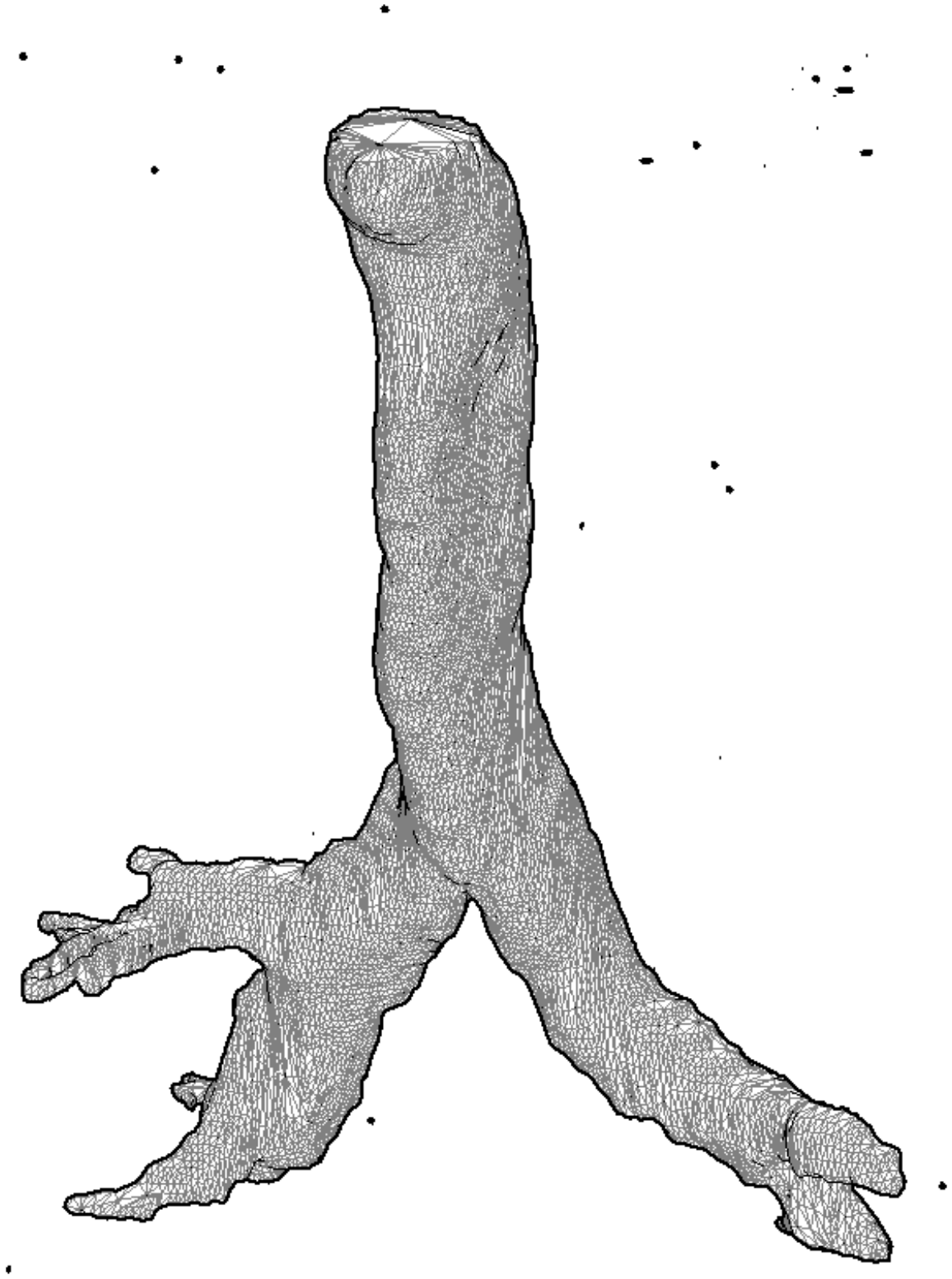

Figure 23: Airway Model of Patient B Exported from 3D Slicer.

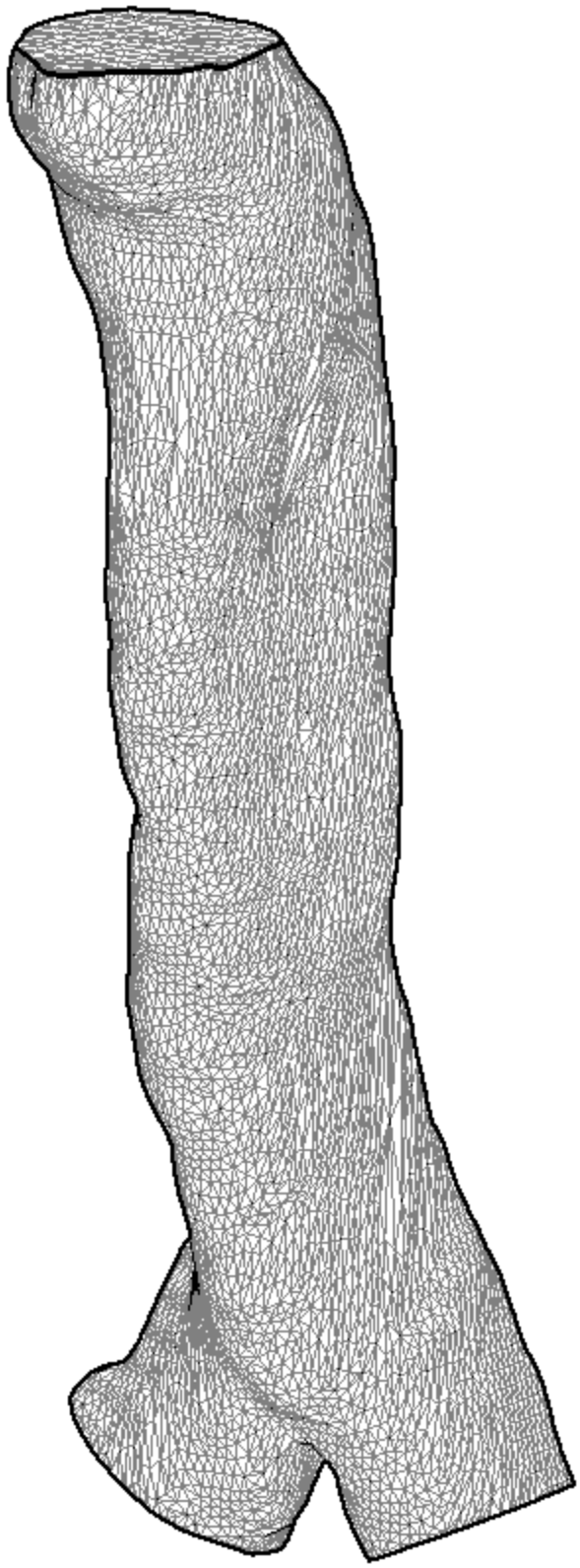

Figure 24: Refined Airway Model using Autodesk Meshmixer.

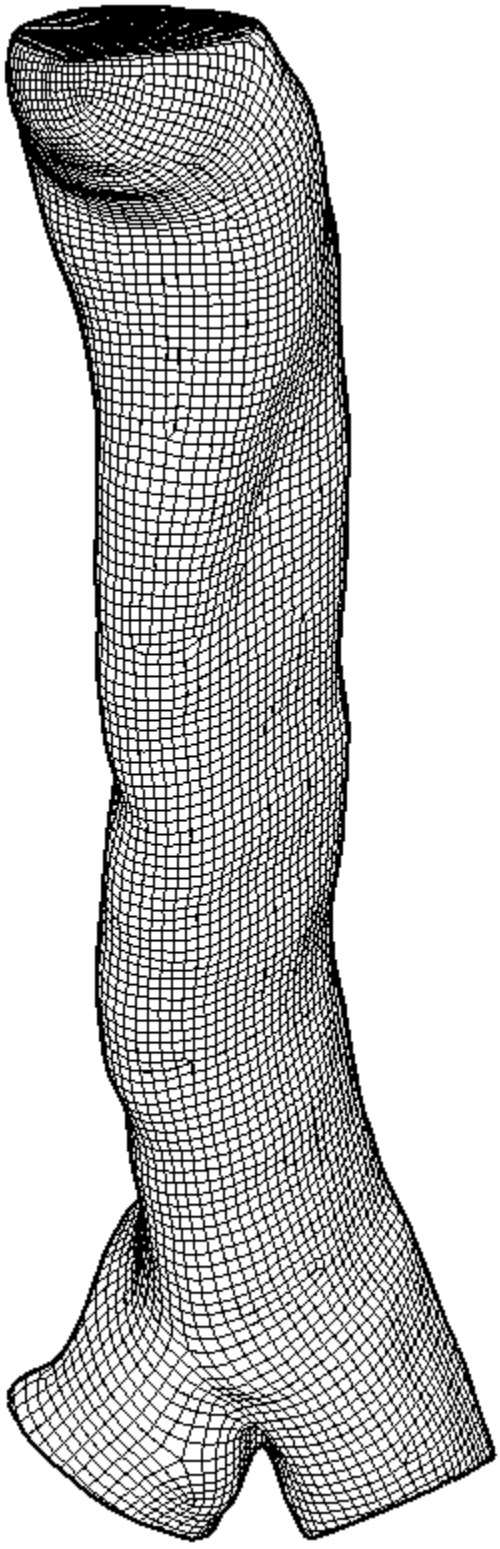

Figure 25: Refined Airway Model Converted to t-Spline (or NURB) Model.

Figure 26: 3D Airway Converted to a Water Tight Model.

Laminar and turbulent CFD simulations were conducted after the solid model was obtained. The boundary conditions used in both simulations were the same as those listed in Table 1. The velocity boundary condition of 2.3 m/s represents the peak velocity amplitude during respiration. The simulation results thus represent peak conditions at a specific point in time. The top of the airway was labeled as the inlet of the system, while bronchi were specified as the outlets. Because of time constraints, only an inhale was analyzed for each simulation type.

Special meshing considerations were taken at the walls to capture the boundary layer development within the simulations. Figure 27 illustrates the inflation mesh sizing that was implemented within ANSYS. This technique is analogous to the zonal meshing technique mentioned in Section 4.3.2. In addition to this sizing, metrics had to be reviewed to ensure the generated mesh was appropriate for simulation. ANSYS recommends that the skewness and orthogonal quality of a mesh be observed prior to importing the model into Fluent [53]. Table 7 features the mesh metric spectrum provided by ANSYS, while Table 8 contains the observed metrics for a fine mesh of the airway. As one will notice, the metrics of the airway satisfy the constraints provided. The average skewness and orthogonal quality fit within their respective “very good” ranges. Furthermore, the standard deviation of each metric indicated that most of the cells had a value close to the average. A small number of the cells did contain poor metric values, but this typically isn’t a concern if a fine mesh size is utilized. Nonetheless, a mesh independence study was performed to ensure that the results for the fine mesh were consistent with other mesh densities. This process is recommended, as it can reinsure

convergence and verify that the final values obtained are accurate. Hand calculations were also performed to ensure the validity of the CFD results.

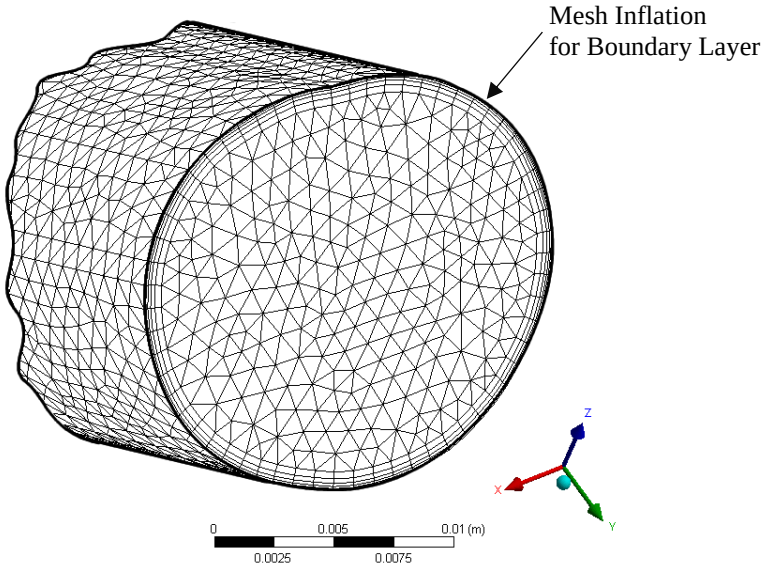

Figure 27: Mesh Inflation Specified at the Walls of the Airway.

Table 7: ANSYS Mesh Metric Spectrum.

Mesh Metric	Rating					
	Unacceptable	Bad	Acceptable	Good	Very Good	Excellent
Orthogonal Quality	0-0.001	0.001-0.14	0.15-0.20	0.20-0.69	0.70-0.95	0.95-1.00
Skewness	1.00-0.98	0.97-0.94	0.94-0.80	0.80-0.50	0.50-0.20	0.25-0

Table 8: Mesh Metrics for Fine Airway Mesh.

Mesh Metric	Min	Max	Average	Standard Deviation
Skewness	$2.9207 \cdot 10^{-4}$	0.94192	0.23198	0.1167
Orthogonal Quality	0.19546	0.99926	0.87826	$8.793 \cdot 10^{-2}$

Table 9 and Table 10 are the mesh independence and convergence studies that were performed for the laminar and turbulent simulations. In both studies, three different mesh densities were analyzed: a coarse, medium, and fine mesh. These meshes were specified by controlling the maximum and minimum cell size within the airway model. It should be noted that maximum mesh density was constrained by the element limit within the academic version of ANSYS. Furthermore, the three mesh models remained consistent between the laminar and turbulent simulations.

Table 9: Mesh Independence and Convergence Study (Laminar Flow).

Mesh Density	Nodes	Elements	Iterations	Maximum Pressure [Pa]	Maximum Velocity [m/s]
Course	40,439	96,058	450	6.571	3.875
Medium	101,773	265,846	500	7.236	3.880
Fine	155,862	504,683	500	7.734	3.928

Table 10: Mesh Independence and Convergence Study (Turbulent Flow).

Mesh Density	Nodes	Elements	Iterations	Maximum Pressure [Pa]	Maximum Velocity [m/s]
Course	40,439	96,058	400	7.618	3.914
Medium	101,773	265,846	650	8.797	3.962
Fine	155,862	504,683	1100	9.524	4.052

In each table, the iterations column represents an approximate number of iterations that were required for the simulation to converge. For both flow types, convergence was defined as when the residuals (or absolute error) reached a magnitude less than 10^{-6}, or when the residuals leveled off to an approximate steady-state value. Because the flow within the airway is turbulent, the laminar simulations never satisfied the desired residual magnitude. Instead, each laminar simulation would level off at a magnitude of approximately 10^{-5}. This result was deemed acceptable, as a laminar model was forced onto the airway. A laminar study was desirable, as it would provide a comparison to the turbulent results obtained latter. The turbulent simulations did satisfy both convergence criteria.

The pressures and velocities recorded in Table 9 and Table 10 represent the maximum pressure simulated at walls and the maximum velocity simulated at the outlets of the airway model (i.e., the bronchi). As one can see, there is variation among the values recorded for each mesh. In both the laminar and turbulent studies, the maximum pressure recorded was influenced by the mesh size. There are two theories as to why this result occurred. First, the maximum pressure occurs at the bifurcation of the airway (see Figure 29). It can be possible that the lower density meshes fail to capture the pressure being applied. The second theory is that sharp edges created from the airway may also represent unrealistic pressure readings in the first place. The sharp edges created from the bifurcation are based on the geometry that could be best extracted from the sample CT scan. It is possible that the actual geometry is smoother than what was generated. A smoother transition to the bronchi would contribute to lower pressure at the walls. Because neither of these theories could be verified or disproven, the simulation results

had to be taken with caution. Nonetheless, the results obtained using the fine mesh were assumed to be the most accurate, as it contained a higher number of cells and nodes.[13]

The smaller degree of variation was observed between the velocities recorded. Both the laminar and turbulent simulations indicated that the maximum velocity was approximately 3.9 m/s. Although variation was seen in both Table 9 and Table 10, it was concluded that the simulation was not sensitive to the mesh geometry. The maximum pressure observed in each mesh model did change; however, the overall pressure distribution remained the same. This state of affairs meant that the results can be considered accurate, but need to be confirmed with hand calculations. The study performed in both tables also provided insight into the convergence of each model type.

Approximately the same number of iterations was required for each mesh to converge in the laminar study; however, the computation time required for each iteration did increase at higher mesh densities. The exact time increase between the mesh densities was not measured. The convergence of the turbulent model was greatly influenced by the mesh of the airway. The number of iterations required for convergence was proportional to the number of nodes and cells within the mesh model. Like the laminar study, the computation time required for each iteration also increased at higher mesh densities. The error of each simulation was inversely proportional to the mesh size. This meant that even though computation time could be decreased by reducing the mesh density, it would not be desirable as the amount of error would increase by doing so.

---

[13] The fine mesh is assumed to be the most accurate, as more cells are capable of capturing the pressure and velocity fluctuations within the model. The simulation results have to be confirmed with hand calculations to ensure that the model is set up properly and that the results are reasonable.

Figure 28 is the residual plot associated with the turbulent simulation for the fine airway mesh. This plot has been included to illustrate that the proper number of iterations was performed prior to publishing the results. As one can see, approximately 1,100 iterations were necessary to reach a converged solution. After this point, all residuals expect for continuity reached a magnitude of 10^{-6}. The error within the continuity equation converged to a magnitude of 10^{-3}. This result was deemed acceptable, as no large fluctuations were observed in the residual plot after convergence was said to occur.

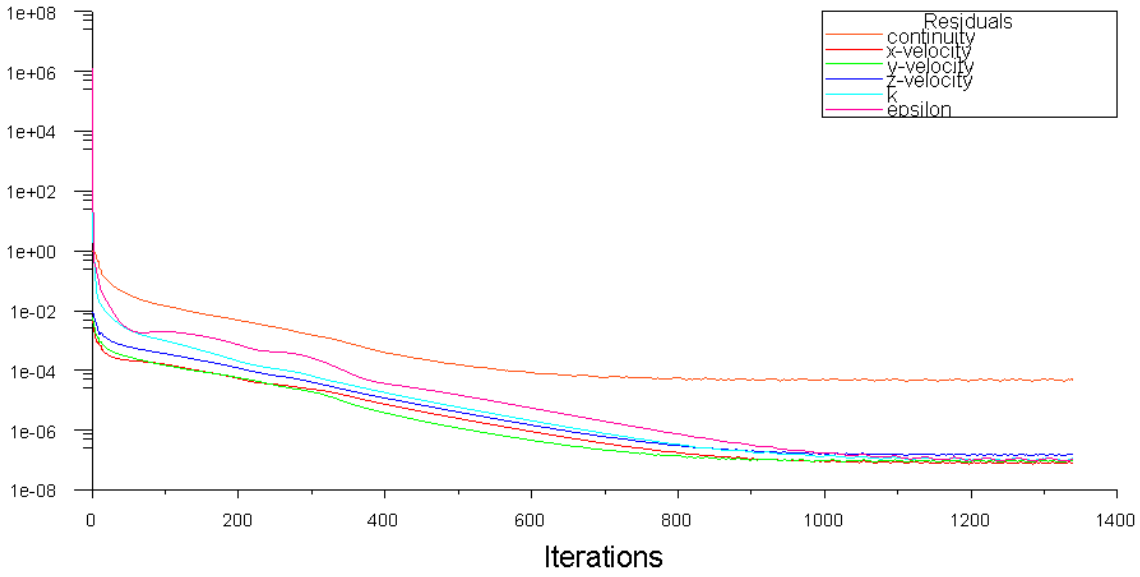

Figure 28: Residual Plot for Fine Mesh, Turbulent Simulation.

Once a converged solution was obtained, both the pressure and velocity distribution within the airway was observed. The pressure values simulated on the walls of the airway can be seen in Figure 29. The contour surface plot details that much of airway experiences low pressure values. Large pressure occurs at the top of the airway where the velocity boundary condition was applied. As mentioned earlier, the largest pressure is experienced near bifurcation of the airway. This pressure occupies a small area and is difficult to see within the figure.

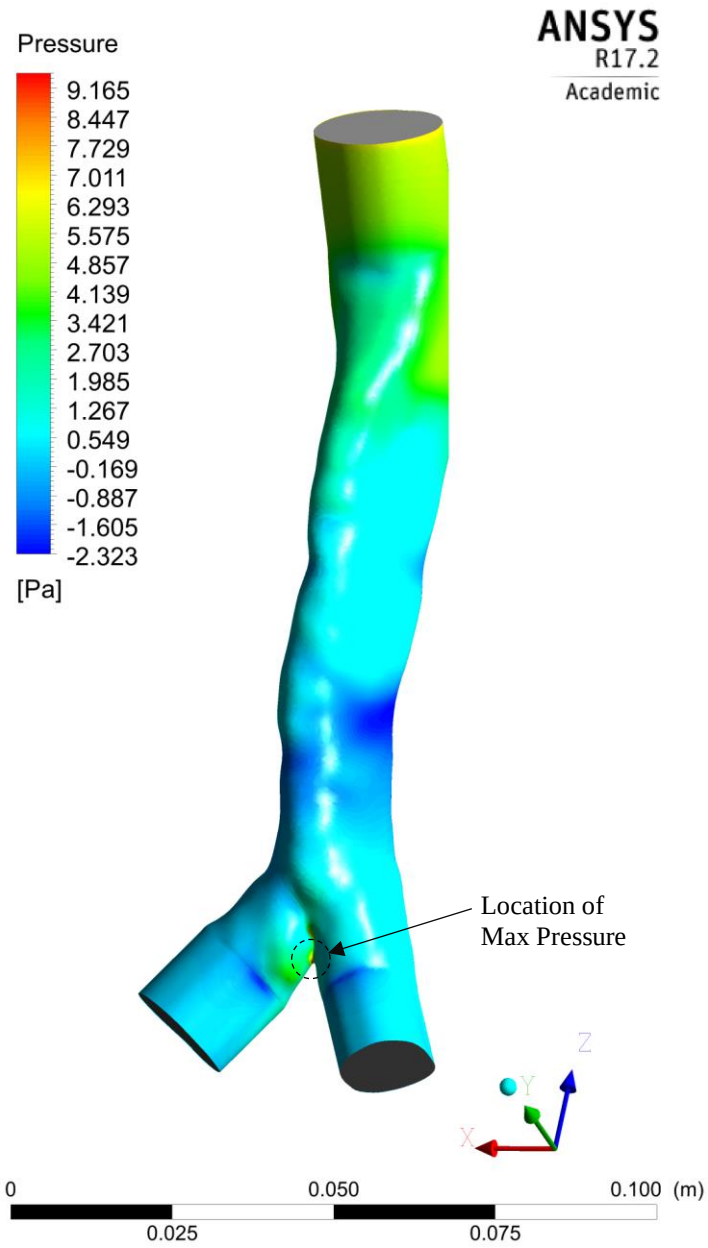

Figure 29: Pressure Contour Plot at Airway Walls.

A volume render, contour, and vector plot were used to visualize the velocity of air within the airway. Figure 30 is the volume render of the airway and is used to illustrate the air velocity within the entire 3D domain. The importance of this figure is that the volume render highlights that large velocity magnitudes exist toward the center of the airway and continue out non-uniformly at the outlets.

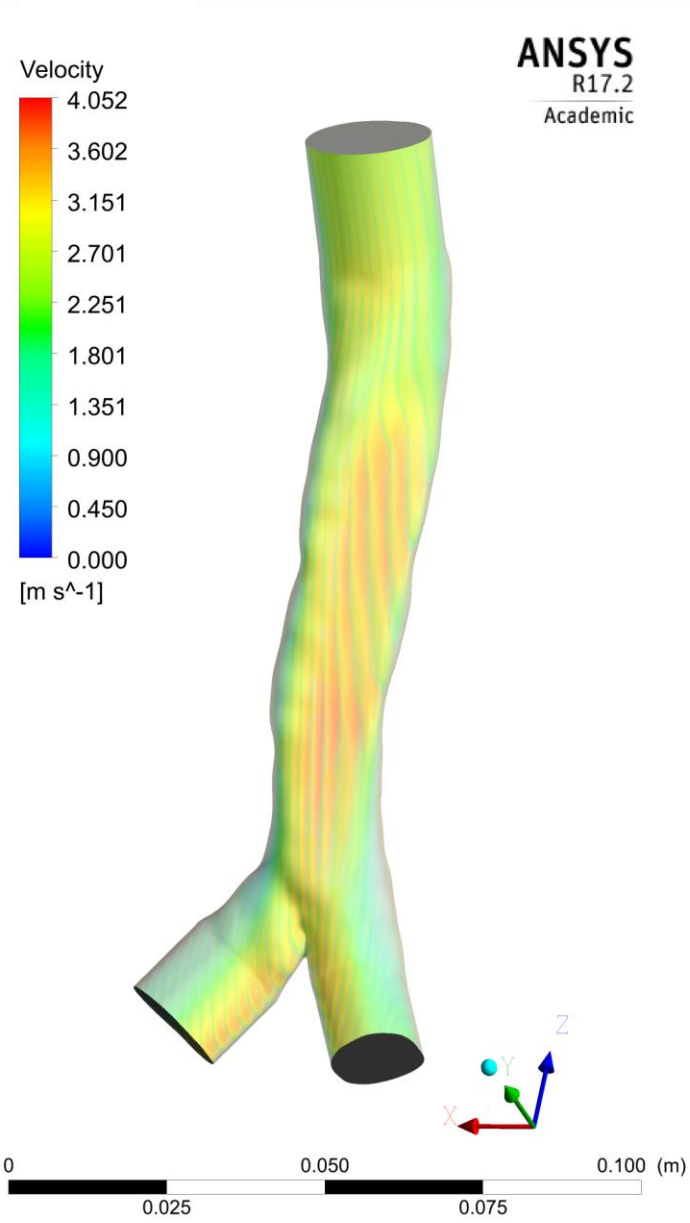

Figure 30: Volume Render of Velocity within the Airway.

A contour plot was then used to better visualize the velocity distribution along a section plane within the airway. The non-uniform shape of the airway meant that a section could not be created perfectly in the middle of the trachea. Instead, a best approximate was used that divided the trachea as evenly as possible. This meant that portion of the bottom right bronchi had to be included within the section plane. Figure 31

illustrates the velocity contour plot created on this plane. This figure clearly shows the velocity increase toward the center of the airway. A vector plot was then created along this same plane to observe the direction of the airflow and to see if any eddies exist. This plot is shown in Figure 32.

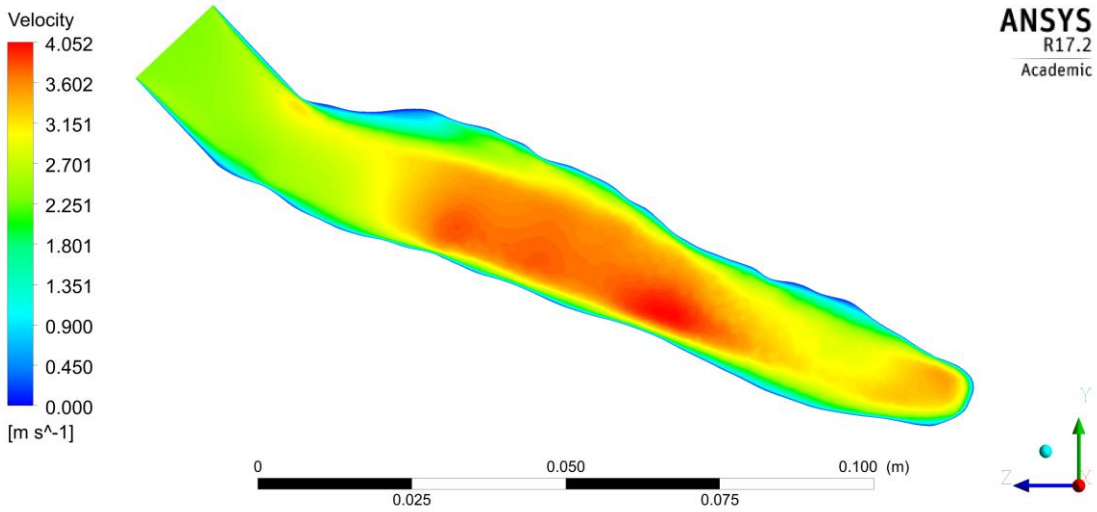

Figure 31: 2D Velocity Contour Plot at Section Plane.

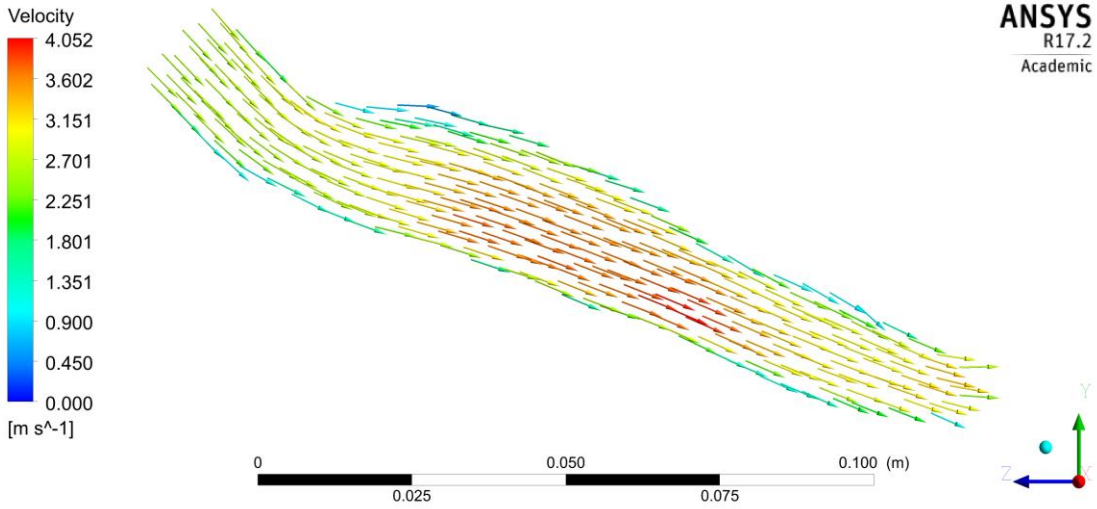

Figure 32: 2D Vector Plot at Section Plane.

A conservation of mass calculation was performed to confirm that the simulation results were accurate. For steady-state, the mass entering a system is equal to the mass exiting. This is represented by Equation (41),

$$\dot{m}_i = \dot{m}_o, \tag{41}$$

where $\dot{m}_i$ is the mass flow rate at the inlet and $\dot{m}_o$ is the mass flow rate at the outlet. Both quantities are in units of kg/s. The mass flow rate is equated using the density of the fluid, the cross-sectional area of the inlet (or outlet), and the velocity of the fluid. This relationship is shown in Equation (42),

$$\dot{m} = \rho \cdot A \cdot v, \tag{42}$$

where ρ is the density of air in kg/m^3, A is the cross-sectional area in m^2, and v is the velocity of the air in m/s. Substitution of this equation into Equation (41) yields the following:

$$\rho_i \cdot A_i \cdot v_i = \rho_{o_1} \cdot A_{o_1} \cdot v_{o_1} + \rho_{o_2} \cdot A_{o_2} \cdot v_{o_2}. \tag{43}$$

The subscripts in Equation (43) indicate the location of each variable. Specifically, the subscript *i* indicates the inlet, whereas the subscript o_1 and o_2 indicate the two outlets of the airway. Because the air is traveling much slower than the speed of the sound, the fluid flow can be assumed to be incompressible. Thus, the density at the inlet is equal to the density at the two outlets. In this case, the density term drops out of Equation (43). The velocities measured at the inlet and outlets are also better represented as averages over their respective cross-sectional areas. This simplification yields to Equation (44):

$$\bar{v}_i \cdot A_i = \bar{v}_o \cdot (A_{o_1} + A_{o_2}). \tag{44}$$

In this equation, an average velocity is used for both the inlet and outlet of the system. As one can see, the average outlet velocity is defined as the total average across both outlets.

All the values in this equation are known, except for the average outlet velocity. Thus, Equation (44) can be manipulated to solve for this value. This manipulation is

$$\bar{v}_o = \bar{v}_i \cdot \frac{A_i}{A_{o_1}+A_{o_2}}. \tag{45}$$

The average inlet velocity is equal to 2.3 m/s and is the same as the velocity boundary condition specified in Table 1. The cross-sectional area of each inlet and outlet is listed in Table 11. These values were measured from the airway geometry within Autodesk Fusion 360.

Table 11: Cross-Sectional Area of Airway Geometry.

Location	Cross-sectional Area [mm^2]
Inlet (A_i)	286.292
Outlet #1 (A_{o1})	171.616
Outlet #2 (A_{o2})	158.842

These values were then used to calculate the average outlet velocity from the airway. Table 12 lists the value that was calculated from Equation (45) versus the average outlet velocity simulated within ANSYS Fluent. As one can see, a 1.2% percent difference exists between the calculated and simulated values. This is a good indication that the CFD simulation is correct and that the values shown in Figure 29 through Figure 32 can be taken with confidence. Unfortunately, Bernoulli's principle could not be applied to calculate the pressure at the top of the airway. Bernoulli's principle allows for the pressure and velocity at two points along a stream line to be calculated. The split in the airway does not allow for the principle to be applied unless assumptions are made about the velocity distribution between the two outlets. It would have been ideal to

compare the simulated average pressure at the top of the airway to one calculated physically.

Table 12: Simulation Results versus Hand Calculation.

Average Outlet Velocity (v_o) [m/s]		Percent Difference [%]
Hand Calculation	From Simulation	
1.9926	2.0165	1.1923

Figure 33 is a process flow diagram that summarizes all the steps that were taken to transform the DICOM images into a fluid simulation. Each block in this diagram represents a different stage in the conversion process, whereas the connecting arrows indicate the input and output file type at each stage. The changes in each stage are further visualized with an image shown above each block, highlighting the changes that were made to the 3D airway model.

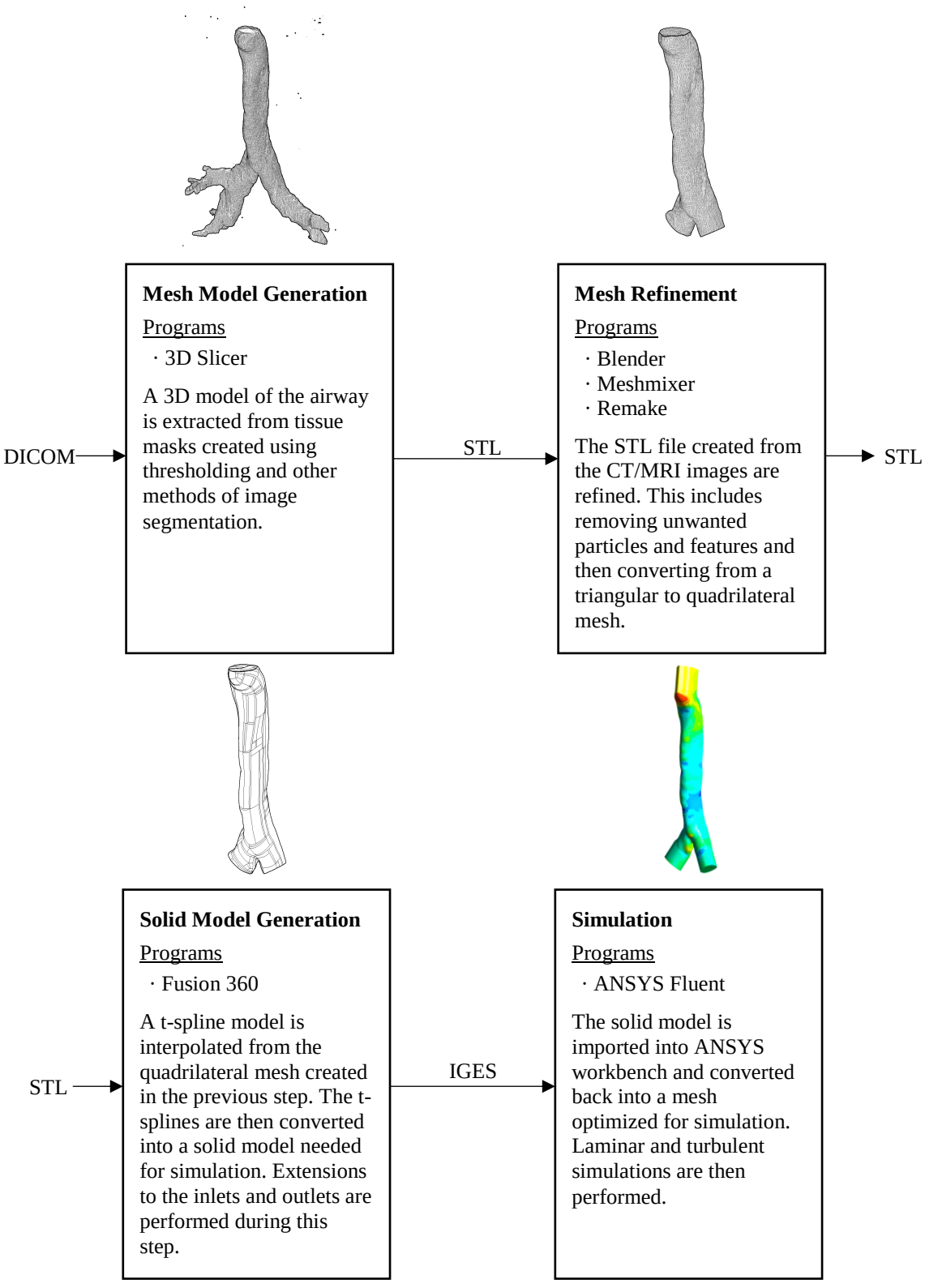

Figure 33: Flow Diagram of Data Manipulation Required for CFD Simulation.

5.2 WINTER QUARTER (2016-2017)

5.2.1 PATIENT A – DATA SET #2

Additional MRI images for Patient A were received on November 11, 2016. The new set of data that was provided was a tissue volume (i.e., standard MRI) as oppose to cinematics that were provided in July 2016. The second set of data was composed of 31 images taken along the axial plane of the patient using 8 mm spacing. The locations of the axial slices are illustrated in Figure 34, where a screen save of the study is shown.[14] Immediately, the slice thickness of the new data set drew some concerns with the generation of an airway model. A slice thickness of 1 mm to 3 mm is typically preferred for use in model generation. Another concern associated with this data set is that it was labeled as "AX STIR 6 mm". The "6 mm" portion of this label leads one to believe that the spacing between slices is 6 mm thick, whereas inspection of these data proves otherwise. Despite these concerns, the 8 mm slice thickness did prove sufficient in generating an airway model, especially for the patient's trachea.

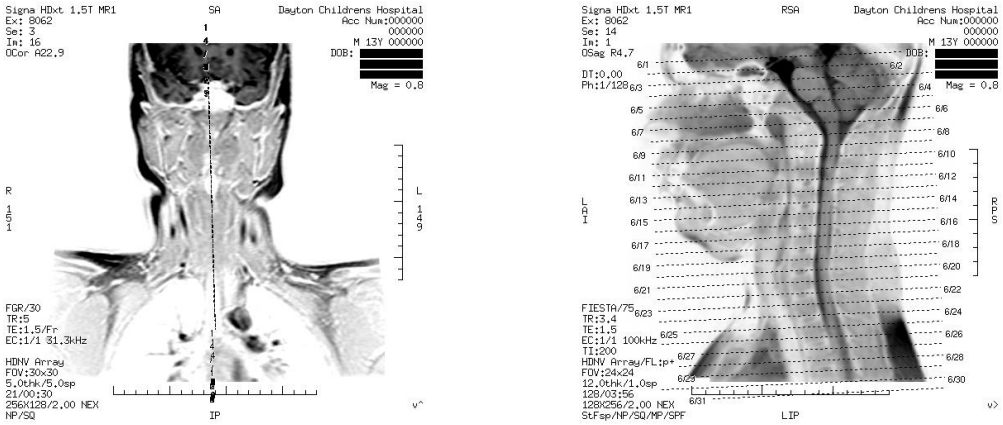

(a) Coronal View **(b) Saggital View**

Figure 34: Location of Axial Slices for Patient A – Data Set #2.

[14] The images shown within this figure have been inverted in color for improved readability.

5.2.1.1 MODEL GENERATION

A model of the airway for Patient A was generated utilizing similar methods that were used in the Fall Quarter for Patient B (see Section 5.1.2). It is important to note that an update to 3D Slicer shifted the model generation from the program's "Editor" to a new module labeled "Segmentations".[15] The underlying functions of these two modules are overall the same; however, changes in the work flow were introduced. The segmentations module also introduced a number of new features that were utilized during the second phase of the project. The most notable of these new features was the ability to create overlapping segments and real-time segmentation to model conversion. Previously label-maps had to be created within the Editor module and then manually converted to a 3D model. Unwanted features observed in this model then had to be removed by returning back to the editor, modifying the label map, and then generating a new model. The introduction of new features along with improved understanding of the program allowed for a more streamlined model creation process in comparison to the first phase of the project.

Model generation was divided into three phases. The first phase focused on the patient's lower airway, specifically the generation of a model for the trachea and bronchi. The second phase focused on the patient's upperairway. This pertained to generating a model for the patient's oral and nasal cavities. The final phase focused on analyzing the cinematics that were originally provided for the patient. In this phase, a model was not created directly from the MRI images. Instead, the cinematics were used to observe the

[15] The program was updated on November 8, 2016 to version 4.6. This new version introduced features that were not included in version 3.5.x that was used in the first phase of the project.

changes in the trachea's cross-sectional area. The extrema of these cross-sections were then used to dictate changes made to the base models created in the previous phases.

All three phases of the model generation process were performed within a single 3D Slicer project. This setup allowed for each phase to be treated separately, but also allowed for interaction between the models and improved flexibility. Furthermore, this project setup had the benefit that all data manipulation was isolated within a single file directory. Figure 35 is the subject hierarchy that was created for the project. As one can see, four series of MRIs were imported within the program. The 3 Plane Loc data are a single series but must be imported separately for each anatomical plane within 3D Slicer (see Section 5.1.1). This explains why six sets of MRI data are illustrated within the subject hierarchy, although only four unique series where used.

Figure 35: 3D Slicer Project Structure for Patient A.

Series 3 and Series 6 where used to generate the 3D models of the airway. Series 3 features the localized images that were included in the first set of data provided in July 2016, whereas Series 6 includes the axial slices that were provided in November 2016. Series 3 was not enough to generate solid models of the airway in the first phase of the project. Only a single axial image was provided within this series and the coronal and

sagittal images did not suffice because of their large slice thickness. The newly obtained axial images allowed for an acceptable model of the patient's airway to be extracted. The 8 mm slice thickness of Series 6, however, did result in a poor multiplanar reconstruction (MPR). This is illustrated in Figure 36, where the reconstructed sagittal and coronal views from Series 6 are shown. As one can see, these images are pixelated because of the large slice thickness that was used. As a result, the sagittal and coronal images from Series 3 were manually specified as an attempt to improve clarity. The result of this action is seen in Figure 37. It is important to note that although overriding the default MPR did result in improved image quality, it did require that the number of slices within these views be reduced.

(a) Axial **(b) Sagittal** **(c) Coronal**

Figure 36: Multiplanar Reconstruction of Patient A using Series 6 Axial Slices.

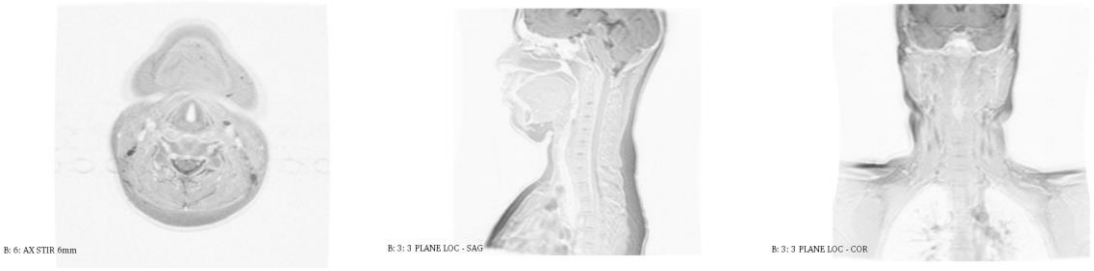

(a) Axial **(b) Sagittal** **(c) Coronal**

Figure 37: Multiplanar Visualization of Patient A using Series 6 Axial Slices and Series 3 Sagittal and Coronal Slices.

Despite using separate data for each anatomical view, only the axial images from Series 6 were used for segmentation.[16] The sagittal and coronal views from Series 3 were mostly used as an aid during the segmentation process. Furthermore, a thresholding technique was not used to isolate the airway boundaries for Patient A. The lack of contrast between tissues resulted in undesired elements being highlighted during the thresholding process (the same effect is seen in Figure 20). If thresholding were to be used, these unwanted artifacts would then have to be removed manually for each slice. Because of this, a level tracing tool was used instead. Level tracing is similar to thresholding, but requires that the user highlight over the desired tissue using the mouse. The tool then develops a region in which the selected color intensity is uniform. This was deemed acceptable for the following reasons:

- The threshold in which the airway is highlighted is not important, as it does not correlate to tissue density and serves no aid in isolating tissue around the airways.
- The threshold that selects tissue around the airway is dependent on both the equipment and protocol used. Thus, this form of segmentation isn't repeatable and should be avoided as standard practice.
- The fluid domain (i.e., empty space) is desired. A thresholding technique can isolate the internal airways, but has the drawback of selecting the empty space surrounding the patient as well random artifacts. For the CT scan used in Section 5.1.2, the selection of the surroundings was avoided by creating a ROI. This

[16] This isn't entirely true. The axial images within Series 6 were used for segmentation of the trachea and nasal cavity. Part of the oral cavity was segmented using the sagittal view of Series 3 but the accuracy of this model is questionable and discussed later on within this document.

isolated the trachea and removed the surroundings. This does not affect the artifacts created during the thresholding process.

Utilizing the level tracing tool, the boundaries of the trachea were selected and a 3D model was generated. A Gaussian smoothing factor of 50% was used for the model. This allowed for a smooth transition between each slice and a more realistic representation of the trachea. The 50% smoothing factor was chosen out of preference and can be changed at the discretion of the user; however, it should be noted that a smoothing factor larger than 50% can over simplify the model, resulting in a loss of defining geometry. Unlike before, this edit was made within 3D Slicer and not within Autodesk Meshmixer or Blender. The changes within the segmentation process made working with preliminary models easier and reduced the need for post-editing. Figure 38 illustrates the preliminary 3D models that were created for Patient A's trachea. The image on the left is the raw 3D model that was created from the isolated voxels, whereas the image on the right is the same model with the 50% smoothing factor applied.

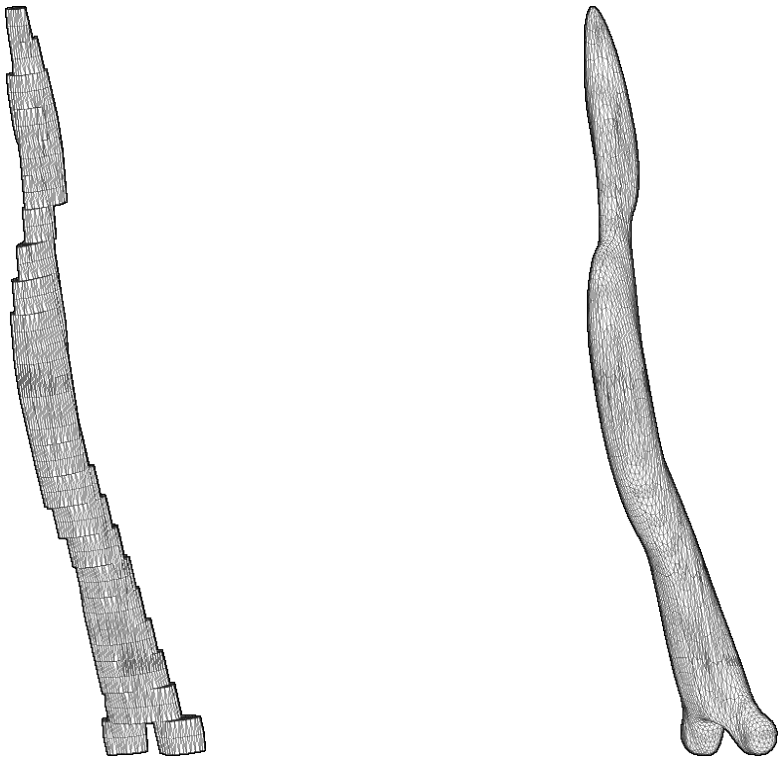

(a) Raw Voxel Model **(b) Smoothed Model**

Figure 38: Preliminary Trachea Model of Patient A Exported from 3D Slicer.

The smoothed trachea model was then imported into Autodesk Remake for re-meshing. As mentioned within Section 5.1.2, several conversion processes are necessary to prepare models for simulation. In this case the first conversion process involved converting the triangular mesh of the airway to a quadrilateral mesh within Remake. The mesh generated within this program is specifically designed to work with Autodesk Fusion 360. Within Fusion 360, the quadrilateral mesh of the trachea was then converted into a t-spline model that was later used to generate a solid, water-tight body. Once a solid model was obtained, the model was then prepared for simulation. This process involved slicing the bottom and top of the trachea and extending the resulting surfaces by three hydraulic diameters, respectively. The final model (i.e., the model prepared for simulation) is shown in Figure 39. As one will notice, the top inlet and bronchi

have been extended for simulation. Each of these inlets/outlets were extended by 15 mm, exceeding the minimum requirement of three hydraulic diameters.

The non-medical background of the author proved troublesome when developing models for Patient A's oral and nasal cavities. The cavities within the head have a complex shape in comparison to the almost pipe-like nature of the trachea. This meant that the abruptly changing geometry of the cavities became hard to capture because of the large slice thickness of the second data set. Because of these difficulties, some time was spent reviewing the structure of cavities (see Section 4.1.1). Unfortunately, their exact structure could not be replicated in the fluid domain model for Patient A. This is illustrated in Figure 40, where the total fluid domain of Patient A's airway is shown. In this figure, the pink, green, and blue geometry represent the fluid domain of the nasal cavity, oral cavity, and trachea, respectively.

The models generated in Figure 39 and Figure 40 were a significant improvement over the one shown in Figure 19. This improvement was greatly influenced by the new data set that was provided. Series 6 of the MRI images allowed for the direct generation of the trachea and nasal cavities. The image quality within the axial images allowed for good contrast between the airway tissue and empty space where the number of slices allowed for more geometry to be extracted. It was the improved understanding of 3D Slicer that allowed for the partial generation of the oral cavity. The patient's oral cavity was generated using the sagittal images that were originally provided within Series 3. Again, the provided slice thickness meant that only three slices could be used for defining this geometry.

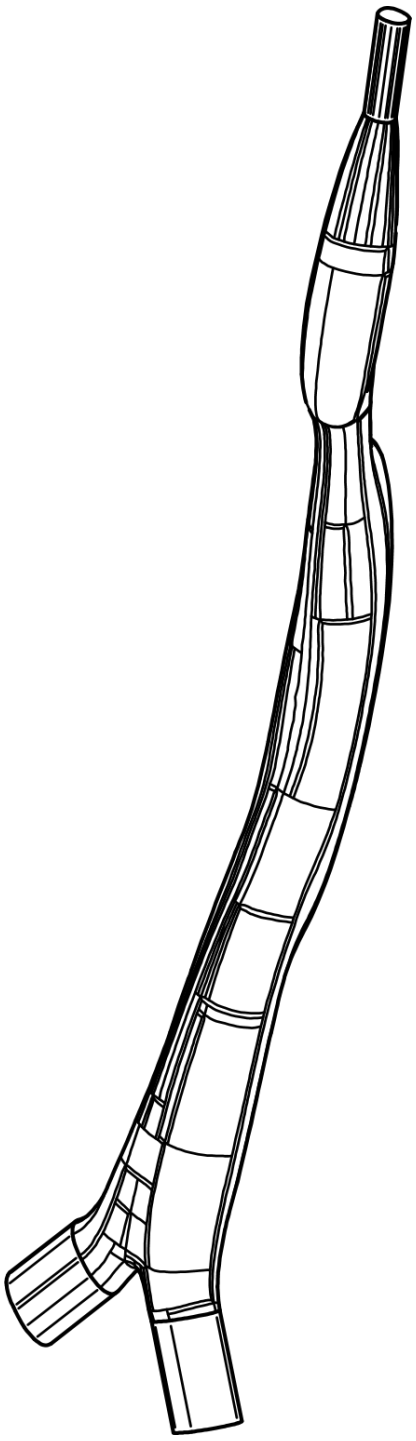

Figure 39: Final Trachea Model of Patient A Prepared for Simulation.

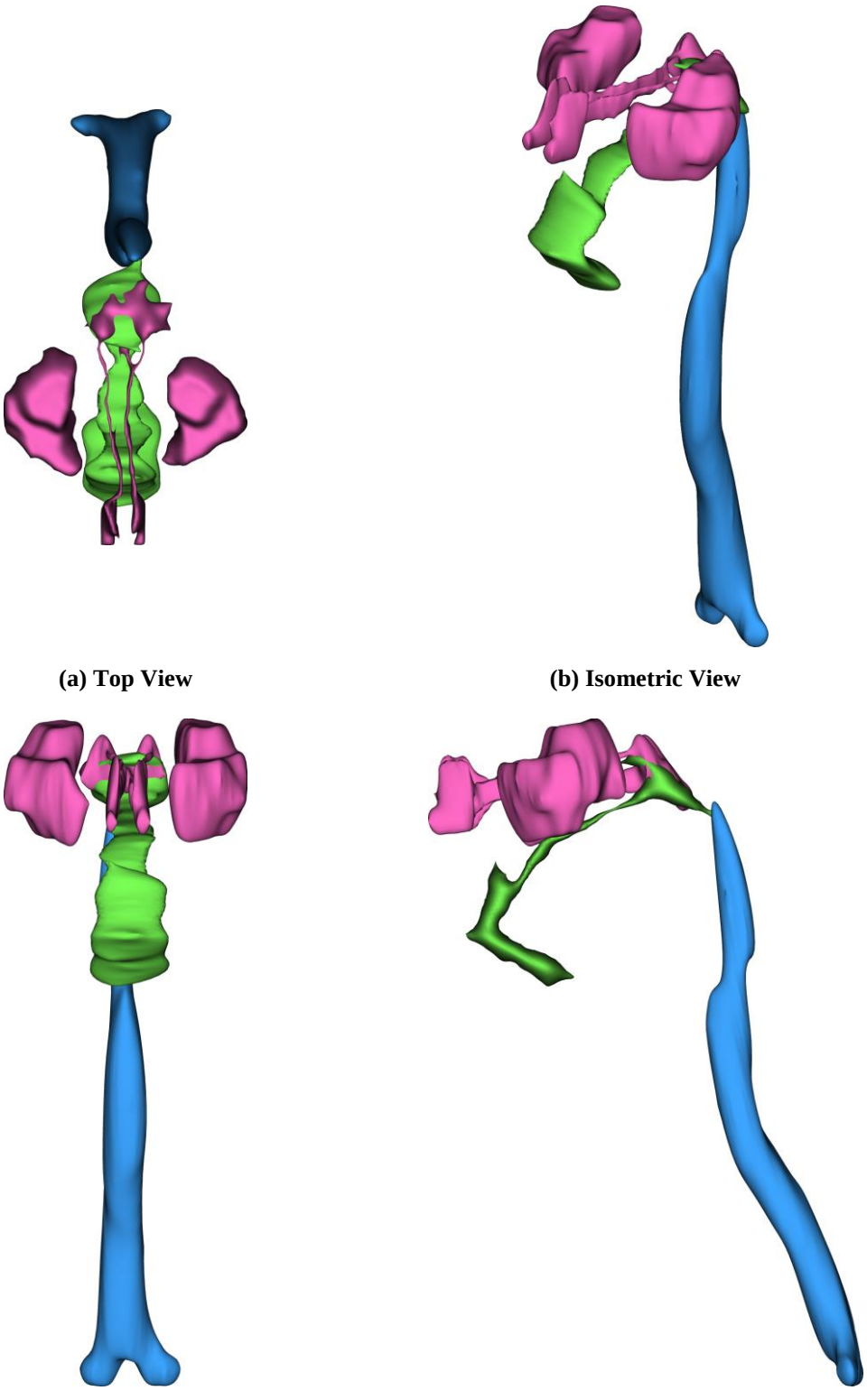

(a) Top View **(b) Isometric View**

(c) Front View **(d) Right View**

Figure 40: Total Captured Fluid Domain Model for Patient A.

Although there was some success in generating the nasal or oral cavities, the models could not be used for simulation. The fluid domain of the nasal cavity is discontinuous with islands (sinuses) existing left and right of what appears to be channels of the nose. These channels are small features that would prove troublesome in a CFD application. Furthermore, the nasal cavity that is shown represents the small portion that could be captured. The oral cavity could not be used for simulation because it represents the fluid domain for when the patient's mouth is closed. Any simulations of this geometry would not accurately depict the fluid flow behavior. Thus, only the trachea model (Figure 39) was used.

5.2.1.2 Multi-Volume (Cine MRI) Analysis

The cine MRI images could not be analyzed within 3D Slicer. Instead, an image editing program called GIMP was utilized.[17] The DICOM images were converted into a bitmap format that allowed them to be manipulated within the application. The threshold range of each image was modified so that there would be better contrast between the tissue and empty space. For each image, the cross-section of the airway was isolated using a "fuzzy select" tool. This tool is analogous to the level tracing tool within 3D Slicer and allows a user to highlight a region by selecting a single point. For this project, the tool was configured to highlight all the pixels within a ± 10 threshold region. Figure 41 illustrates some of the cross-sections that were isolated during this process.

[17] GIMP (GNU Image Manipulation Program) is a free/open source image editing program that is similar to Adobe Photoshop.

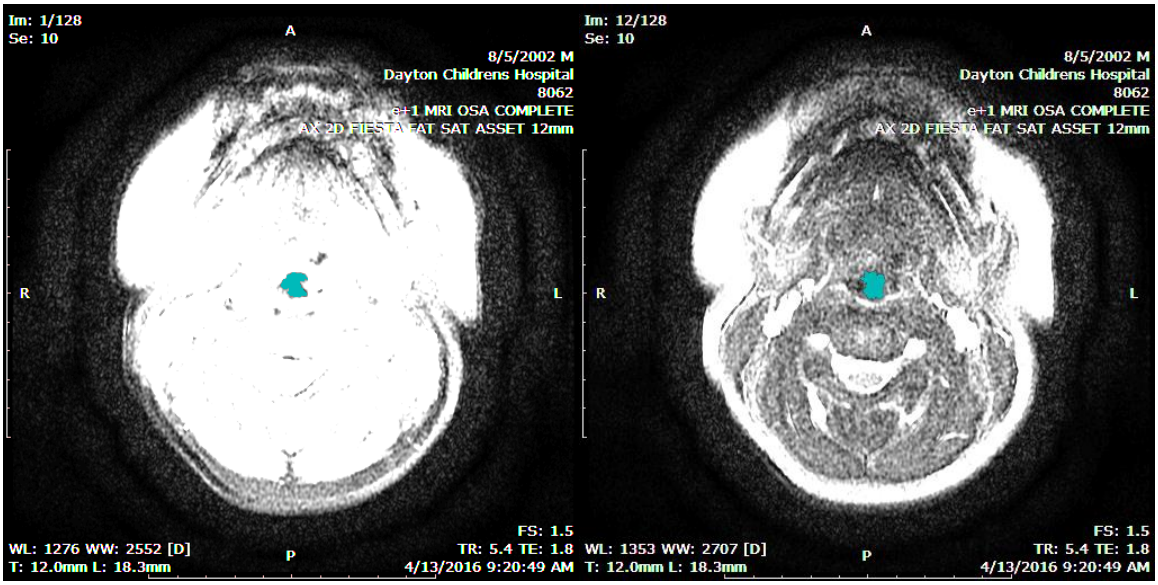

(a) Image 1 **(b) Image 12**

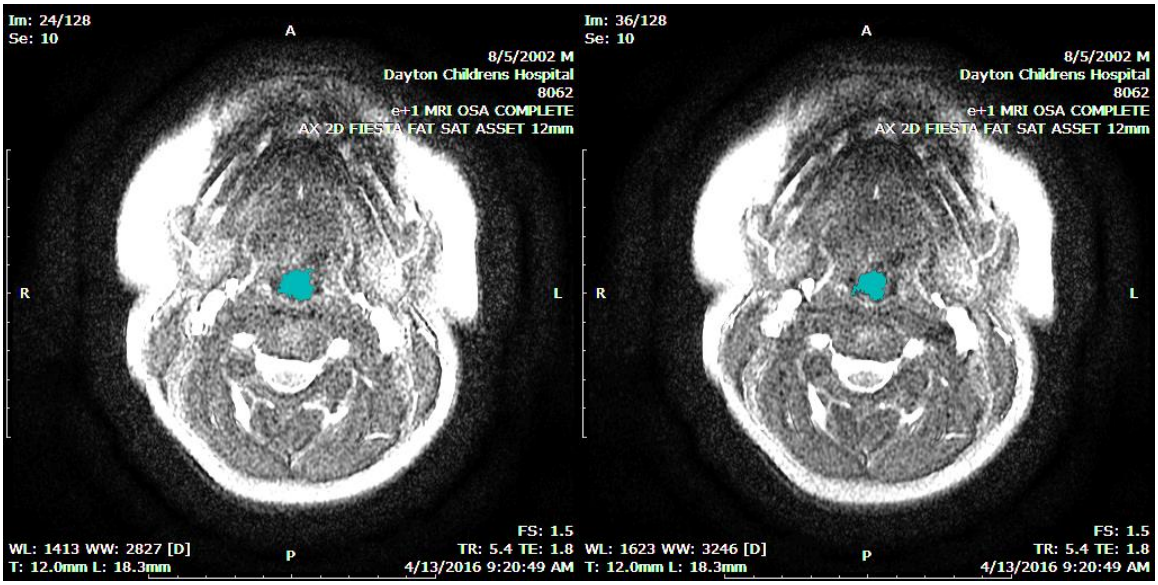

(c) Image 24 **(d) Image 36**

Figure 41: Captured Cross-sections for Various Images within Series 10

In each image, the blue regions represent the cross-section of the airway that was isolated. As one can see, a noticeable amount of noise is present within these images. As

a result, it was difficult to isolate the cross-sections with high accuracy. The area of the selected regions was determined by multiplying the pixel area by the corresponding number of pixels. For the cine MRIs, each pixel had an area of 0.153 mm^2. Figure 42 is a scatter plot showing the change in cross-sectional area for 64 images within the series. This chart represents half of the images within the series and 1 minute of respiration.

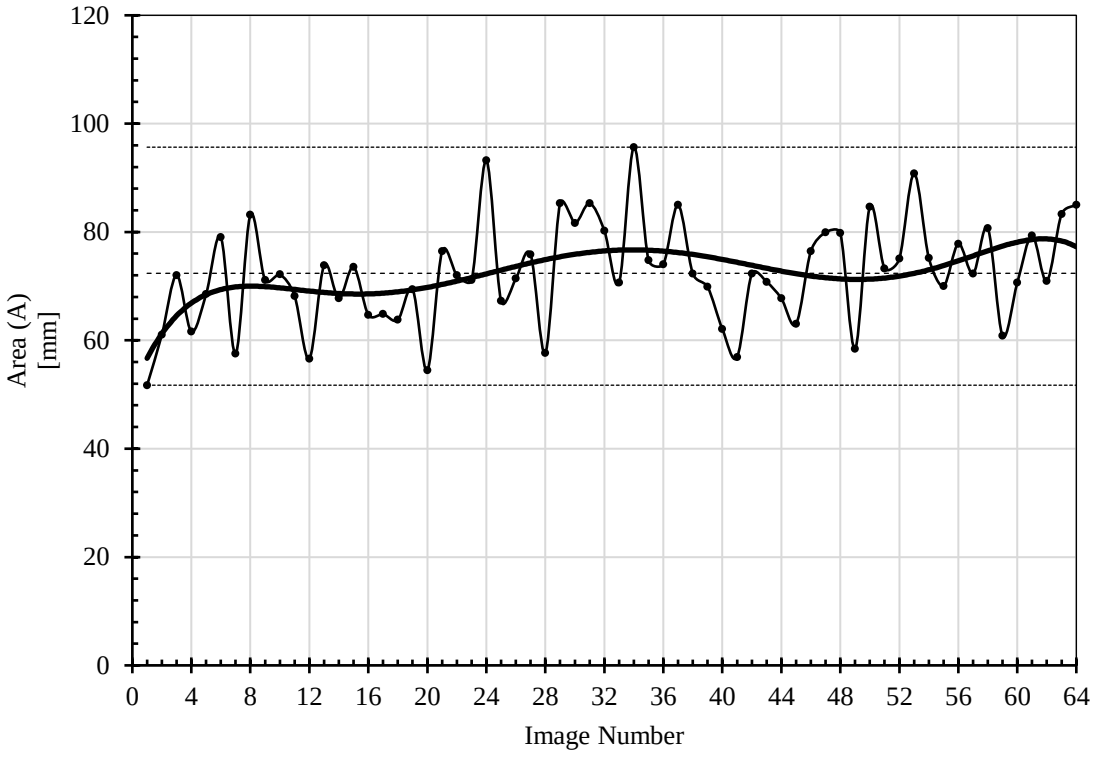

Figure 42: Cross-Sectional Area versus Image Number for Series 10.

The cross-sectional area of the airway changes abruptly from each image. A sixth order polynomial was fitted onto the data in an attempt to discover an underlying pattern. The three smallest and three largest areas within these data were used to determine a minimum and maximum value. The first three maxima and minima are listed in Table 13. The average of these values resulted in a minimum cross-sectional area of 54.3 mm^2 and a maximum of 93.2 mm^2. The static model at the same location of the cine MRI had a

cross-sectional area of 69.55 mm^2. The percent difference of these values to the static airway model are listed in Table 14. The difference listed in this table was then used to modify the radial dimension of the static airway model for additional simulation (see Appendix C). This would ensure that the study would represent all stages of respiration.

Table 13: First Three Minima and Maxima of Airway Cross-sectional Area.

Area (A) [mm^2]	
Minima	Maxima
51.7	90.8
54.5	93.2
56.6	95.7

Table 14: Percent Difference between the Average Minimum and Maximum Cross-Sectional Area from Static Airway Model.

Type	Area ($\bar{A}$) [mm^2]	Percent Difference from Static Model [%]	Required Scaling Factor (n) [n/a]
Minimum	54.3	24.6	0.884
Maximum	93.2	29.1	1.158

*The scaling factor is calculated by taking the square root of the minimum or maximum area divided by the cross-sectional area of the static model.

5.2.1.3 SIMULATION

Unlike the first phase of the project, only a fine mesh of the trachea was developed for simulation; a mesh independence study was not deemed necessary. The resulting mesh consisted of 509,113 elements and 175,636 nodes (near the limit of the

ANSYS academic version). Mesh inflation was used to properly capture boundary layer development near the airway walls (see Figure 27). Table 15 lists the mesh metrics that were observed for the trachea model. This model was deemed sufficient for simulation because the values in this table met the recommended metrics that were provided by ANSYS (Table 7). The parameters listed in Table 3 were used to set up the CFD model. From this table, the density and viscosity of the air were used to define the fluid properties, whereas the mass flow rate and a zero-gauge pressure were used for boundary conditions. A steady-state k-ω turbulent model was used to analyze both inhalation and expiration.

Table 15: Mesh Metrics for Airway Mesh of Patient A.

Mesh Metric	Min	Max	Average	Standard Deviation
Orthogonal Quality	0.234	1.00	0.889	$8.55 \cdot 10^{-2}$
Skewness	$2.38 \cdot 10^{-4}$	0.799	0.234	0.117

Figure 43 is the residual plot associated with the turbulent simulation for inhalation. Approximately 1,700 iterations were necessary to reach a converged solution. After this point, all the residuals except for continuity reached a magnitude of 10^{-6}. The error within the continuity equation converged to a magnitude of 10^{-3}. This result was deemed acceptable, as no large fluctuations were observed in the residual plot after convergence was said to occur.

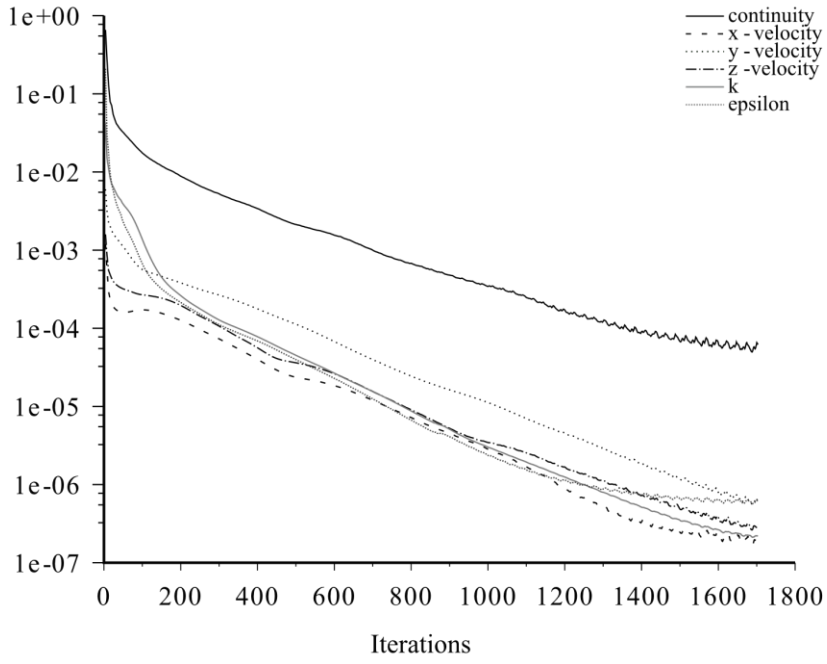

Figure 43: Residual Plot of Inspiration Simulation for Patient A.

A contour plot was used to visualize the velocity distribution along a section plane within the airway. As before, the non-uniform shape of the airway meant that a section could not be created perfectly in the middle of the trachea. Instead, an approximation was used to divide the trachea as evenly as possible. Figure 44 and Figure 45 illustrate the inhale and exhale velocity contour plot at this plane. These figures show that the velocity is the largest near the oropharynx because of its small cross-sectional area. As expected, the magnitude decreases as the cross-section increases. A vector plot was then used to observe the direction of airflow and to identify the location of eddies. These plots are shown in Figure 46 and Figure 47.

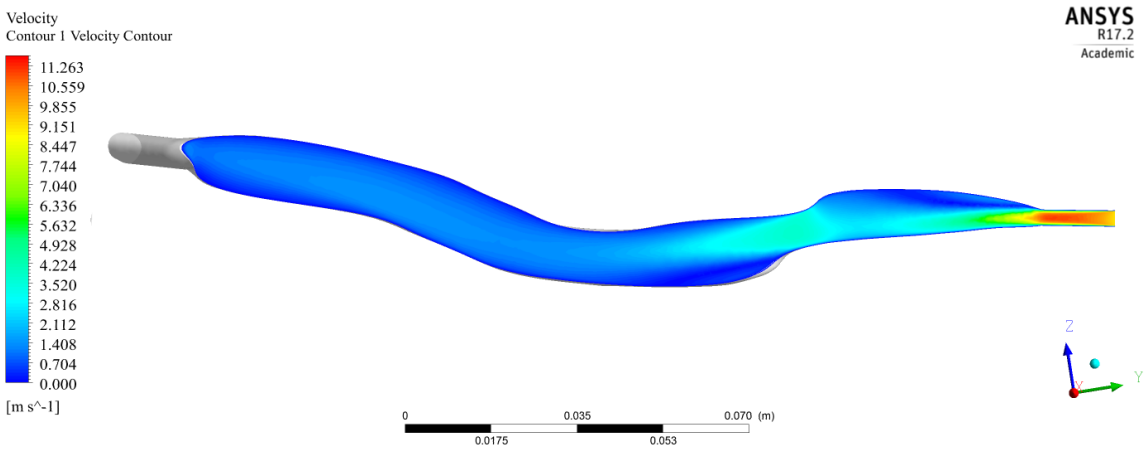

Figure 44: Velocity Contour Plot for an Inhale.

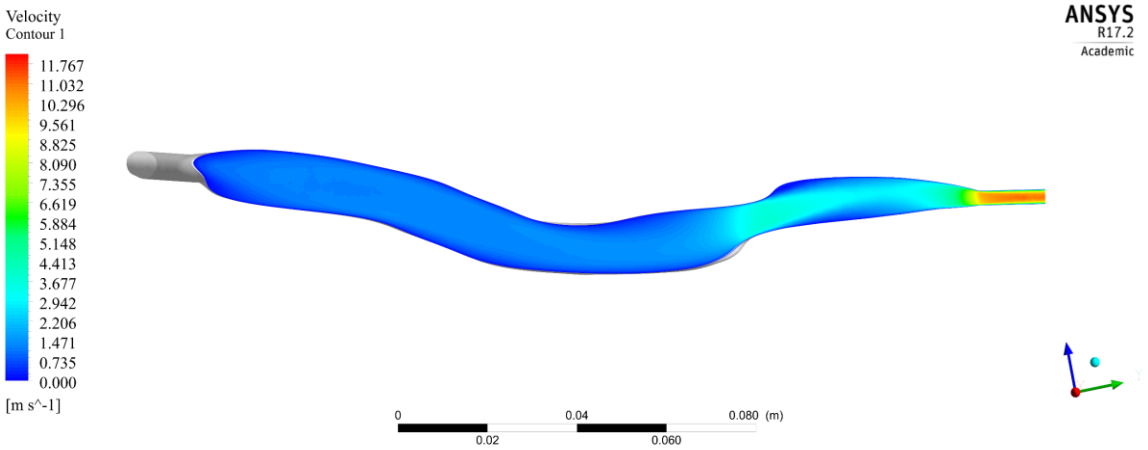

Figure 45: Velocity Contour Plot for an Exhale.

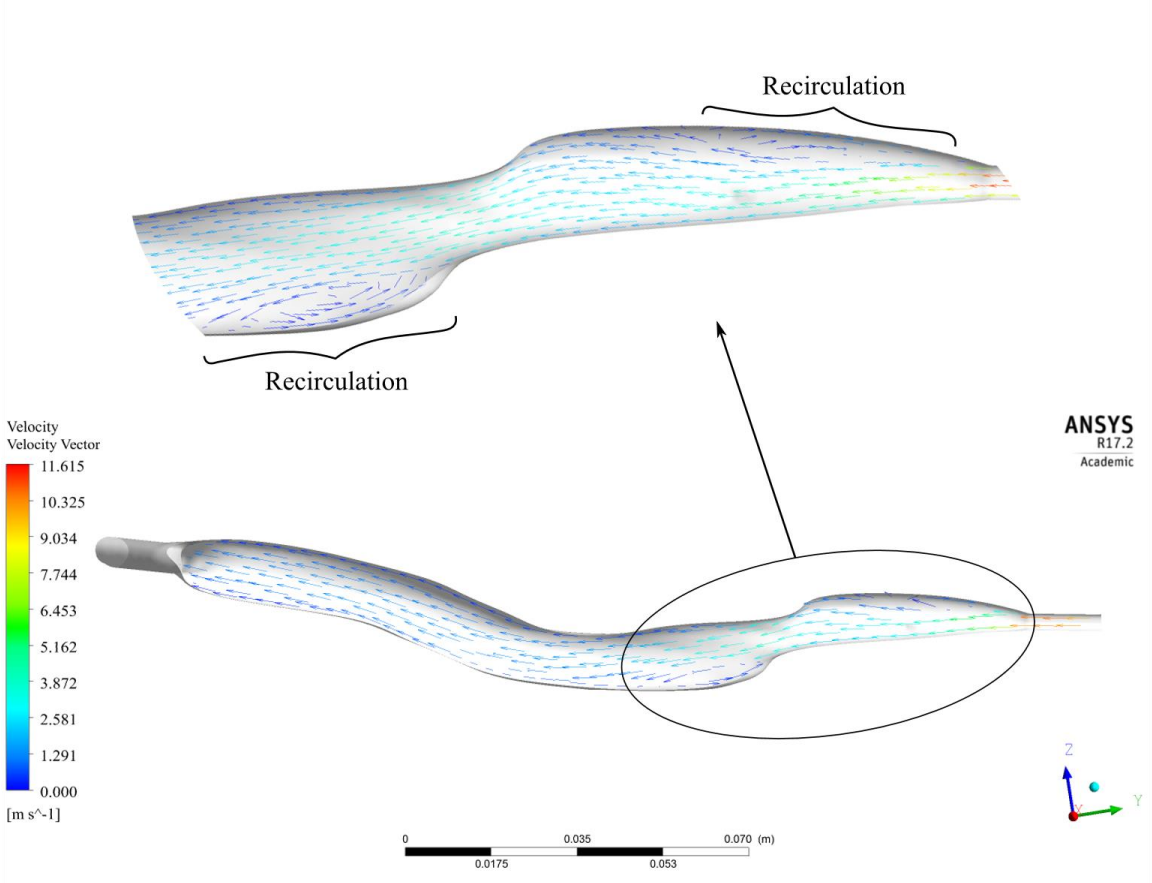

Figure 46: Velocity Vector Plot for an Inhale.

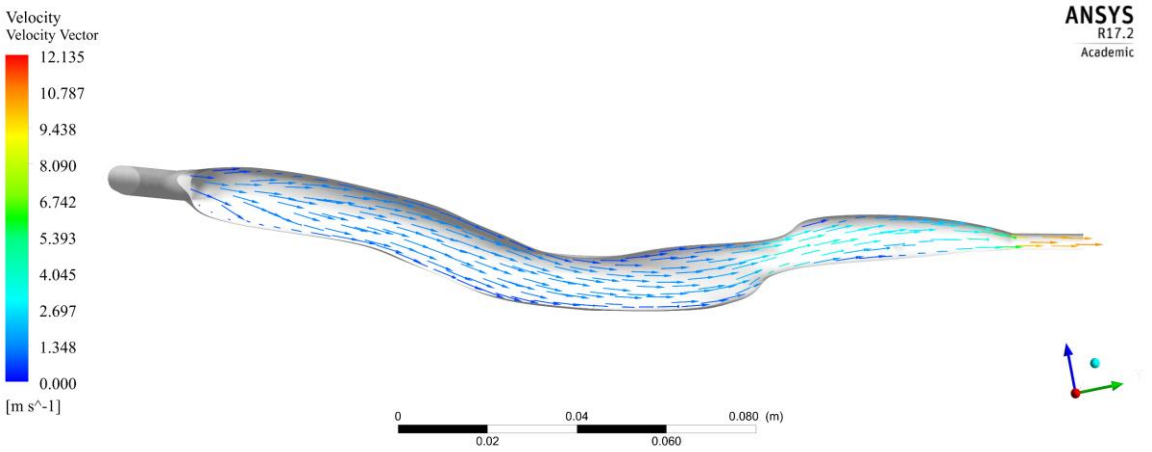

Figure 47: Velocity Vector Plot for an Exhale.

Recirculation was observed in both the inhale and exhale models with the largest recirculation noted in Figure 46. In both models, the recirculation did not interfere with

the overall quantity of air leaving or entering the lungs. Pressure contours were then utilized to identify location of stress on the airway walls. The pressure contours are shown in Figure 48 and Figure 49 for inhalation and expiration, respectively. The contour surface plot for an inhale details that much of airway experiences low-gauge pressure. The largest pressure gradient occurs at the top of the airway because of a large negative (or vacuum) pressure near the inlet extension. This pressure gradient is what results in the large air velocity at the inlet. The internal velocity decreases upon entering the larger regions of the airway. It should be noted that the smooth transition of the bronchi in this model removed large pressures that were previously experienced in the sample airway model (see Section 5.1.2). Larger pressures were observed in the exhale simulation. In Figure 49, one can see that much of the airway experiences pressure around 88 Pa. The higher pressures in the exhale model are expected, as the top of the airway behaves as a nozzle. In both simulations, the pressures experienced on the airway walls are small. The maximum pressure on the exhale model correlates to approximately 0.013 psi.

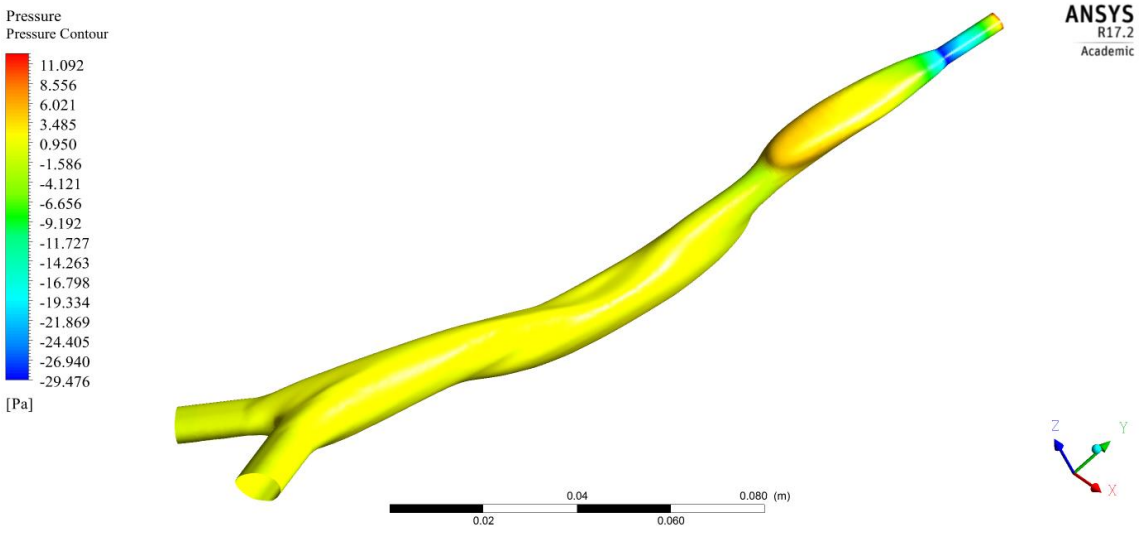

Figure 48: Pressure Contour on Wall Surface for Inhale.

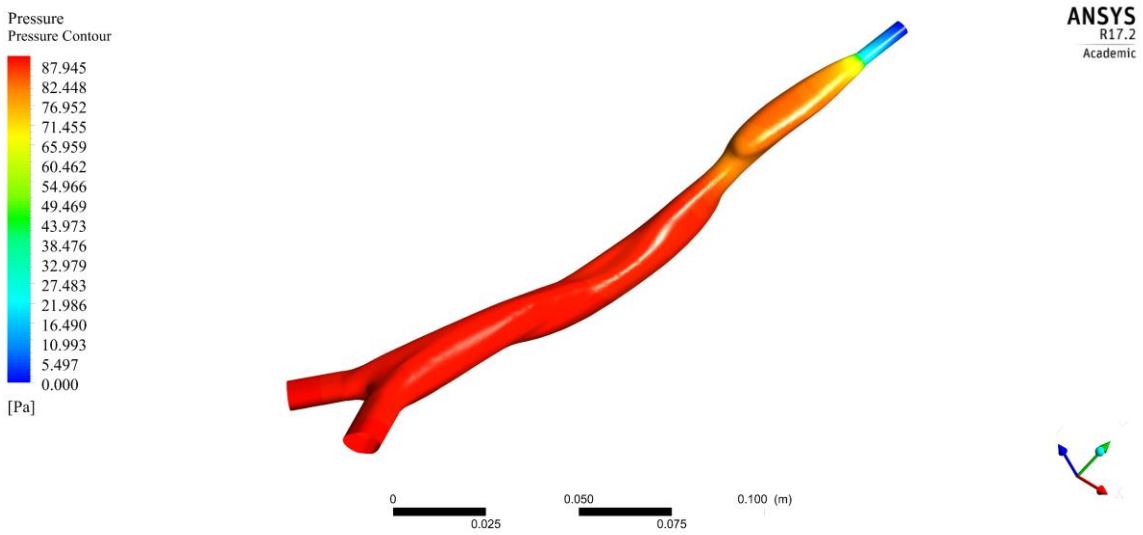

Figure 49: Pressure Contour on Wall Surface for Exhale

A conservation of mass calculation was performed to confirm the accuracy of the simulation results. Equation (41) through (45) were used to develop the mass balance of the system. Table 16 lists the cross-sectional areas that were used during calculation, while Table 17 summarizes the results obtained. The small percent difference between the simulated results and hand calculations indicate that continuity was satisfied and that the simulation results can be used in confidence.

Table 16: Cross-Sectional Area of Airway Geometry – Patient A.

Location	Cross-sectional Area [mm^2]
Inlet (A_i)	12.889
Outlet #1 (A_{o1})	53.501
Outlet #2 (A_{o2})	61.152

Table 17: Simulation Results versus Hand Calculation – Patient A.

Average Outlet Velocity (v_o) [m/s]		Percent Difference [%]
Hand Calculation	From Simulation	
1.018	1.026	0.783

6. CONCLUSIONS

The first phase of the project cleared up questions regarding model generation. A three-dimensional (3D) model was successfully extracted from both MRI and CT studies utilizing an open-source segmentation program. Methods of model refinement were documented using an array of open source and freemium applications. The second phase of the project stressed the importance of image quality. A fine slice thickness and resolution is needed if models of the nasal/oral cavity are desired. The MRI images provided for this project had a resolution of 256 x 256, except for the two cine MRI series, which had a resolution of 512 x 512. The 256 x 256 resolution was not ideal for capturing the complex and abruptly changing geometry of the nasal cavity. The slice thickness in the region also became crucial factor of model quality. It was concluded that a finer resolution would be desired for the patient's head, but special consideration would need to be taken to account for the signal-to-noise ratio. The models of the trachea and bronchi were easily developed because of their pipe-like nature. Thus, pixel size and slice thickness did not play as large of a role within this region.

No significant conclusions could be drawn from the analysis of the cine MRI series. The cine MRIs had to be analyzed manually using an image editing program. This was unfavorable as the threshold region within a standard image format is much less than within a DICOM. The images within each cine series had a large amount of noise and the cross-sections extracted from these images were inconsistent. As a result, an underlying pattern could not be made about the airway's cross-sectional area over time. Nonetheless, the analysis performed was consistent with previous work performed by Dr. Kalra and Dr. Elluru. This suggests that the airway geometry may change erratically or that the sample rate of images is too slow to capture its behavior. The average of the first three

minima and maxima cross-sectional areas was used to determine the amount of dilation or erosion that had to be made to the static model. Simulation of these various models were then used to represent different states of respiration. Because of time constraints, this analysis was placed within Appendix C and serves as an extension of the analysis that is discussed in body of this report.

Time constraints, as well as other limiting factors, did interfere with goals proposed for this project. First, this project failed to analyze the airway geometry of three pediatric patients. Simulations were only performed for a single patient of Dr. Elluru and Dr. Kalra and for an airway created from sample CT images. These simulations were not compared to sleep studies. Furthermore, the simulations did not reveal any major obstructions within the airways. Nonetheless, the project was successful in alleviating some of the concerns that were addressed prior to its start. Specifically, it was determined that MRIs are more than fine in generating fluid domain models. The lack of contrast between various tissues, however, means that airway walls cannot be isolated. Thus, finite element analysis on the airway walls could not be performed without large assumptions made about its geometry and properties. In addition, this project addressed concerns regarding model refinement in CFD analysis.

The largest hurdle in this project was the segmentation of the DICOM images in both the static and cinematic series. Further development of this project would be best invested in developing software (or similar) for cine MRI analysis. Automation of this process would provide better insight into the changing geometry, reduce analysis time, and remove human error. Open-source CFD packages could also be used to automate problem setup and simulation; however, this could prove difficult, especially if dynamic breathing behavior is to be taken into consideration.

7. COMPLETED TASKS AND MILESTONES

Table 18 lists the tasks and milestones that were completed during the first and the second phase of the project (i.e., the 2016 Fall and Winter Quarters at MSOE). Project milestones are shown in bold.

Table 18: Completed Tasks for the Project.

Quarter	Week Number	Task Description
1st Quarter (Fall 2016)	1	**Project Start.** Continued work on the MRI study that was sent in the Summer. The MRI study was analyzed. Work was performed on the partial airway geometry, which was extracted using Mimics.
	2	Re-established contact with project advisors in the form of a project update. Issues with model generation from cine MRI data were discussed. Standard MRI studies were requested.
	3	Studied the use of 3D Slicer as an image segmentation tool to extract airway geometry. Spent the remainder of the week getting trained in the program and becoming more familiar with medical imaging.
	4	A second project update was sent. Work was halted on the MRI study because of modeling issues. An airway model was extracted from a sample CT study while awaiting new MRI studies.
	5	**Mesh Refinement.** STL files created using 3D Slicer were refined; particles and sharp edges were removed.

Table 18: Completed Tasks for the Project (continued).

1st Quarter (Fall 2016)	6	Mesh refinement was continued. Work was performed to convert STL mesh files to solid parts that could be modified in a traditional CAD program.
	7	A phone called was made to Dr. Elluru. The current work that was performed was discussed and notes were taken on how the project should move forward. It was agreed that work should be done to see how well standard MRIs work for 3D model generation and if a protocol can be established. Research should be made on 2D CFD simulations using profiles created from the cine MRIs.
	8	**Began Simulation.** The 3D model generated from the sample CT study was imported into ANSYS for a preliminary laminar flow simulation. Model convergence criteria and proper mesh characteristics required for simulation were researched.
	9	Continued CFD simulations. A mesh independence study was performed to observe the rate of convergence and the final pressure and velocity values for laminar and turbulent models. Results were documented in the project report.
	10	Submitted a draft of the project report. Began work on the PowerPoint presentation needed for the meeting with the advisory committee.
	11	**Completion of First Project Phase.** Meeting with advisory committee on November 11, 2016. A presentation was made on the work completed and a revised draft of the report was submitted.

Table 18: Completed Tasks for the Project (continued).

2nd Quarter (Winter 2016-2017)	1	Contacted Dr. Elluru and reviewed work that was to be completed during the second half of the project and discussed work already performed. Obtained the new MRI study for Patient A.
	2	Began work on all remaining airway models. This included model generation using 3D Slicer and refinement. Generated a preliminary model of Patient A's trachea.
	3	Worked within 3D Slicer in developing the nasal and oral cavity of Patient A. Developed the boundary conditions to be used for simulation.
	4	Continued refining models generated in the previous two weeks. Prepared the trachea model for simulation.
	5	**Began CFD Simulations.** Performed turbulent model simulations on the airway model obtained from MRI studies.
	6	Reviewed simulation results. The simulations were reviewed by Dr. Kumpaty to ensure their validity. Changes were made based on Dr. Kumpaty's feedback.
	7	**Began Finalizing Project Report.** Documented work completed during the 2nd quarter and begin compiling phase one and phase two reports. Compiled CFD results.

Table 18: Completed Tasks for the Project (continued).

2nd Quarter (Winter 2016-2017)	8	Completed all outstanding portions of the project. This included remaining fluid flow analysis, research, and so on. Reviewed the project's status with Dr. Elluru, Dr. Kalra, and Dr. Kumpaty during a conference call on February 2, 2017.
	9	Prepared for project close. Submitted the initial draft of the capstone report.
	10	Prepared for the final project presentation. This included creating a PowerPoint outlining the work performed throughout the two-quarter timeframe and completing the final project report.
	11	**Project Close.** Submittal of the final project report and meeting with the advisory committee.

REFERENCES

[1] National Institute of Neurological Disorders and Stroke, "Brain Basics: Understanding Sleep," National Institutes of Health (NIH), 25 July 2014. [Online]. Available: http://www.ninds.nih.gov/disorders/brain_basics/understanding_sleep.htm. [Accessed 10 May 2016].

[2] Division of Sleep Medicine at Harvard Medical School, "Natural Patterns of Sleep," Harvard University, 18 December 2007. [Online]. Available: http://healthysleep.med.harvard.edu/healthy/science/what/sleep-patterns-rem-nrem. [Accessed 10 May 2016].

[3] Division of Sleep Medicine at Harvard Medical School, "Sleep, Learning, and Memory," Harvard University, 18 December 2007. [Online]. Available: http://healthysleep.med.harvard.edu/healthy/matters/benefits-of-sleep/learning-memory. [Accessed 10 May 2016].

[4] Division of Sleep Medicine at Harvard Medical School, "Consequences of Insufficient Sleep," Harvard University, [Online]. Available: http://healthysleep.med.harvard.edu/healthy/matters/consequences. [Accessed 10 May 2016].

[5] H. Radhakrishnan and S. Kassinos, "CFD Modeling of Turbulent Flow and Particle Deposition in Human Lungs," *31st Annual International Conference of the IEEE Engineering in Medicine and Biology Society,* pp. 2867-2870. IEEE, Minneapolis, 2009.

[6] G. Tanaka, M. Ohgawara, G. Inagaki, M. Hishida and T. Sera, "Kinematic Irreversibility of Oscillatory Flow in Expanding and Contracting Small Airways,"*International Journal of Heat and Mass Transfer*, Vol. 56, pp. 1873-1880, 2012.

[7] P. Saksono, P. Nithiarasu, I. Sazonov and S. Y. Yeo, "Computational Flow Studies in a Subject-Specific Human Upper Airway Using a One-Equation Turbulence Model. Influence of the Nasal Cavity," *International Journal for Numerical Methods in Engineering*, Vol. 87, pp. 96-114, 2011.

[8] C.-L. Lin, M. Tawhai, G. Mclennan and E. A. Hoffman, "Characteristics of the Turbulent Laryngeal Jet and Its Effect on Airflow in the Human Intra-thoracic Airways," *Respiratory Physiology & Neurobiology*, Vol. 157, pp. 295-309, 2007.

[9] Boston Children's Hospital, "The Future of Cardiac MRI: 3-D Cine," Boston Children's Hospital Science and Clinical Innovation Blog, 12 December 2016. [Online]. Available: https://vector.childrenshospital.org/2016/12/the-future-of-cardiac-mri-3-d-cine/. [Accessed 20 January 2017].

[10] D. Rutkowski, "Computational Fluid Dynamics of the Pediatric Trachea," Milwaukee School of Engineering (MSOE), Milwaukee, 2013, [Online]. Available: https://community.msoe.edu/docs/DOC-4212

[11] Materialise, "Materialise Mimics," Materialise, [Online]. Available: http://biomedical.materialise.com/mimics. [Accessed 10 May 2016].

[12] Materialise, "Materialise: Software & Services for Biomedical Engineering," Materialise, [Online]. Available: http://biomedical.materialise.com/. [Accessed 10 May 2016].

[13] X. Y. Luo, J. S. Hinton, T. T. Liew and K. K. Tan, "LES Modeling of Flow in a Simple Airway Model," *Medical Engineering & Physics*, Vol. 26, pp. 403-413, 2004.

[14] National Heart, Lung, and Blood Institute, "The Respiratory System," U.S. Department of Health & Human Services, 17 July 2012. [Online]. Available: http://www.nhlbi.nih.gov/health/health-topics/topics/hlw/system. [Accessed 27 April 2016].

[15] LadyofHats, "Respiratory System Complete," Wikimedia Foundation, Inc., 13 December 2007. [Online]. Available: https://upload.wikimedia.org/wikipedia/commons/5/5e/Respiratory_system_complete_en.svg. [Accessed 27 April 2016].

[16] R. L. Drake, A. W. Vogl and A. W. M. Mitchell, *Gray's Anatomy for Students*, Philadelphia: Churchill Livingstone Elsevier, 2015.

[17] Wikimedia Foundation, Inc., "Tidal Volume," Wikimedia Foundation, Inc., 16 December 2015. [Online]. Available: https://en.wikipedia.org/wiki/Tidal_volume. [Accessed 11 January 2017].

[18] S. Kang and A. Fetterman, "Vital Signs (Body Temperature, Pulse Rate, Respiration Rate, Blood Pressure)," University of Rochester Medical Center, [Online]. Available:

https://www.urmc.rochester.edu/encyclopedia/content.aspx?ContentTypeID=85&ContentID=P00866. [Accessed 11 January 2017].

[19] Wikimedia Foundation, Inc., "Respiratory Minute Volume," Wikimedia Foundation, Inc., 8 April 2016. [Online]. Available: https://en.wikipedia.org/wiki/Respiratory_minute_volume. [Accessed 11 January 2017].

[20] D. Currie, "Lung Volumes and Capacities," East Tennessee State University, 5 January 2009. [Online]. Available: http://faculty.etsu.edu/currie/respvolumes.htm. [Accessed 11 January 2017].

[21] University of Iowa Healthcare, "Pediatric Vital Signs Normal Ranges," University of Iowa Healthcare, 2016 December 2016. [Online]. Available: https://iowaheadneckprotocols.oto.uiowa.edu/display/protocols/Pediatric+Vital+Signs+Normal+Ranges. [Accessed 11 January 2017].

[22] A. Selvakumar, V. Noronha and P. M. Sundaram, *Atlas of Imaging in Ophthalmology*, Jaypee Brothers Medical Publishing, 2014.

[23] MRI Master, "Resolution and Image Quality," [Online]. Available: https://mrimaster.com/index.4.html. [Accessed 27 October 2016].

[24] EB Medicine, "Basic Principles of MRI," EB Medicine, [Online]. Available: https://www.ebmedicine.net/topics.php?paction=showTopicSeg&topic_id=178&seg_id=3754. [Accessed 23 October 2016].

[25] Wikimedia Foundation, Inc., "Hounsfield scale," Wikimedia Foundation, Inc., 30 September 2016. [Online]. Available: https://en.wikipedia.org/wiki/Hounsfield_scale. [Accessed 23 October 2016].

[26] Materlise NV, "Mimics Student Edition Course Book," Materlise NV, Leuven, 2012.

[27] D. R. Molteni, *From CT Numbers to Hounsfield Units in Cone Beam Volumetric Imaging: the Effect of Artifacts*, Chicago: American Academy of Oral and Maxillofacial Radiology, 2011. [Online]. Available: http://c.ymcdn.com/sites/www.aaomr.org/resource/resmgr/2012_Uploads/AAOMR2011_medicine.pdf

[28] World Health Organization, "Communicating Radiation Risks in Paediatric Imaging," WHO Press, Geneva, 2016.

[29] P. T. Norton, N. C. Nacey, D. B. Caovan, S. B. Gay, C. M. Kramer and B. S. Jeun, "Cine Imaging," University of Virginia Health System Department of Radiology, 2013. [Online]. Available: https://www.med-ed.virginia.edu/courses/rad/cardiacmr/Techniques/Cine.html. [Accessed 30 April 2016].

[30] American Syringomylia & Chiari Alliance Project, "Cine MRI," 2 December 2009. [Online]. Available: http://asap.org/index.php/medical-articles/cine-mri/. [Accessed 29 April 2016].

[31] Wikimedia Foundation, Inc., "Functional magnetic resonance imaging," Wikimedia Foundation, Inc., 18 August 2016. [Online]. Available:

https://en.wikipedia.org/wiki/Functional_magnetic_resonance_imaging. [Accessed 13 October 2016].

[32] R. H. Turner and Y. A. Cengel, "Introduction to Fluid Mechanics," in *Fundamentals of Thermal-Fluid Sciences*, McGraw-Hill Higher Education, 2005, pp. 463-484.

[33] D. S. Kumpaty, *Boundary Layer Presentation*, Milwaukee: Milwaukee School of Engineering, 2016.

[34] H. K. Versteeg and W. Malalasekera, *An Introduction to Computational Fluid Dynamics: The Finite Volume Approach*, England: Pearson Education Limited, 2007.

[35] F. M. White, *Fluid Mechanics*, New York: McGraw-Hill, 2011.

[36] J. Anderson, *Computational Fluid Dynamics*, McGraw-Hill Education, 1995.

[37] N. Hall, "Navier-Stokes Equations," National Aeronautics and Space Administration (NASA), 5 May 2015. [Online]. Available: http://www.grc.nasa.gov/WWW/k-12/airplane/nseqs.html. [Accessed 29 April 2016].

[38] J. Anderson, "The Pressure Correction Technique: Application to Incompressible Viscous Flow," in *Computational Fluid Dynamics*, McGraw-Hill Education, 1995, pp. 248-263.

[39] J. Anderson, "Incompressible Couette Flow: Numerical Solutions by Means of an Implicit Method and the Pressure Correction Method," in *Computational Fluid Dynamics*, McGraw-Hill Education, 1995, pp. 416-446.

[40] Medixant, *RadiAnt DICOM Viewer,* Poznan: Medixant, 2016.

[41] Softways, "Fat Saturation," Magnetic Resonance - Technology Information Portal, 6 September 2016. [Online]. Available: http://www.mr-tip.com/serv1.php?type=db1&dbs=Fat%20Saturation. [Accessed 24 September 2016].

[42] A. Fedorov, R. Beichel, J. Kalpathy-Cramer, J. Finet, J.-C. Fillion-Robin, S. Pujol, C. Bauer, D. Jennings, F. Fennessy, M. Sonka, J. Buatti, S. Aylward, J. Miller, S. Pieper and R. Kikinis, "3D Slicer as an Image Computing Platform for the Quantitative Imaging Network," *Magnetic Resonance Imaging,* Vol. 30, no. 9, pp. 1323-1341, 2012.

[43] 3D Slicer, "3D Slicer," Boston's Brigham and Women's Hospital & Hardvard Medical School, 2016. [Online]. Available: http://www.slicer.org. [Accessed 11 October 2016].

[44] "3DSlicer," Wikimedia Foundation, Inc., 13 October 2016. [Online]. Available: https://en.wikipedia.org/wiki/3DSlicer. [Accessed 15 October 2016].

[45] Center for Information Technology Renato Archer (CTI), "About Invesalius," Center for Information Technology Renato Archer (CTI), 2016. [Online]. Available: http://www.cti.gov.br/invesalius/?page_id=14. [Accessed 22 October 2016].

[46] I. Young, J. Gerbrands and L. van Vliet, "Segmentation," Vilnius University - Faculty of Mathematics and Computer Science, 20 February 2009. [Online].

Available: http://www.mif.vu.lt/atpazinimas/dip/FIP/fip-Segmenta.html. [Accessed 23 October 2016].

[47] Wikimedia Foundation, Inc., "STL (file format)," Wikimedia Foundation, Inc., 20 October 2016. [Online]. Available: https://en.wikipedia.org/wiki/STL_(file_format). [Accessed 23 October 2016].

[48] 3D Systems, Inc., "Geomagic Design X," 3D Systems, Inc., 2016. [Online]. Available: http://www.geomagic.com/en/products-landing-pages/designx. [Accessed 23 October 2016].

[49] Autodesk, Inc., "Autodesk Meshmixer," Autodesk, Inc., [Online]. Available: http://www.meshmixer.com/. [Accessed 23 October 2016].

[50] Autodesk, Inc., "Working with STL Files | Autodesk Memento + Fusion 360," Autodesk Fusion 360, 25 February 2016. [Online]. Available: https://www.youtube.com/watch?v=rhk9l_OlPR4. [Accessed 3 October 2016].

[51] Autodesk, Inc., "Autodesk Remake," Autodesk, Inc., 2016. [Online]. Available: https://remake.autodesk.com/about. [Accessed 3 October 2016].

[52] Autodesk, Inc., "Fusion 360," Autodesk, Inc., 2016. [Online]. Available: http://www.autodesk.com/products/fusion-360/. [Accessed 3 October 2016].

[53] ANSYS, Inc., *Introduction to Fluent - Module 09: Best Practice Guidelines,* Canonsburg: ANSYS, Inc., 2016.

[54] R. L. Drake, A. W. Vogl, A. W. M. Mitchell, R. M. Tibbitts and P.E. Richardson, *Gray's Atlas of Anatomy,* Philadelphia: Churchill Livingstone Elsevier, 2015.

APPENDIX A: IRB CERTIFICATION

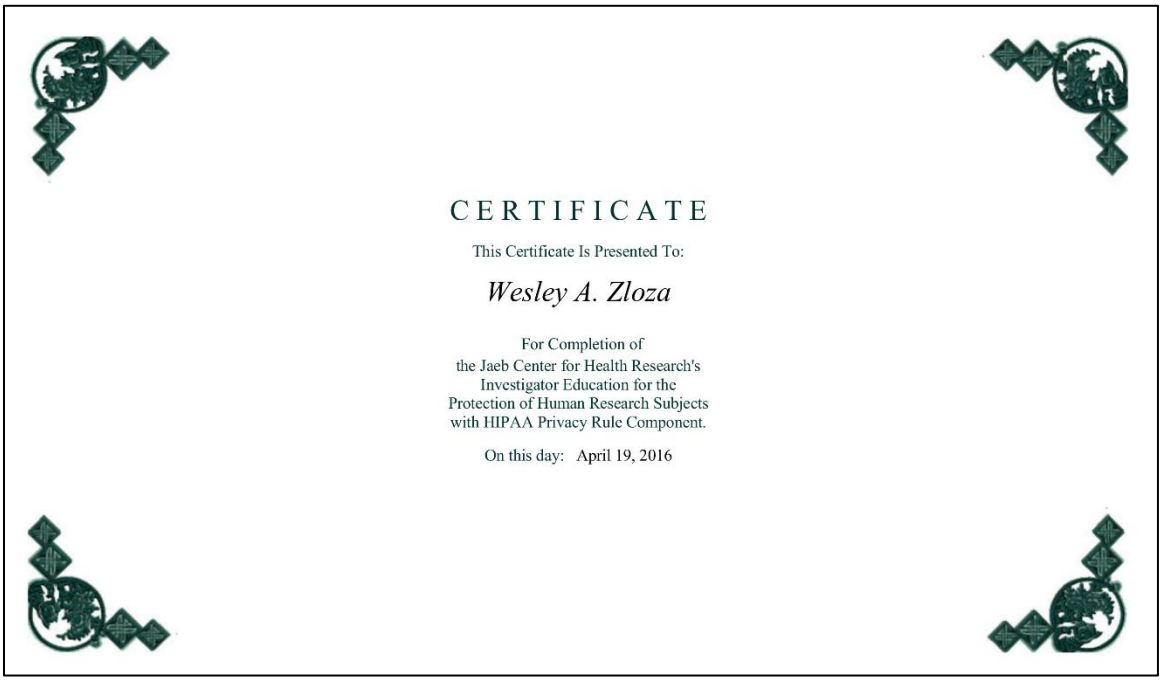

CERTIFICATE

This Certificate Is Presented To:

Wesley A. Zloza

For Completion of
the Jaeb Center for Health Research's
Investigator Education for the
Protection of Human Research Subjects
with HIPAA Privacy Rule Component.

On this day: April 19, 2016

Figure A-1: Certification for IRB Approval.

APPENDIX B: MEDICAL ILLUSTRATIONS

This appendix contains a series of medical illustrations that were used as a reference during the project. These illustrations were found in two publications: *Gray's Anatomy for Students*[1] and *Gray's Atlas of Anatomy*.[2] The appendix is split into two sections. The first section lists images correlating to the upper airway, specifically the nasal cavity and pharynx whereas the second section contains images that describe the geometry within the lower airway, specifically the trachea and bronchi.

B.1 UPPER AIRWAY GEOMETRY

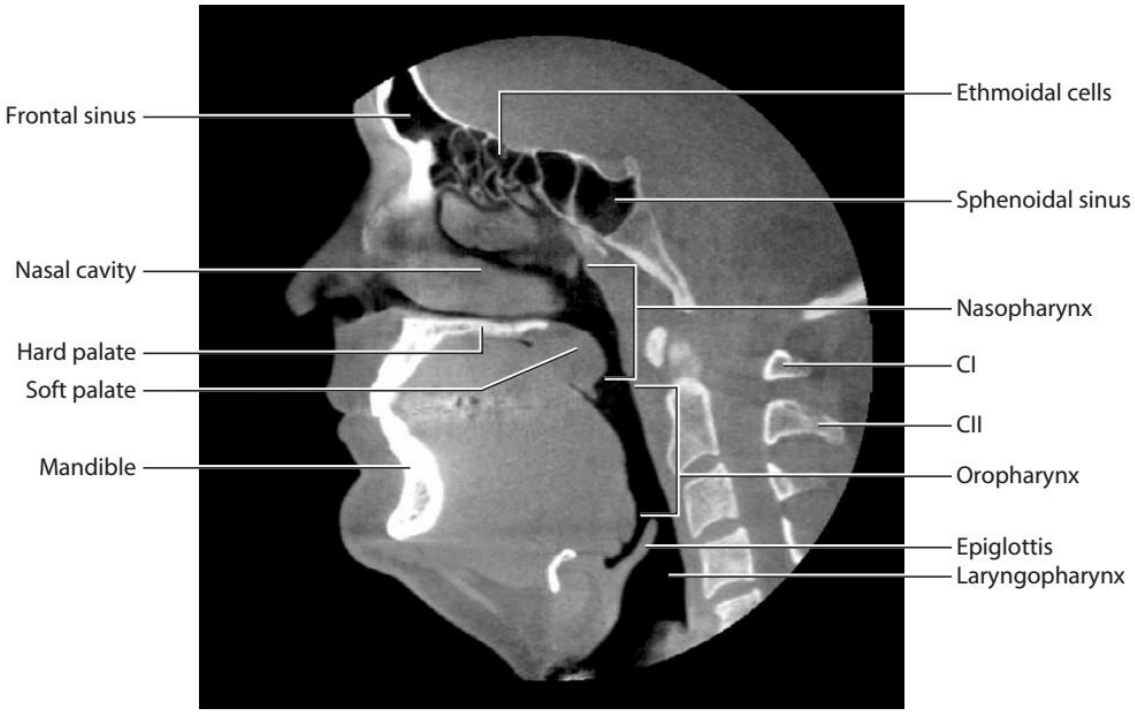

Figure B-1: Sagittal CT Scan of Pharynx with Anatomy Labeled.[2]

[1] R.L. Drake, A.W. Vogel and A.W.M. Mitchell, *Gray's Anatomy for Students*, Philadelphia: Churchill Livingstone Elsevier, 2015.
[2] R.L. Drake, A.W. Vogel, A.W.M. Mitchell, R.M. Tibbitts, and P.E. Richardson, *Gray's Atlas of Anatomy*, Philadelphia: Churchill Livingstone Elsevier, 2015.

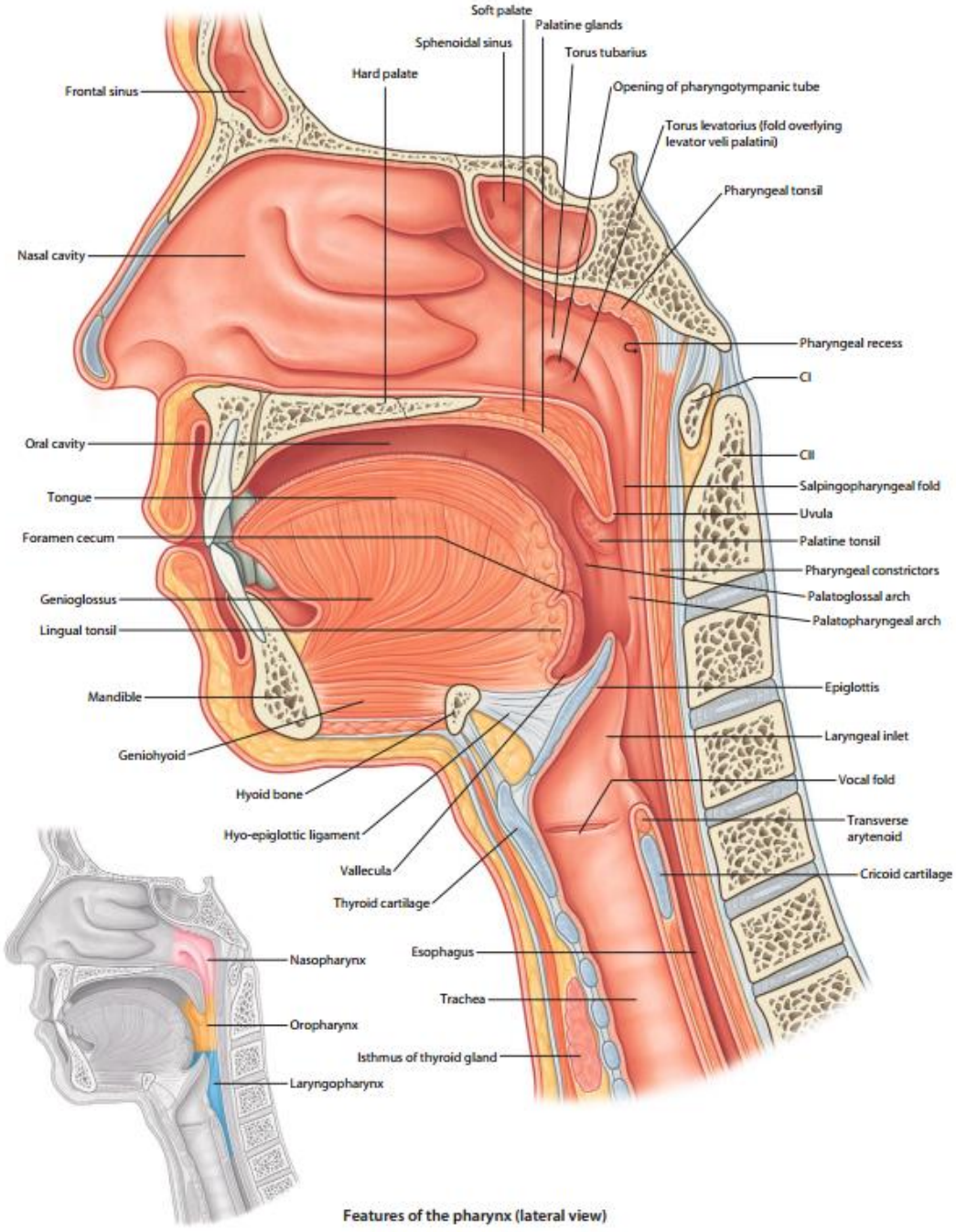

Figure B-2: Sagittal Diagram of Pharynx Anatomy.[2]

[2] R.L. Drake, A.W. Vogel, A.W.M. Mitchell, R.M. Tibbitts, and P.E. Richardson, *Gray's Atlas of Anatomy*, Philadelphia: Churchill Livingstone Elsevier, 2015.

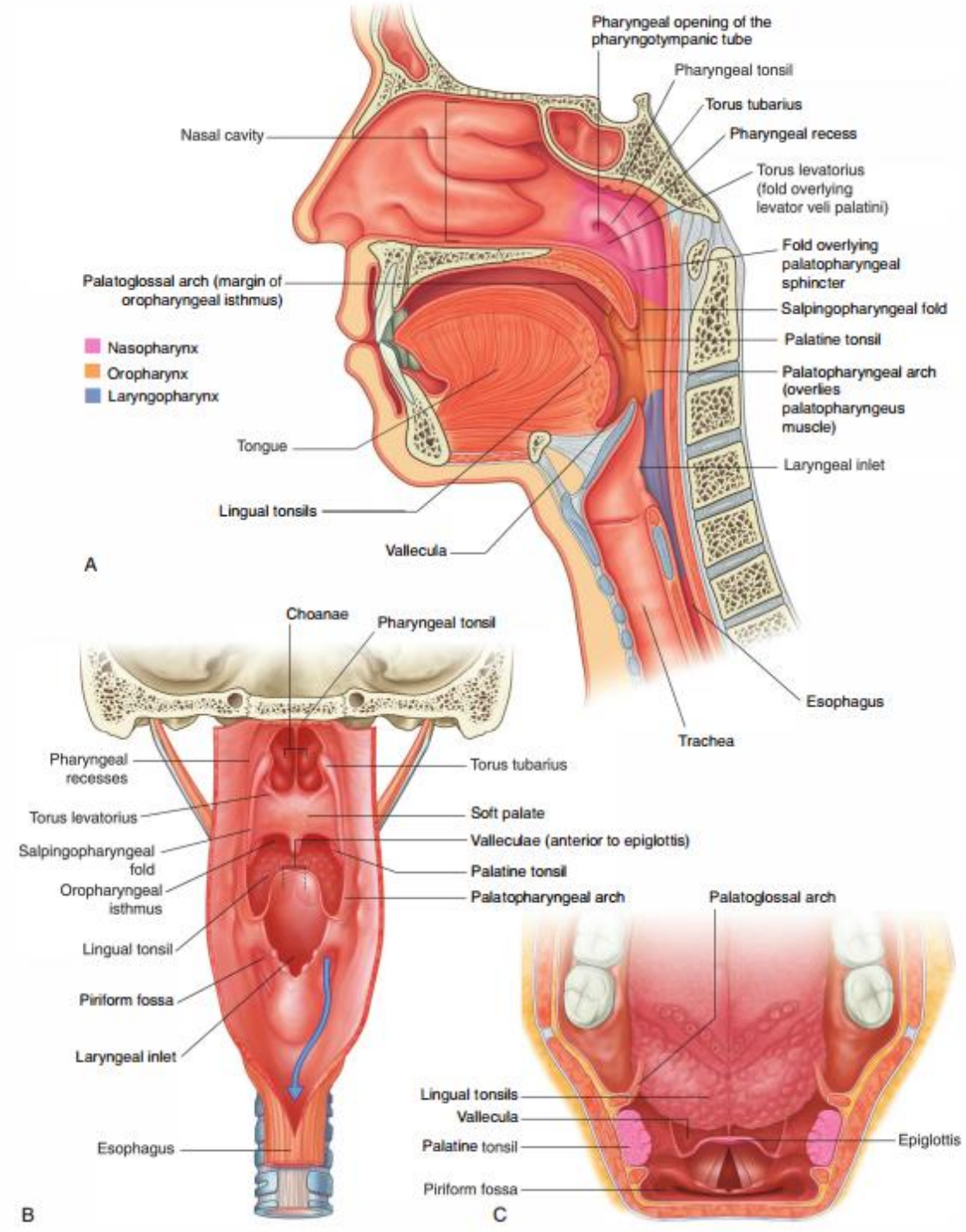

Figure B-3: Diagrams of Pharynx Anatomy in Multiple Views.[2]

[2] R.L. Drake, A.W. Vogel, A.W.M. Mitchell, R.M. Tibbitts, and P.E. Richardson, *Gray's Atlas of Anatomy*, Philadelphia: Churchill Livingstone Elsevier, 2015.

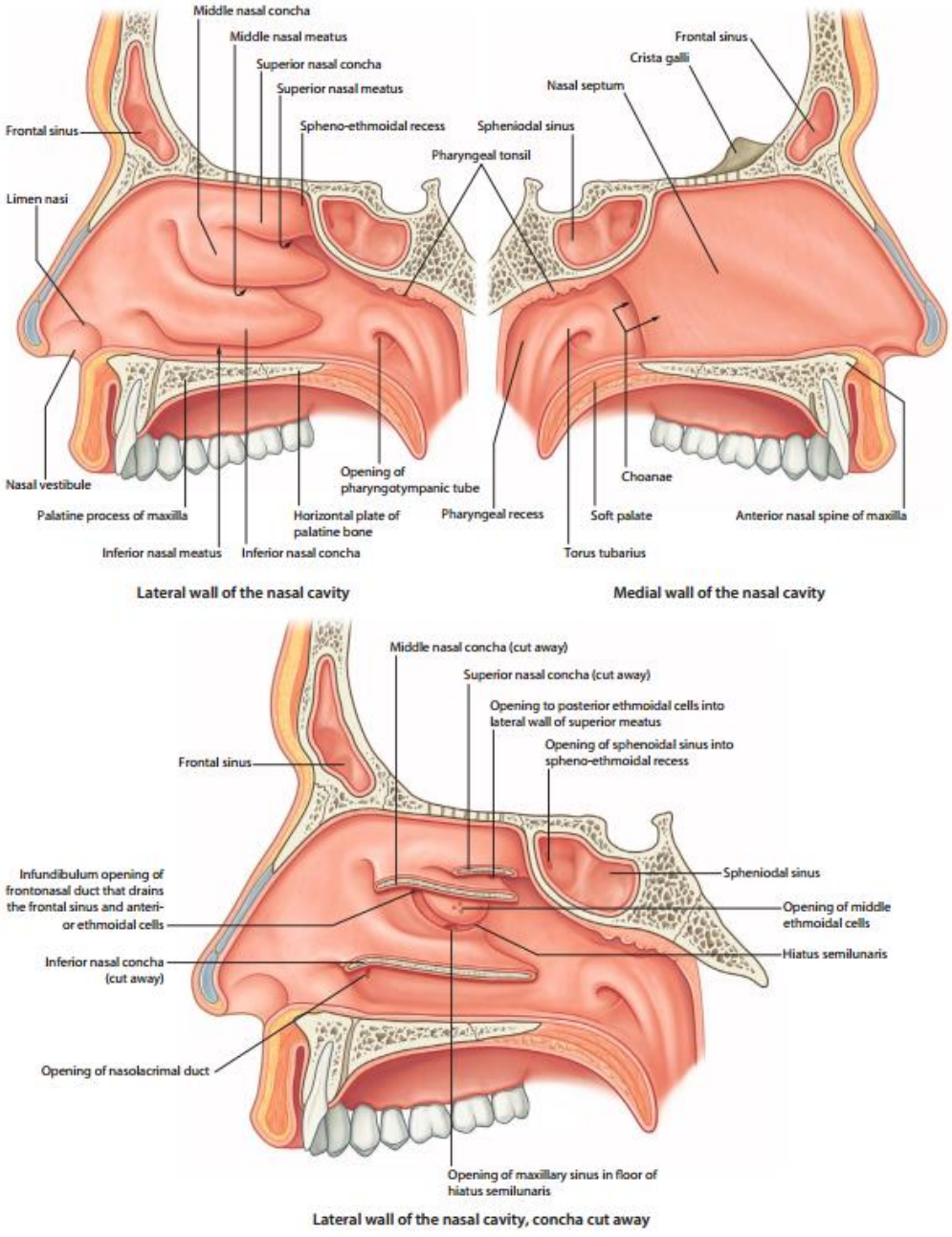

Figure B-4: Cut Away (Sagittal) Diagrams of Nasal Cavity Anatomy.[2]

[2] R.L. Drake, A.W. Vogel, A.W.M. Mitchell, R.M. Tibbitts, and P.E. Richardson, *Gray's Atlas of Anatomy*, Philadelphia: Churchill Livingstone Elsevier, 2015.

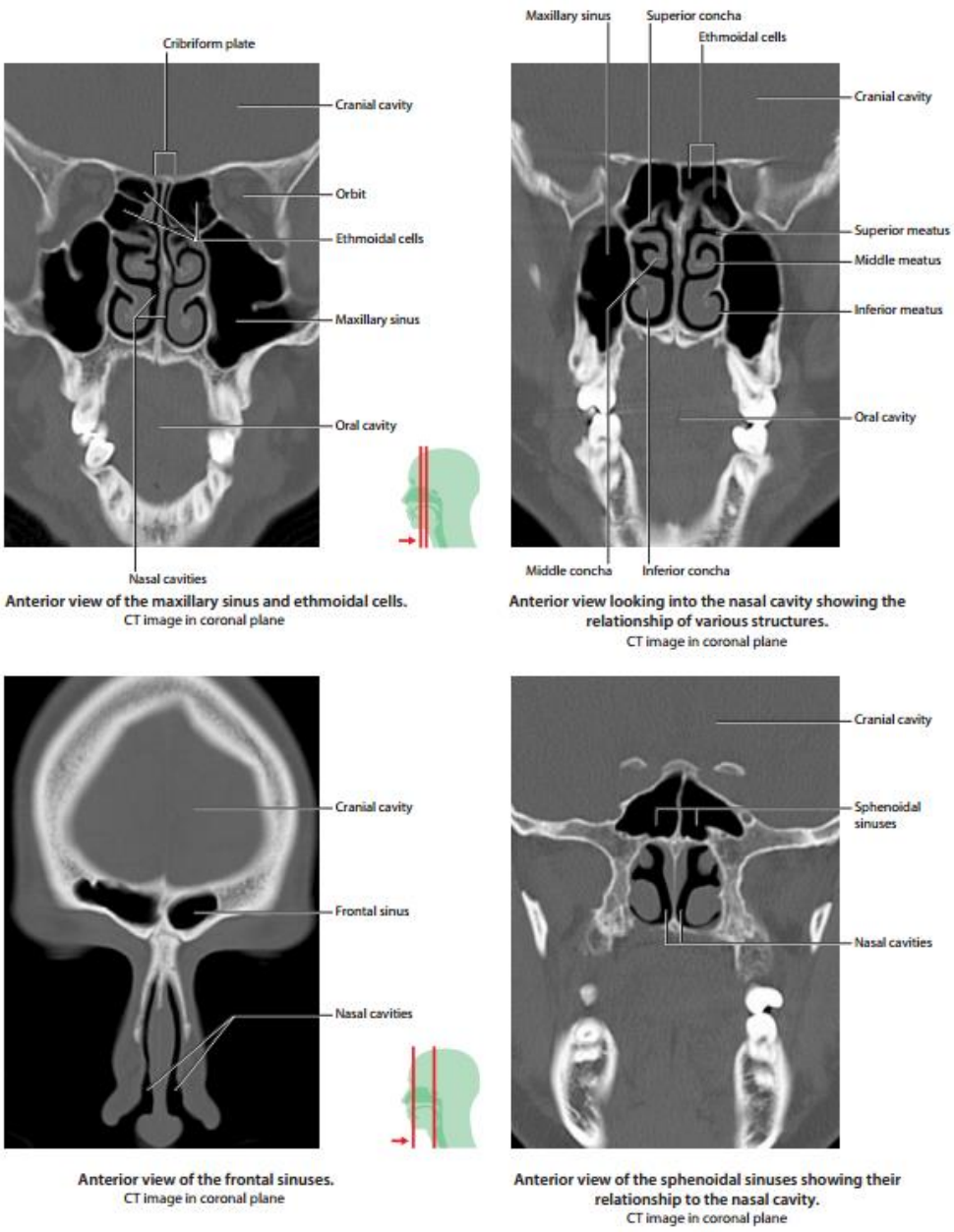

Figure B-5: Coronal CT Images of the Nasal Cavity with Anatomy Labeled.[2]

[2] R.L. Drake, A.W. Vogel, A.W.M. Mitchell, R.M. Tibbitts, and P.E. Richardson, *Gray's Atlas of Anatomy*, Philadelphia: Churchill Livingstone Elsevier, 2015.

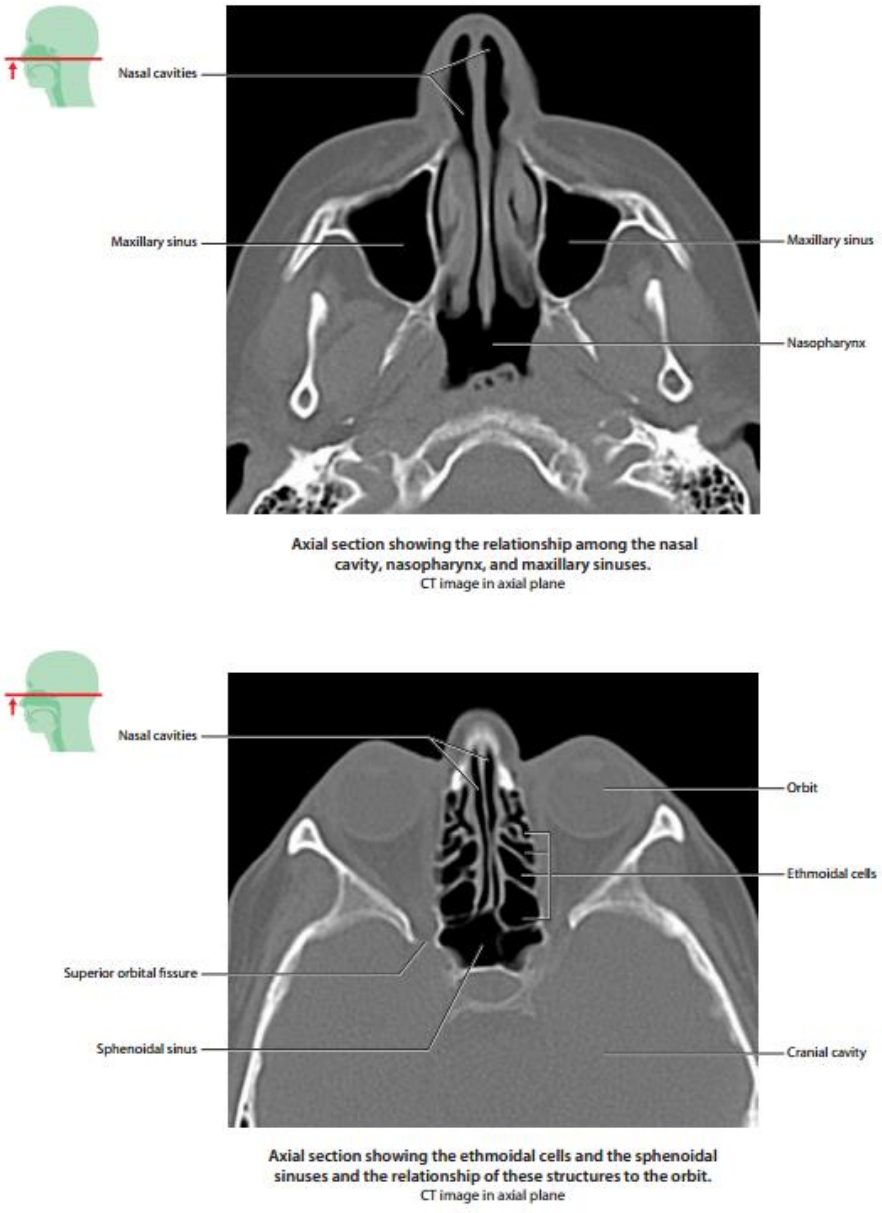

Figure B-6: Axial CT Images of the Nasal Cavity with Anatomy Labeled.[2]

[2] R.L. Drake, A.W. Vogel, A.W.M. Mitchell, R.M. Tibbitts, and P.E. Richardson, *Gray's Atlas of Anatomy*, Philadelphia: Churchill Livingstone Elsevier, 2015.

B.2 LOWER AIRWAY GEOMETRY

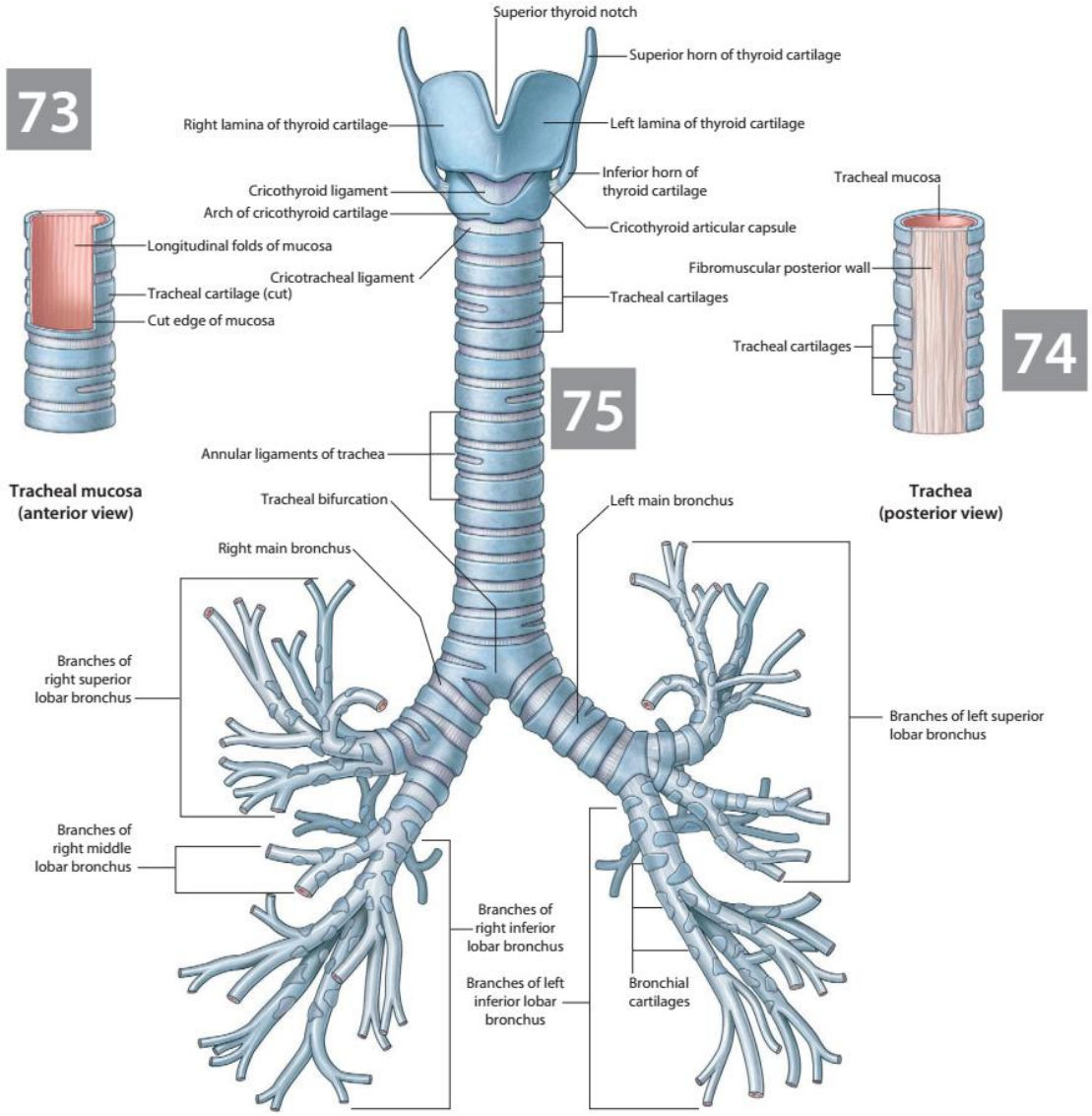

Figure B-7: Diagram of Trachea and Bronchial Tree.[2]

[2] R.L. Drake, A.W. Vogel, A.W.M. Mitchell, R.M. Tibbitts, and P.E. Richardson, *Gray's Atlas of Anatomy*, Philadelphia: Churchill Livingstone Elsevier, 2015.

APPENDIX C: ADDITIONAL CFD ANALYSIS

C.1 OVERVIEW

Additional analysis was performed for a specific region of Patient A's airway. Images 7 through 14 in the sixth axial series were used to develop a static model of the nasopharynx and oropharynx. This model was then altered based on the multi-volume analysis that was explained in Section 5.2.1.2. The segmentation performed using the seven images resulted in a discontinuous fluid model. This discontinuity is illustrated in Figure C-1 and Figure C-2. Figure C-1 shows the segmentation of the region as seen in the sagittal plane, whereas Figure C-2 shows the developed three-dimensional (3D) model from the segmentation. Additional modeling from the author was required to develop a continuous fluid domain. This resulted in an unnatural transition between the top and bottom islands, shown in Figure C-3.

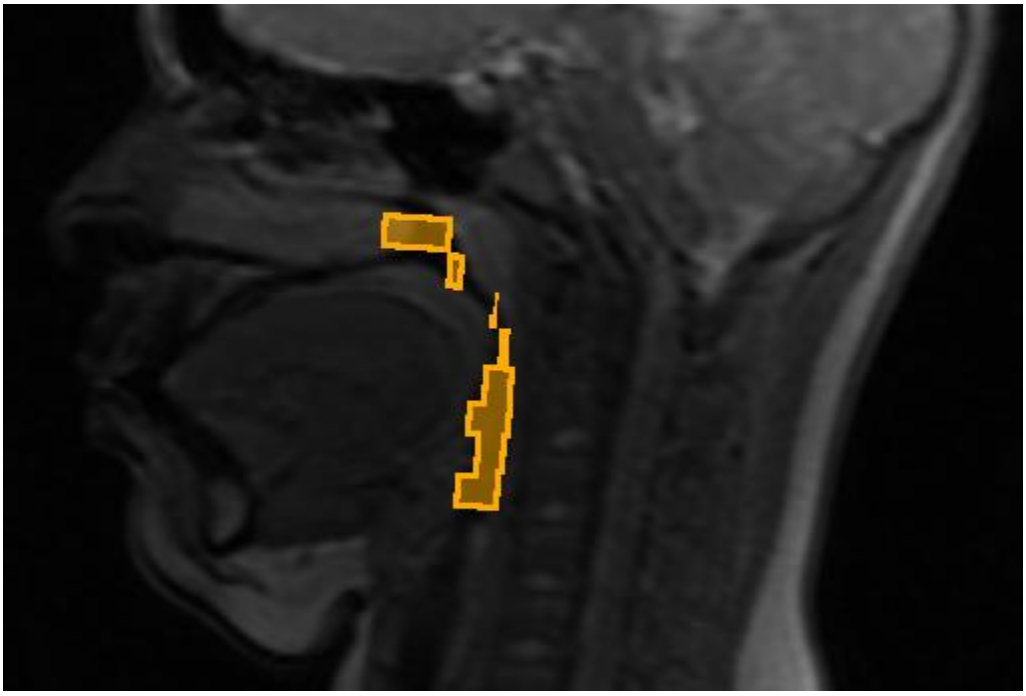

Figure C-1: Segmentation of Images 7 through 14 as Seen in the Sagittal Plane.

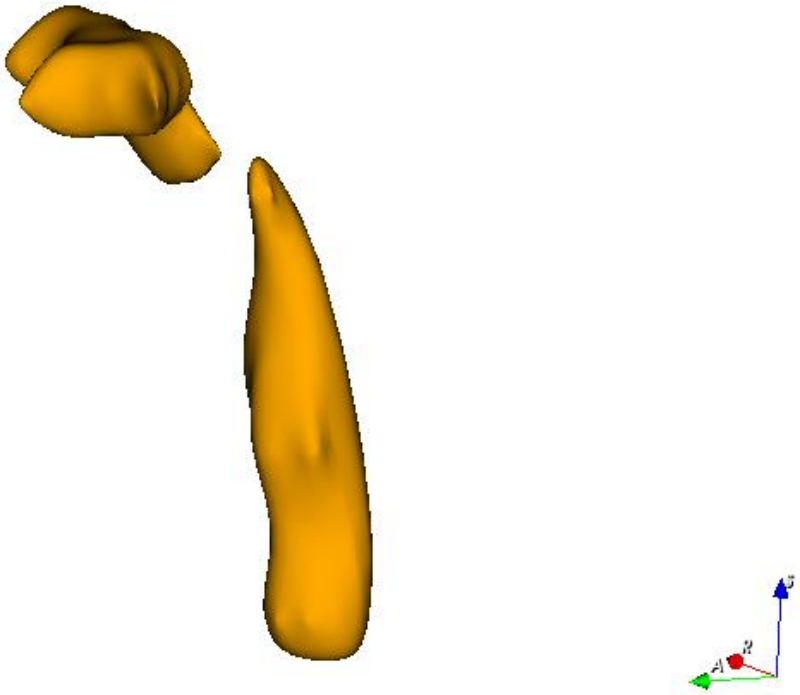

Figure C-2: Preliminary Model of Fluid Domain as Generated from Images 7 through 14.

Figure C-3: Refined Fluid Model to Remove Discontinuity.

It should be noted that the modifications used to develop a continuous model introduced human error into the geometry. Thus, simulation results may not accurately depict the airflow that the patient experiences. For this reason, two geometries were analyzed. The first geometry was the fluid domain depicted in Figure C-3 (i.e., geometry created from axial images 7 through 14) while the second geometry was only the bottom island shown in Figure C-2 (i.e., geometry created from axial images 9 through 14).

C.2 GEOMETRY

Figure C-4 features the two geometries that were developed for simulation. In both models, the inlet and outlet have been extended by a minimum of 5 hydraulic diameters. This was done to establish fully developed flow within the region of interest and to ensure the boundary conditions were satisfied without interfering flow behavior.

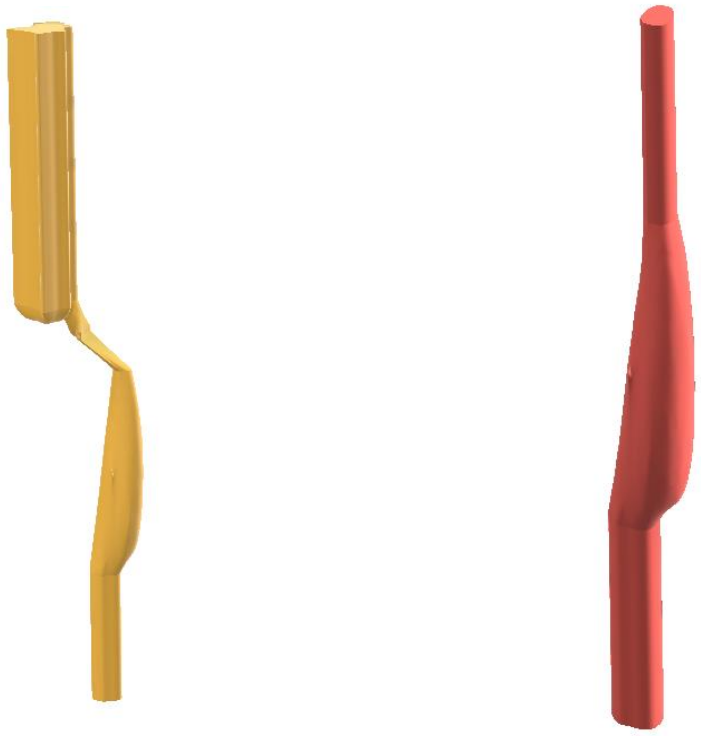

(a) Entire Domain (Images 7-14) **(b) Partial Domain (Images 9-14)**

Figure C-4: Geometry Used for Simulation.

C.3 Simulation

The parameters listed in Table 3 were used to set up the CFD model. From this table, the density and viscosity of the air were used to define the fluid properties whereas the mass flow rate and a zero-gauge pressure were used for boundary conditions. A steady-state k-ω turbulent model was used to analyze both inhalation and expiration. Simulation was then repeated after uniform dilation and erosion and fluid domain models were made. The scaling factors used are those listed in Table 14. The full domain and partial domain models have vastly different fluid flow behavior and thus stress the importance of boundary conditions and the captured airway geometry.

C.3.1 Full Domain (Images 7 through 14)

Figure C-5, C-6, and C-7 show the full domain models.

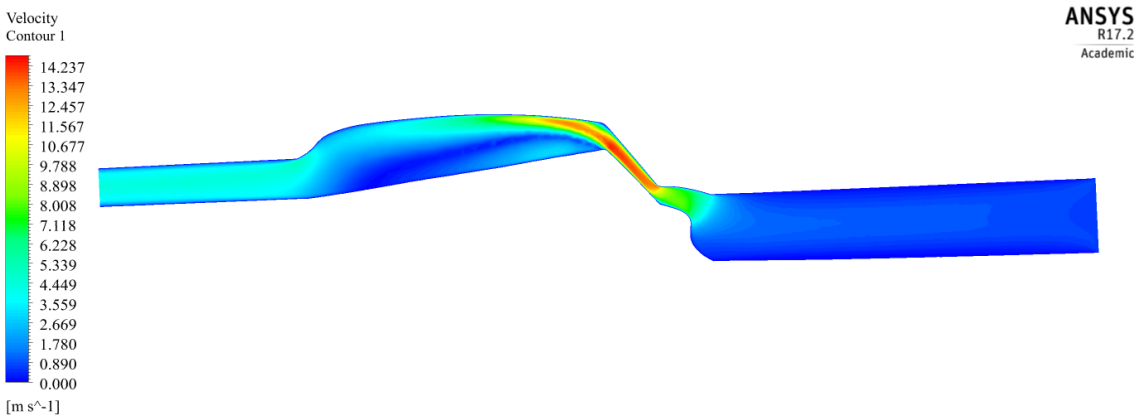

Figure C-5: Velocity Contour Plot for an Inhale (Base Model).

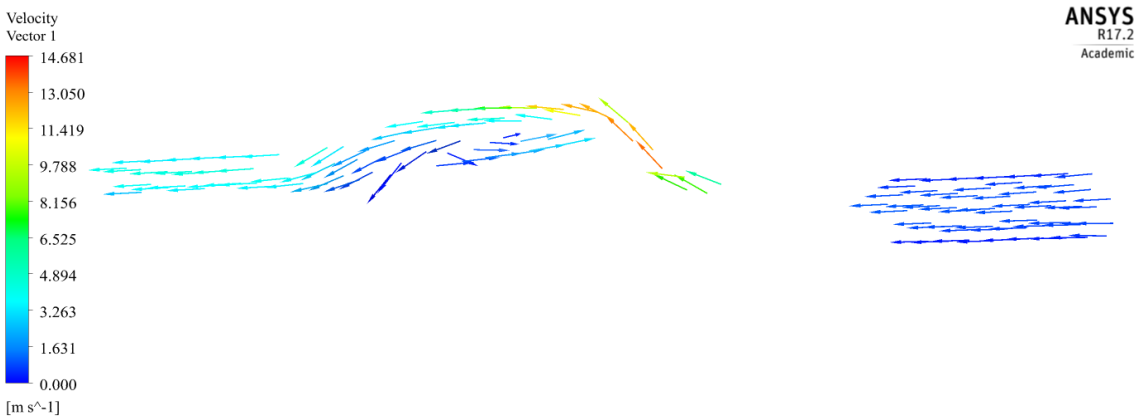

Figure C-6: Velocity Vector Plot for an Inhale (Base Model).

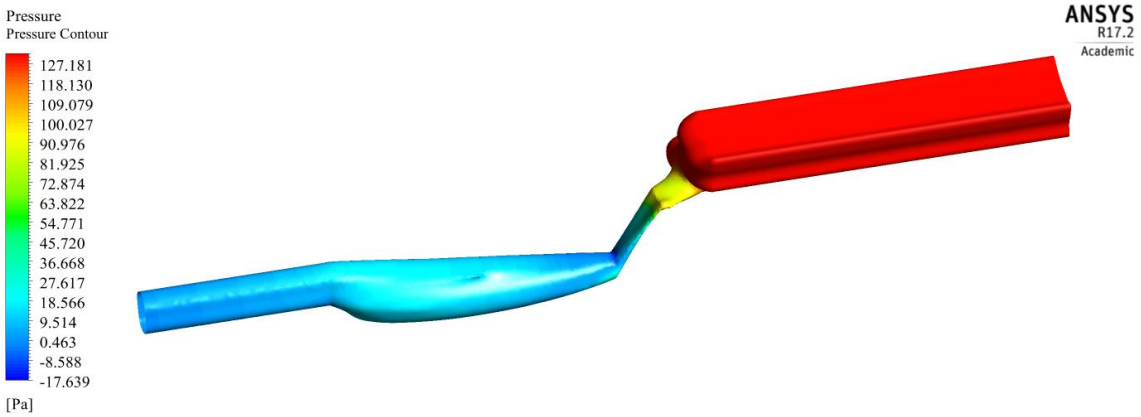

Figure C-7: Pressure Contour Plot for an Inhale (Base Model).

C.3.2 Partial Domain (Images 9 through 14).

Figures C-8 through C-25 show the partial domain model.

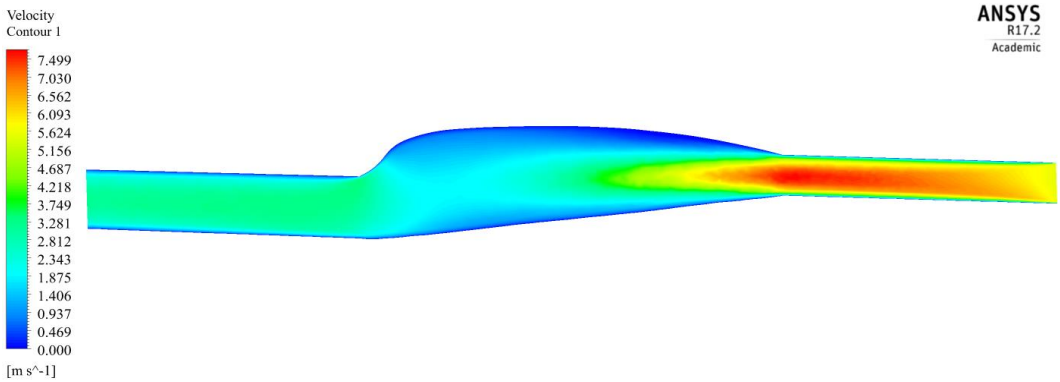

Figure C-8: Velocity Contour Plot for an Inhale (Dilated Model).

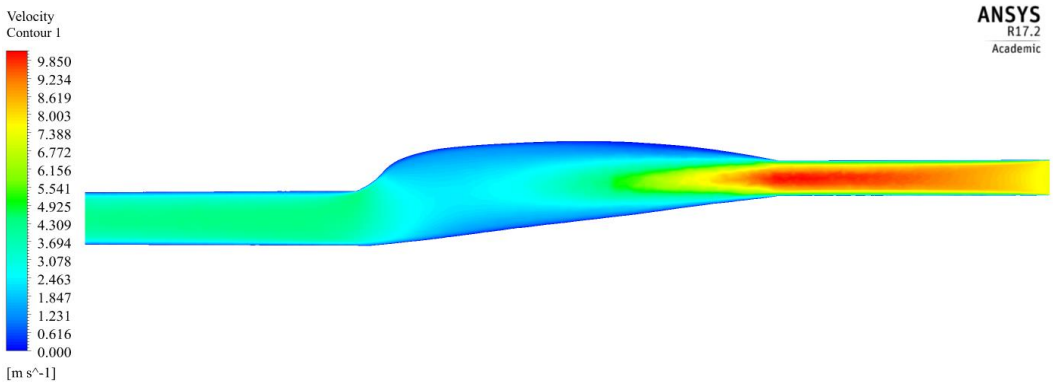

Figure C-9: Velocity Contour Plot for an Inhale (Base Model).

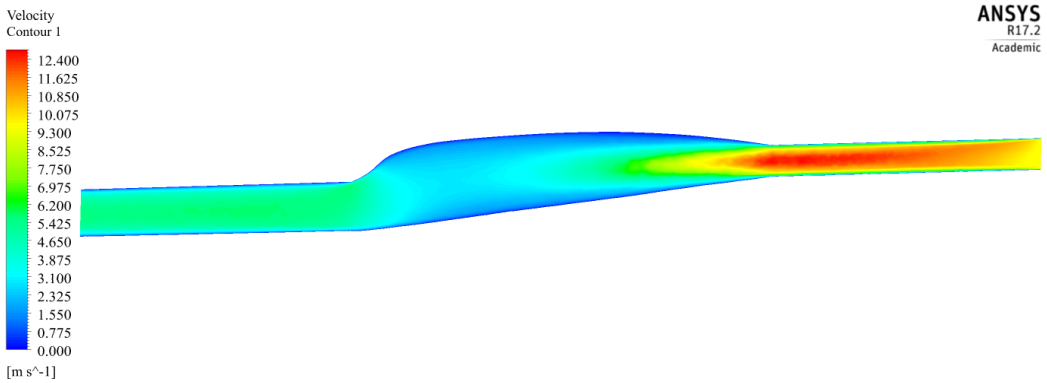

Figure C-10: Velocity Contour Plot for an Inhale (Eroded Model).

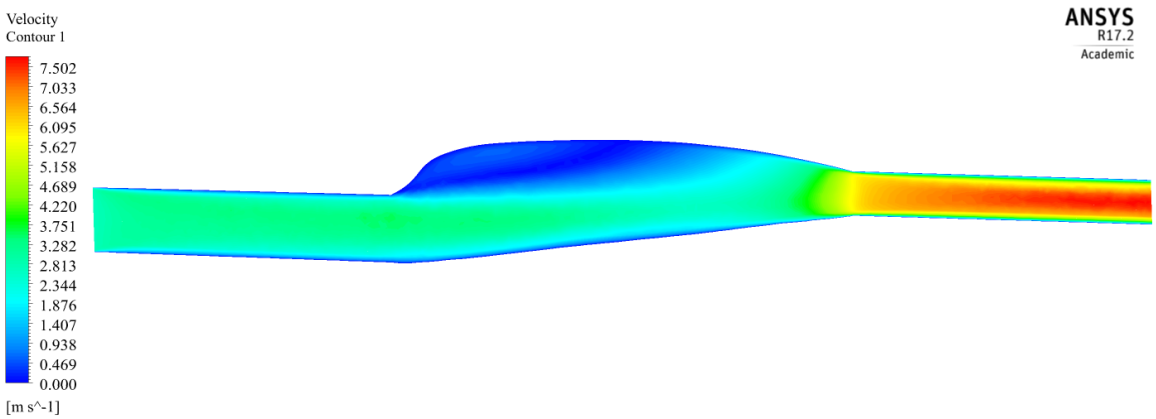

Figure C-11: Velocity Contour Plot for an Exhale (Dilated Model).

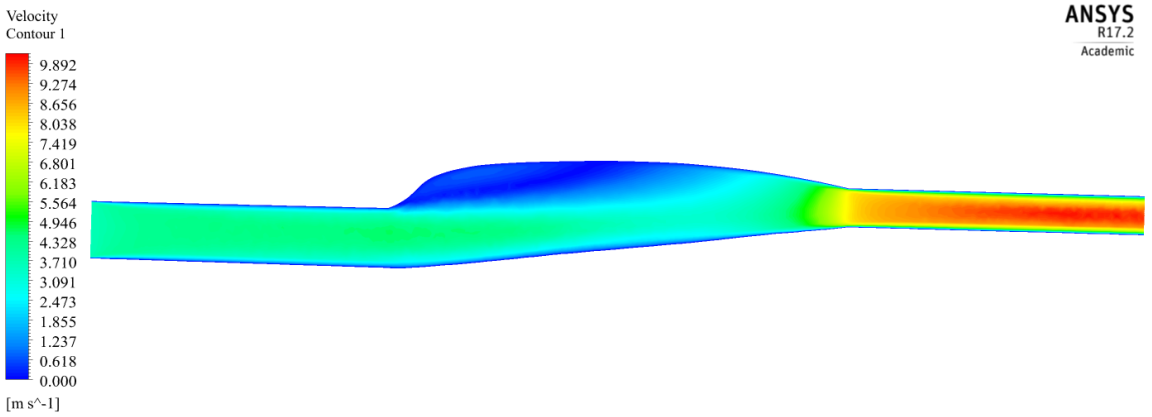

Figure C-12: Velocity Contour Plot for an Exhale (Base Model).

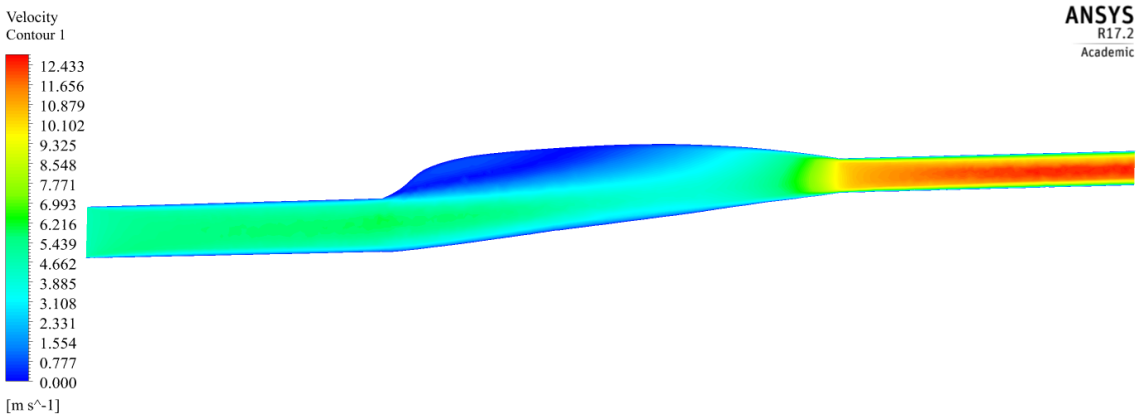

Figure C-13: Velocity Contour Plot for an Exhale (Eroded Model).

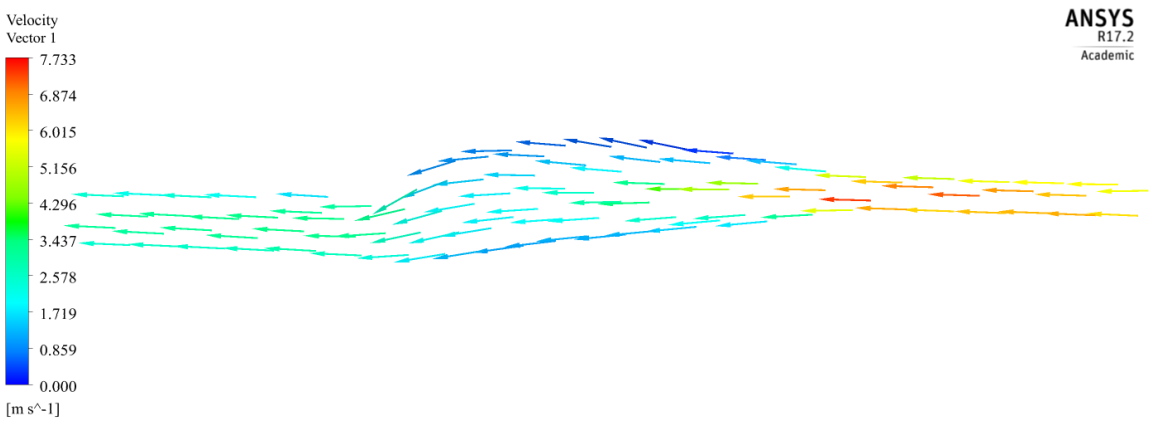

Figure C-14: Velocity Vector Plot at for an Inhale (Dilated Model).

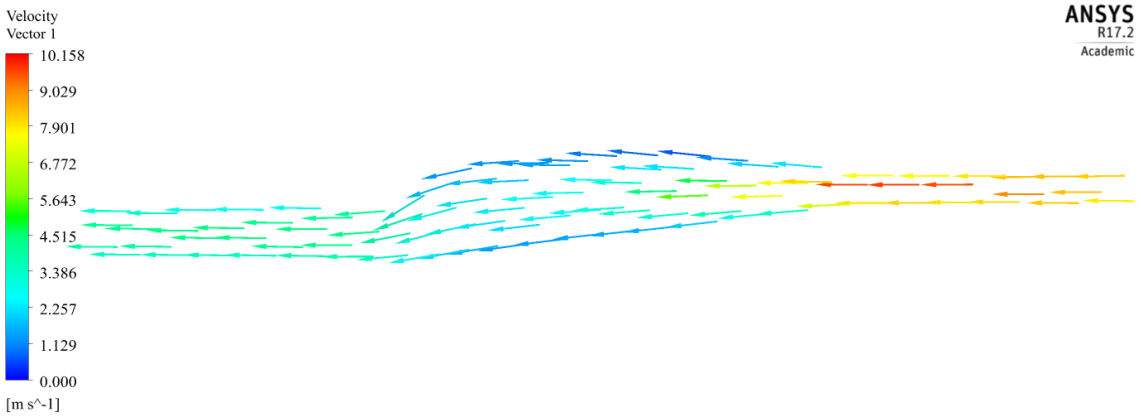

Figure C-15: Velocity Vector Plot at for an Inhale (Base Model).

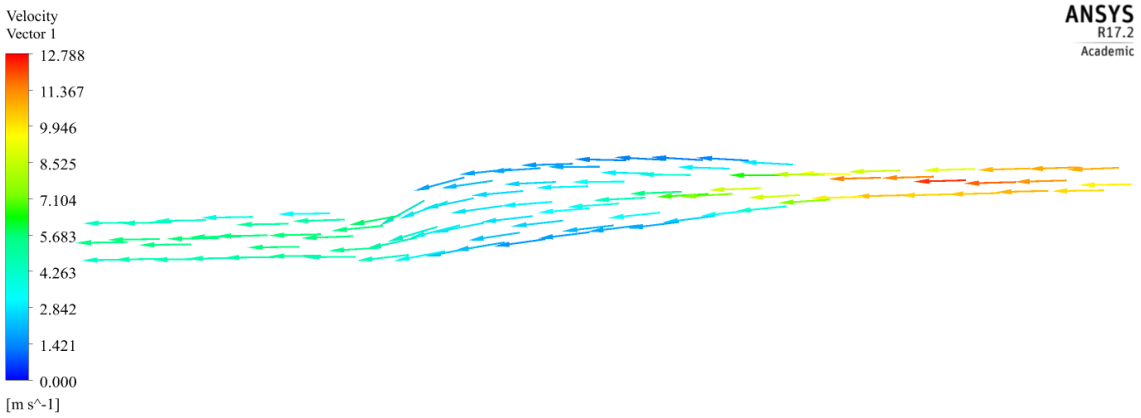

Figure C-16: Velocity Vector Plot at for an Inhale (Eroded Model).

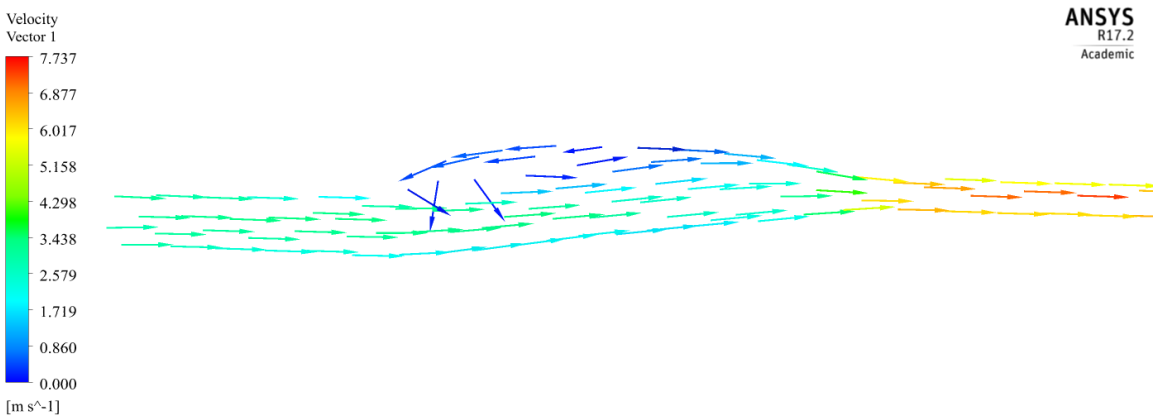

Figure C-17: Velocity Vector Plot at for an Exhale (Dilated Model).

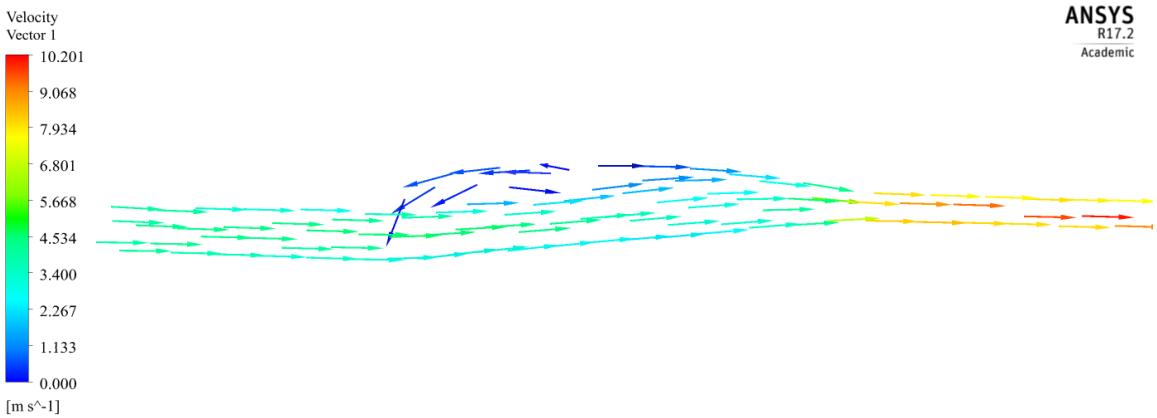

Figure C-18: Velocity Vector Plot at for an Exhale (Base Model).

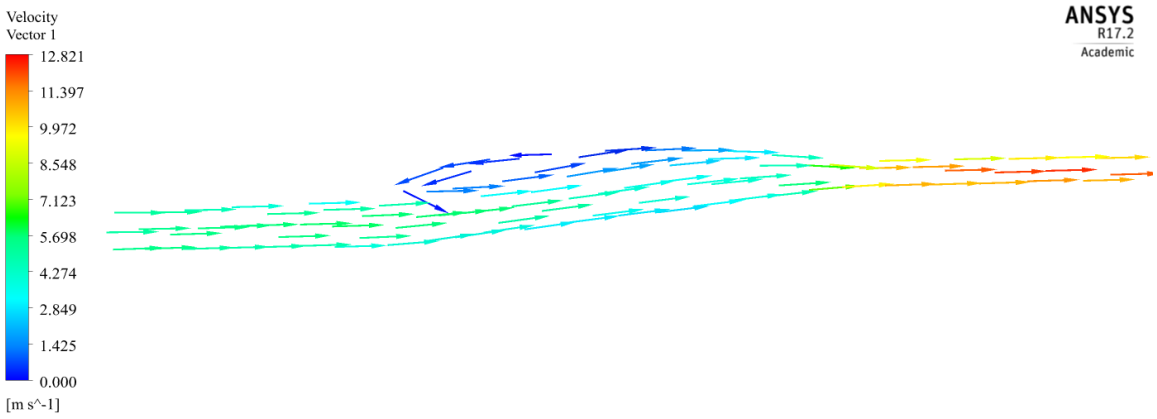

Figure C-19: Velocity Vector Plot at for an Exhale (Eroded Model).

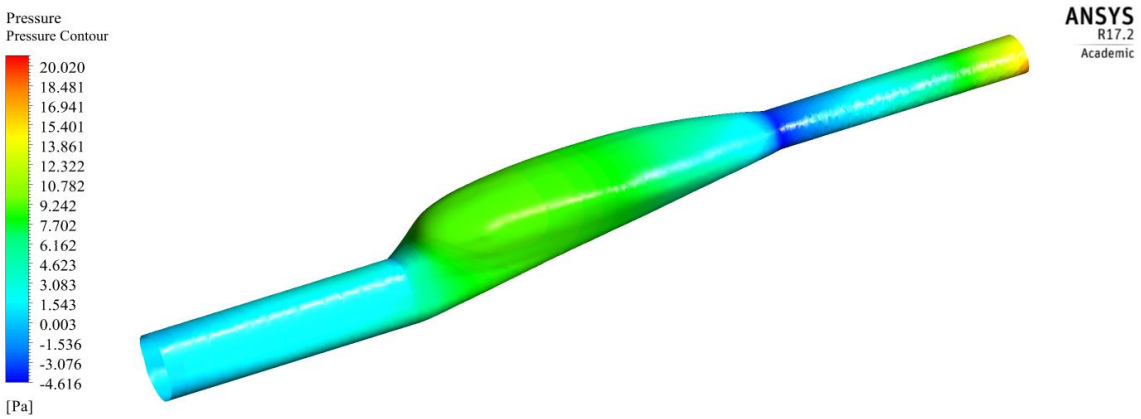

Figure C-20: Pressure Contour for an Inhale (Dilated Model).

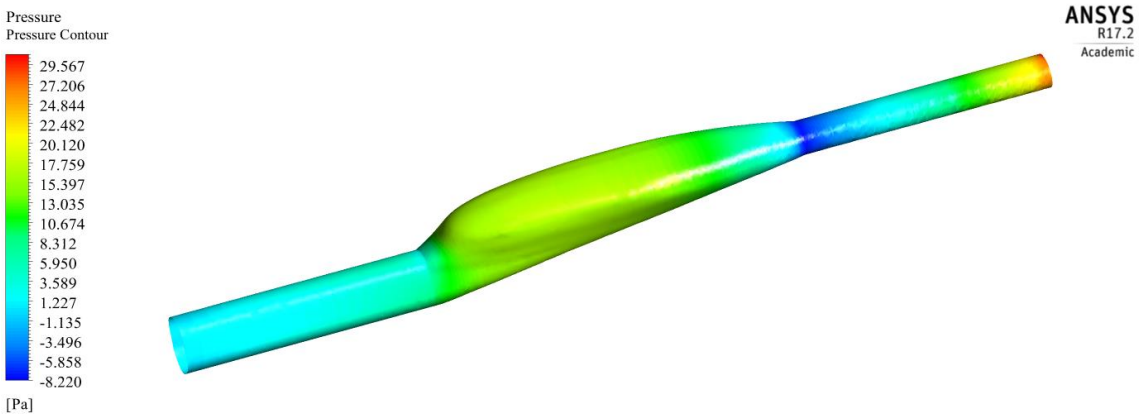

Figure C-21: Pressure Contour for an Inhale (Base Model).

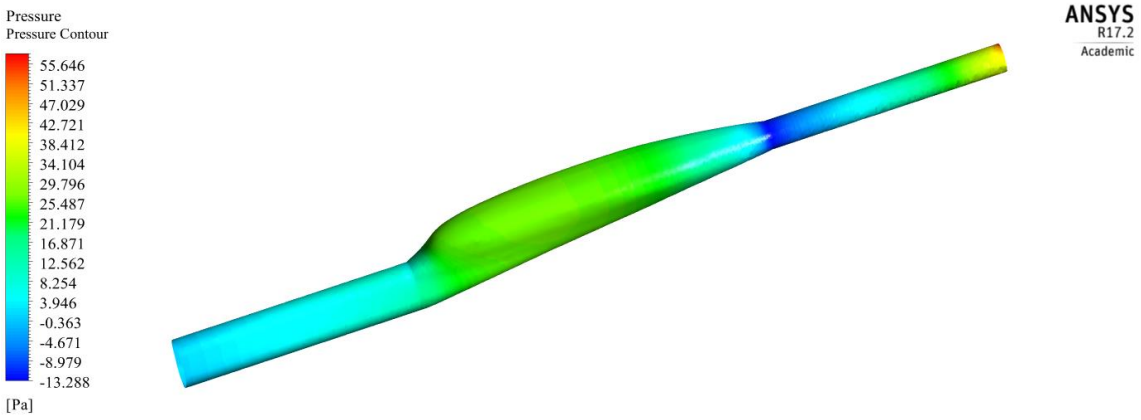

Figure C-22: Pressure Contour for an Inhale (Eroded Model).

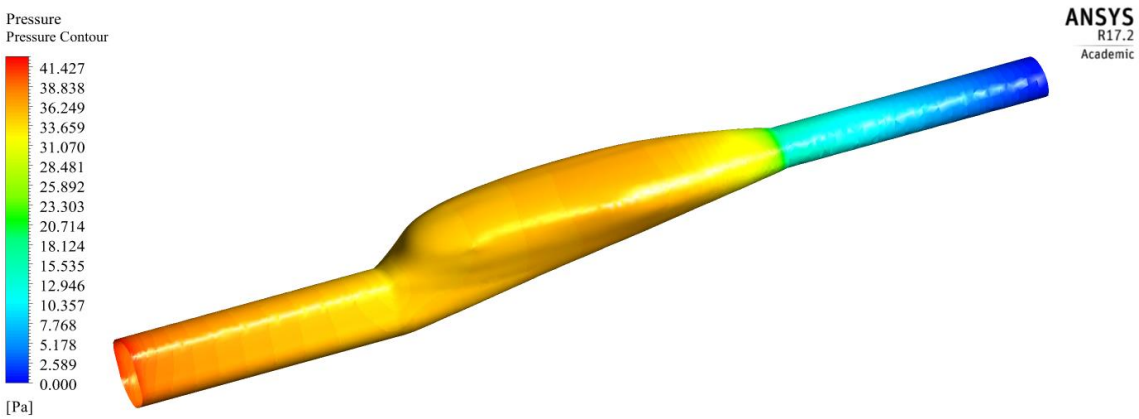

Figure C-23: Pressure Contour for an Exhale (Dilated Model).

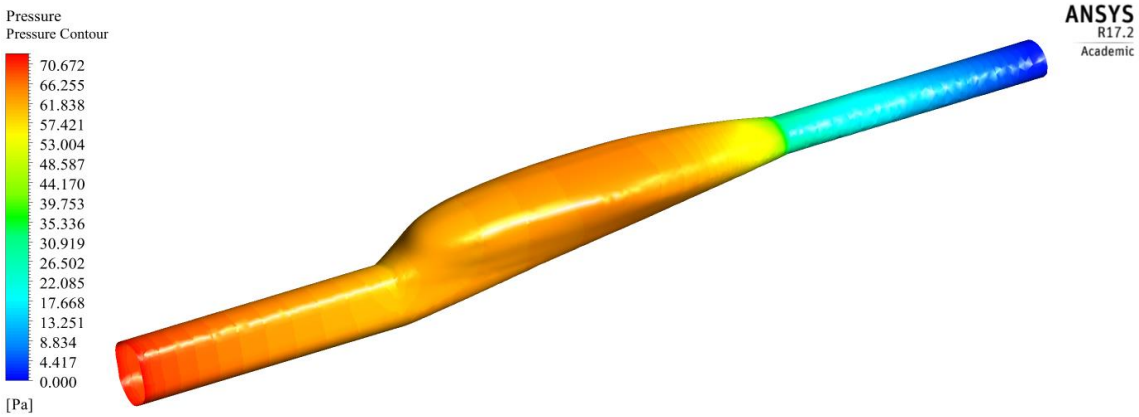

Figure C-24: Pressure Contour for an Exhale (Base Model).

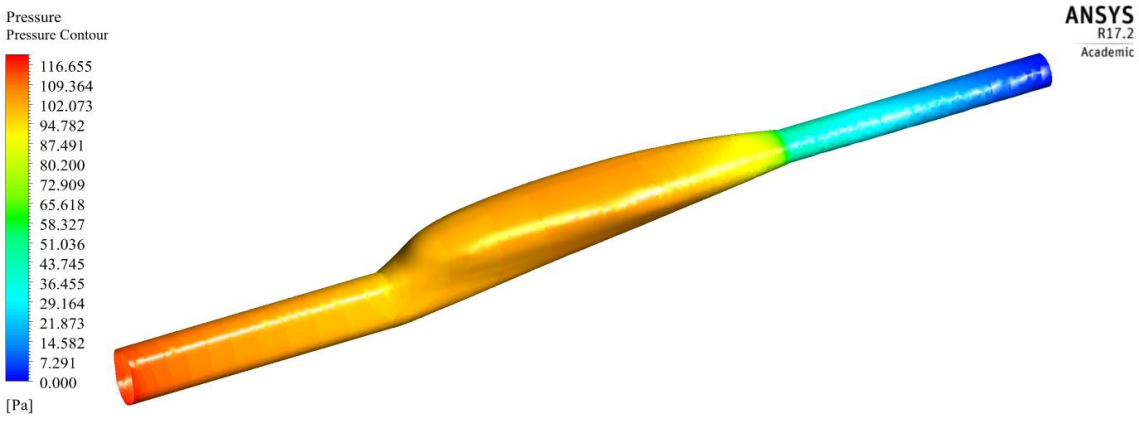

Figure C-25: Pressure Contour for an Exhale (Eroded Model)

Engineering

Capstone Report Approval Form

Master of Science in Engineering – MSE

Milwaukee School of Engineering

This capstone report, titled "Modeling and Analysis of Human Airway Dynamics Utilizing Data Obtained from a Cine MRI," submitted by the student Wesley A. Zloza, has been approved by the following committee:

Faculty Co-Advisor: _____ Date: _____

Dr. Subha Kumpaty, Ph.D.

Faculty Co-Advisor: _____ Date: _____

Dr. Ravi Elluru, M.D., Ph.D.

Faculty Co-Advisor: _____ Date: _____

Dr. Maninder Kalra, M.D., Ph.D.

Faculty Member: _____ Date: _____

Professor Gary Shimek, M.L.I.S.